IN SITU SENSING AND MODELING OF MOLECULAR EVENTS AT THE CELLULAR LEVEL

By

Ruiguo Yang

A DISSERTATION

Submitted to
Michigan State University
in partial fulfillment of the requirements
for the degree of

Electrical Engineering - Doctor of Philosophy

2014

ABSTRACT

IN SITU SENSING AND MODELING OF MOLECULAR EVENTS AT THE CELLULAR LEVEL

By

Ruiguo Yang

We developed the Atomic Force Microscopy (AFM) based nanorobot in combination with other nanomechanical sensors for the investigation of cell signaling pathways. The AFM nanorobotics hinge on the superior spatial resolution of AFM in imaging and extends it into the measurement of biological processes and manipulation of biological matters. A multiple input single output control system was designed and implemented to solve the issues of nanomanipulation of biological materials, feedback, response frequency and nonlinearity. The AFM nanorobotic system therefore provide the human-directed position, velocity and force control with high frequency feedback, and more importantly it can feed the operator with the real-time imaging of manipulation result from the fast-imaging based local scanning. The use of the system has taken the study of cellular process at the molecular scale into a new level.

The cellular response to the physiological conditions can be significantly manifested in cellular mechanics. Dynamic mechanical property has been regarded as biomarkers, sometimes even regulators of the signaling and physiological processes, thus the name mechanobiology. We sought to characterize the relationship between the structural dynamics and the molecular dynamics and the role of them in the regulation of cell behavior. We used the AFM nanorobotics to investigate the mechanical properties in realtime of cells that are stimulated by different chemical species. These reagents could result in similar ion channel responses but distinctive mechanical behaviors. We applied these measurement results to establish a model that describes the cellular stimulation and the mechanical property change, a “two-hit” model that comprises the loss of cell adhesion and

the initiation of cell apoptosis. The first hit was verified by functional experiments: depletion of Calcium and nanosurgery to disrupt the cellular adhesion. The second hit was tested by a labeling of apoptotic markers that were revealed by flow cytometry. The model would then be able to decipher qualitatively the molecular dynamics infolded in the regulation of cell behavior.

To decipher the signaling pathway quantitatively, we employed a nanomechanical sensor at the bottom of the cell, quartz crystal microbalance with energy dissipation monitoring (QCM-D) to monitor the change at the basal area of the cell. This would provide the real time focal adhesion information and would be used in accordance with the AFM measurement data on the top of the cell to build a more complete mechanical profile during the antibody induced signaling process. We developed a model from a systematic control perspective that considers the signaling cascade at certain stimulation as the controller and the mechanical and structural interaction of the cell as the plant. We firstly derived the plant model based on QCM-D and AFM measurement processes. A signaling pathway model was built on a grey box approach where part of the pathway map was delineated in detail while others were condensed into a single reaction. The model parameters were obtained by extracting the mechanical response from the experiment. The model refinements were conducted by testing a series of inhibition mechanisms and comparing the simulation data with the experimental data. The model was then used to predict the existence of certain reactions that are qualitatively reported in the literature.

ACKNOWLEDGMENTS

I would like to express my most sincere appreciation to my advisor, Dr. Ning Xi, for his expert guidance, generous encouragement and support for my research.

In addition, I would like to thank all my PhD committee members: Dr. Lixin Dong, Dr. Robert J. McGough, Dr. Donna H. Wang and Dr. Animesh A. Sinha. They offered me timely help and unfailing support that improve the technical soundness and the presentation of this dissertation.

Furthermore, I would like to express my gratitude to all my colleagues, especially to Dr. King Wai Chiu Lai, Dr. Carmen Kar Man Fung, Dr. Hongzhi Chen, Bo Song, Zhiyong Sun, Liangliang Chen, Jianguo Zhao, and Yunyi Jia, for their support in the experiments and discussion.

Last but not the least, I want to thank my parents and my wife, Jie Guo. This dissertation would not have been possible without their years of encouragement and continuous support. With love and gratitude, I dedicate this dissertation to them.

TABLE OF CONTENTS

LIST OF TABLES . . . . . **ix**

LIST OF FIGURES . . . . . **x**

Chapter 1 Introduction **1**
1.1 Overview 1
1.2 Sensing techniques 3
1.2.1 Structural sensing and force sensing 3
1.2.2 Structural sensing at the cell level 5
1.2.2.1 High resolution imaging by fluorescence imaging 5
1.2.2.2 Scanning Electron Microscopy (SEM) imaging 6
1.2.2.3 Stochastic optical reconstruction microscopy (STORM) 8
1.2.2.4 AFM with Raman spectroscopy 8
1.2.3 Nanomechanical sensors for biological detection 9
1.2.3.1 Cantilever arrays and nano-resonators 9
1.2.3.2 Traction force microscopy (TFM) 10
1.2.3.3 QCM-D detecting energy dissipation in cell adhesion 10
1.2.4 Force sensing at the cell level 11
1.2.5 Force sensing at the molecular level 11
1.2.5.1 Tip functionalization based on self-assembly 11
1.2.5.2 Single molecule force microscopy (SMFM) 12
1.3 Cell signaling pathway 14
1.3.1 Models of molecular kinetics 15
1.3.2 Michaelis-Menten reaction 15
1.3.3 Pathway regulation of cell adhesion 16
1.4 Objectives and challenges for AFM based nanorobotics integrated platform 20
1.5 Organization of the Study 22

Chapter 2 Nanobiomechanics in the identification of pathophysiological conditions 23
2.1 Introduction 23
2.2 Cell Mechanics 24
2.2.1 Membrane, Channels and Cytoskeleton 24
2.2.2 Mechanical model of cells 26
2.2.2.1 Continuum models 27
2.2.2.2 Structural models 32
2.2.3 Importance of cell adhesion in the establishment of cell mechanical states . 33
2.2.4 Different model could apply at different scenarios 34
2.3 Manipulation and measurements at the molecular level 34
2.3.1 DNA manipulation 35

2.3.2 Single cell manipulation . . . 35
2.3.3 Filament manipulation and characterization . . . 36
2.3.4 Nanodissection and nanosurgery . . . 37
2.4 Cellular nanosurgery mimics the effect of antibody treatment in cell-cell adhesion . 38

Chapter 3 *In situ* sensing of ion channel activities after glucose stimulation . . . 39
3.1 Introduction . . . 39
3.2 Materials and methods . . . 40
3.2.1 TRPV1 immunofluorescence . . . 42
3.2.2 Loading of Fur-2 AM to RINm5f cells . . . 42
3.2.3 Glucose and capsaicin stimulation and dosage-dependent study . . . 43
3.2.4 Simultaneous fluorescence imaging of $[Ca^{2+}]_i$ and AFM measurements on RINm5f cells . . . 44
3.2.5 Actin filament staining and imaging . . . 44
3.3 Results . . . 45
3.3.1 Immunofluorescence of TRPV1 on RINm5F cells . . . 45
3.3.2 AFM stiffness observation of dosage responses to glucose and capsaicin stimulation . . . 45
3.3.3 $[Ca^{2+}]_i$ and stiffness observation of glucose stimulation . . . 47
3.3.4 $[Ca^{2+}]_i$ and stiffness observation of capsaicin stimulation . . . 49
3.4 Discussion . . . 51
3.5 Chapter summary . . . 55

Chapter 4 *In situ* biomarker detection during signaling events . . . 56
4.1 Introduction . . . 56
4.2 Visualization of keratinocyte junctions under physiologic and disease conditions by AFM methods . . . 59
4.3 Mechanical characterization . . . 63
4.3.1 AFM based quantification of cell surface stiffness reveals autoantibody-associated nanostructural changes . . . 63
4.3.2 Desmosome disruption by other means . . . 64
4.4 Two-hit hypothesis . . . 67
4.5 An integrated model for antibody-mediated damage in the skin . . . 72
4.6 Chapter summary . . . 73

Chapter 5 Modeling and experimental verifications of cell tensegrity . . . 75
5.1 Introduction . . . 75
5.2 Desmosome disruption leads to decrease in cell stiffness . . . 77
5.2.1 Desmosome disassembly results in stiffness decrease . . . 78
5.2.2 AFM based nanosurgery resulting in the decrease of stiffness . . . 80
5.3 Quantitative modeling based on six struts tensegrity structure . . . 85
5.3.1 Without intermediate filaments . . . 88
5.3.2 With intermediate filaments . . . 89
5.4 Chapter summary . . . 92

Chapter 6 Dynamic characterization of cell signaling pathways mechanics 95
6.1 Introduction 95
6.1.1 AFM energy dissipation and hysteresivity measurements 97
6.1.2 QCM-D energy dissipation measurement 99
6.2 Model development 101
6.2.1 AFM viscoelastic characterization 101
6.2.2 QCM-D based cell membrane peeling model 102
6.3 Results and Discussion 105
6.4 Chapter summary 111

Chapter 7 Plant model derivation 113
7.1 Introduction 113
7.2 Model development 115
7.2.1 The dynamics model for the sensor disk 116
7.2.2 The mechanical model of cell adhesion 117
7.2.3 Gaussian compensation of oscillation amplitude 120
7.2.4 Numerical simulation 122
7.3 Result and discussion 122
7.3.1 The dynamics of the sensor disk and the kinetics of the bond 122
7.3.2 Contributions from different energy dissipation source 125
7.3.3 Relationship of bond number and energy dissipation 126
7.3.4 Experimental observations 128
7.4 Chapter summary 129

Chapter 8 Modeling of signaling pathway dynamics 131
8.1 Introduction 131
8.2 Model development 135
8.2.1 Plant model 136
8.2.2 The controller model 138
8.3 Result 142
8.4 Chapter summary 145

Chapter 9 Conclusion and future work 147
9.1 Conclusion 147
9.1.1 Development of AFM nanorobotics for biomedical applications 147
9.1.2 Dynamical monitoring of cellular structural and mechanical changes under patho/physiological conditions 148
9.1.3 Nanomechanical characterization and nanorobotic surgery delineate cell signaling pathway 149
9.1.4 Cell adhesion model with nanomechanical oscillator 150
9.1.5 A systematic control model for cell signaling pathway 151
9.2 Future work 151
9.2.1 Signal transduction and propagation study 151
9.2.2 Functional model of the pathway based on mechanical profile 152

BIBLIOGRAPHY **154**

LIST OF TABLES

Table 5.1 Parameter list for the numerical evaluation 92

Table 7.1 The parameters in the model with their physical meanings used for the simulation 123

Table 8.1 State variables and ODEs 140

Table 8.2 Rate constants 146

LIST OF FIGURES

Figure 1.1 Schematic drawing of AFM working principle 4

Figure 1.2 High resolution images showing the cytoskeleton structure under the applied peak force of 5 nN, scan size: 30 μm. 6

Figure 1.3 The combination configuration of fluorescence microscopy with AFM. Simultaneous imaging of B lymphoma cells labeled with anti-CD20 (FITC labeled) surface receptor and the AFM is shown. 7

Figure 1.4 Tip functionalization with the intermediate linker molecules. 12

Figure 1.5 SAM formation onto goad coated AFM tip. 13

Figure 1.6 The binding force measuring process. 13

Figure 1.7 A: The diagram of cell adhesion regulation pathways. B: Image of focal adhesion by florescence. C: AFM image of the living cells with focal adhesion complex. 18

Figure 2.1 A: The conversion of force-displacement curve to force-indentation curve; B: The fitting of the force indentation curve by Hertz model to generate the Youngs modulus. 29

Figure 2.2 A: The cell structure is based on cytoskeleton tensegrity. B: Tensegrity structures. 33

Figure 3.1 A: The stimulus-secretion coupling model of β-cells. Increased plasma glucose levels will increase the intracellular ATP/ADP ratio after glucose being uptaked by cells, which leads to the closure of ATP-dependent potassium channels, membrane depolarization, and the increase in intracellular Ca^{2+} concentrations through the activation of voltage dependent calcium channels (VDCC) and ultimately insulin secretion. Capsaicin binds to the intracellular domain of the TRPV1 receptor and causes the influx of Ca^{2+}, which triggers the release of Ca^{2+} into the cytoplasm from the endoplasmic reticulum (ER) and increases $[Ca^{2+}]_i$ concentrations. B: The AFM based nanorobotic manipulator uses a joystick as position input to facilitate the movement of the AFM tip in the planar area during the force measurement process. 41

Figure 3.2 Immunofluorescence imaging of TRPV1 receptors in RINm5f insulinoma cells. A: Cell plasma membrane localization of TRPV1 receptors in RINm5f cells, positive staining indicated by arrows. B: Control RINm5f cells in which primary antibody was replaced with 1% BSA in PBS show negative staining. Scale bar: 20 μ m. C: The stiffness changes before and after administration of glucose at three concentrations, 16 mM, 20 mM, and 40 mM, plus the control. * $p<0.05$ vs. before stimulation; $p<0.05$ vs. control; $p<0.05$ vs. glucose 16 mM; $p<0.05$ vs. glucose 16 mM and 20 mM (n=20). D: The stiffness changes before and after administration of Cap (capsaicin) at four concentrations (1.67 nM, 16.7 nM, 167 nM and 1.67 μM), with *$p<0.05$ vs. before stimulation; $p<0.05$ vs. control; $p<0.05$ vs. Cap 1.67 nM; $p<0.05$ vs. Cap 1.67 nM and 16.7 nM. Each datum is expressed as mean SEM (n=100). 46

Figure 3.3 Dynamic characterization of cellular stiffness simultaneously with $[Ca_{2+}]_i$ fluorescence imaging after glucose (16 mM) stimulation. A: The ion channel activities overlaps with the overall cellular stiffness change in the first phase when the onset of stimulation induced rapid structural rearrangement. A second sustained phase follows to maintain the structural configuration and stiffness at a relatively higher level than the baseline. B: A close-look at the lagging of stiffness response compared with that of intracellular Ca^{2+} concentrations, a 2 minute-delay was observed. C, D, E: The fluorescence imaging of $[Ca^{2+}]_i$ before stimulation (C), 12 minutes after stimulation when the light intensity reaches the peak (D), and 20 minutes after stimulation (E) when the light intensity falls to the baseline. 48

Figure 3.4 Dynamic characterization of cellular stiffness simultaneously with $[Ca^{2+}]_i$ fluorescence imaging after capsaicin (16.7 nM) stimulation. A: The ion channel shows similar pulse-shape response pattern as that of glucose albeit with smaller peak value. B: The cells were also pretreated with Capz 30 minutes before capsaicin stimulation to block TRPV1 receptors. No increase in light intensity was observed for TRPV1-blockade samples shown in the normalized gray scale before and after capsaicin stimulation. *$p<0.05$ vs. before stimulation; $p<0.05$ vs. Cap 16.7 nM. C, D, E: The fluorescence imaging of $[Ca^{2+}]_i$ before (C), 12 minutes after stimulation (D) when the light intensity reaches the plateau, and 20 minutes after stimulation (E) when the light intensity falls to the base line. The normalized gray scale value was obtained the same way as the Fig. 3.3. . 50

Figure 3.5 The overall trend of the stiffness responses. A: Glucose stimulation resulted in a two-phase response: a rapid increase phase in stiffness followed by a sustained elevation phase; B: Capsaicin stimulation induced a slow and sustained increase in stiffness. 52

Figure 3.6 The actin filament reorganization after treatment of low glucose based medium as control, 16 mM glucose and 16.7 nM capsaicin for 0 min, 1 min, 5 min and 10 min. F-actin was labeled with CF488A-conjugated phalloidin. The treatment of glucose and capsaicin causes time-lapse change of cytoskeleton especially actin filament structures with distinct patterns. A delayed disorganization of actin around 10 minutes after stimulation was observed in capsaicin treatment, whereas glucose triggered the disorganization 1 minute after treatment, similar with the biophysical data obtained by AFM nanomechanical analysis. No distinctive change was observed for the control sample. 53

Figure 4.1 Integrated SEM and AFM imaging of intercellular adhesion structures. A: Correlation of SEM imaging with AFM imaging. Identically cultured plates of confluent HaCaT cells were fixed and imaged by SEM and Multimode AFM in increasing magnifications. The lower magnification images (SEM: A1, A2; AFM: B1, B2) show the cells with clear boundaries between neighboring cells where cell-cell adhesion occurs. The higher magnification images (SEM: A3, A4; AFM: B3, B4) show details of the adhesion junction with strand-shaped structures in parallel distribution between two cells. 58

Figure 4.2 Integrated immunofluorescence (IF) and AFM imaging of intercellular adhesion structures. The same area on a confluent slide of HaCaT cells was captured simultaneously by IF and AFM after fixation of the cells. For IF imaging, HaCaT cells were labeled with anti-cytokeratin antibodies (red) and anti-desmoplakin antibodies (green). AFM images were captured by Bioscope AFM at increasing resolution with scan sizes of 100 μm (B2), 50 μm (B3) and 20 μm (B4). C: Correlation of IF imaging (C1) with AFM imaging [scan sizes of 100 μm (C2), 50 μm (C3) and 20 μm (C4) after treatment with 10 g/ml of the pathogenic anti-Dsg3 antibody Px4-3 for 24h 59

Figure 4.3 AFM imaging of autoantibody mediated desmosomal disruption in fixed cells. HaCaT cells were grown to confluence, and left with no antibody treatment, or were treated for 24h with (A) the pathogenic anti-Dsg3 antibody Px4-3, (B) non-pathogenic antibody Px4-4, (C) non-binding irrelevant control antibody goat anti-mouse Ig, or (D) irrelevant control antibody 61

Figure 4.4 AFM imaging of autoantibody mediated desmosomal disruption in live cellsconfluent HaCaT cells were imaged live before antibody treatment or treated with the antibodies as in Fig. 4.3 for 30 min, 1 h, 2 h, 3 h, and 4 h 62

Figure 4.5 AFM-guided elasticity measurements on HaCaT cells before and after treatment with anti-Dsg3 and control antibodies. At each time point, between 20 and 40 HaCaT cells were tested, and the force curves obtained from these measurements were processed to generate the corresponding Young's modulus as a measure of cellular elasticity. In parallel experiments, measurement were obtained before antibody treatment and after treatment with 10 g/ml of the pathogenic anti-Dsg3 antibody Px4-3 (B), the non-pathogenic antibody Px4-4 (C), the non-binding irrelevant control antibody goat anti-mouse Ig (D).*p<0.05. 63

Figure 4.6 Cell desmosome disruption by calcium depletion. 65

Figure 4.7 Apoptotic processes are induced by nonpathogenic and pathogenic anti-Dsg3 antibodies 68

Figure 4.8 Apoptotic processes are induced by pathogenic anti-Dsg3 antibodies detected by flow cytometry and AFM nanomechanical analysis. A: No treatment; B: pathogenic antibody treatment and C: pathogenic antibody treatment blocked by FasL inhibitor 70

Figure 4.9 The pathogenic anti-Dsg3 antibody-induced increase in keratinocyte stiffness can be blocked by caspase inhibitor, but not by Fas ligand neutralizer 71

Figure 5.1 Desmosome structure with different desmosomal proteins connecting each other all the way to the intermediate filaments. AFM image and zoom-in (B) correlates with fluorescence image (C) 77

Figure 5.2 Young's modulus comparison for normal and calcium depleted cells . . . 79

Figure 5.3 A: Illustration of composite cell structure during cell indentation and dissection; B: Force-displacement curve without penetration of the cell membrane; C: Force displacement curve with penetration of the cell membrane with the kink zoomed-in in the inset. 81

Figure 5.4 A:The lateral force was the laser position shift in the horizontal direction on the detector; B: The tangent direction of the trajectory defines the angle (θ) between the cutting force F and the lateral force F_l ; C: The trajectory of the nanosurgery on the cell peripheral between neighboring cells with the black triangle indicating the tip position; D: the XY position, cutting force and the Z piezo position in the process of the nanosurgery along the path in C with a cutting depth of 100 nm. 82

Figure 5.5 Nanodissection of intermediate filaments by AFM (before and after) with cross section to indicate the cut-off bundle 84

Figure 5.6 The stiffness response before and after AFM based nanodissection. 84

Figure 5.7 The configuration of the tensegrity structure without intermediate filaments, the black lines indicate the microtubule as the compressive elements and the blue line indicate the actin filament as the tensional elements 86

Figure 5.8 Young Modulus comparison with and without intermediate filaments from simulation based on the structure model 93

Figure 6.1 AFM energy dissipation 98

Figure 6.2 Schematic of QCM-D principle 100

Figure 6.3 The modeling of viscoelastic material under AFM based force displacement measurement during the retract process 101

Figure 6.4 Cell membrane peeling model at the basal area (A, B); and the cell model as a whole (C) in which the cytoplasm was modeled as a Voigt element. . 103

Figure 6.5 AFM energy dissipation measurement on a single cell with and without EGF treatment 105

Figure 6.6 AFM energy dissipation measurement on 100 different cells before and after EGF treatment. 105

Figure 6.7 Dynamic mechanical responses (Energy dissipation) of A431 cells to stimulations with four different concentrations of EGF: 0, 10 nM, 20 nM, and 40 nM 106

Figure 6.8 Dynamic mechanical responses (Hysteresivity) of A431 cells to stimulations with four different concentrations of EGF: 0, 10 nM, 20 nM, and 40 nM 107

Figure 6.9 QCM-D measurement of energy dissipation over time after EGF treatment with concentration of 0 nM, 10 nM, 20 nM and 40 nM 108

Figure 6.10 AFM energy dissipation simulation result shows that it takes longer time for the deformation to recover for a cell with higher viscosity η as indicated with $\eta = 0.45$ showing larger deformation overall. 109

Figure 6.11 Cell peeling model simulation 110

Figure 7.1 The QCM-D/cell focal adhesion energy dissipation model 116

Figure 7.2 A: The initial spring displacement $L_{s0} - L_{sr}$ will be varied according to a Gaussian profile of the oscillation amplitude $A = L_{s0} - L_{sr}$ with the maximum amplitude $A0/2\pi$ of 1 nm and a variance of 3.16; B: Illustration of the sensor disk with manually divided areas with equal distribution of bonds, each was assigned with one amplitude. 121

Figure 7.3 The simulation result at a given initial displacement of 1 nm for a period of 5 μs. 124

Figure 7.4 Dynamic energy dissipation for the three channels 125

Figure 7.5 The energy dissipation channel contribution with respect to the bond number. 127

Figure 7.6 The energy dissipation increases linearly with the bond number. 128

Figure 7.7 The simulation data comparison with the experimental observation 129

Figure 8.1 Diagram of control model of pathway dynamics 135

Figure 8.2 The exponential relationship of the input and output for the plant model. . 138

Figure 8.3 The system of molecules that ODEs were built upon. 141

Figure 8.4 The fitting result for EGF treatment of A431 cells based on the control model. 142

Figure 8.5 Expression levels of MEK1/2, Rho and PLCγ 144

Figure 9.1 EGF stimulated intra and intercellular signaling propagation: A1, no activation; A2, global activation; A3, Local activation. B1, Local stimulation; B2, Intercellular propagation 152

Chapter 1

Introduction

1.1 Overview

Nanobiotechnology, the application of nanotechnology to the characterization and analysis of biological systems is a fast evolving field that represents the intersection of nanoscale physics, biology and engineering [1]. The centerpieces of this technology are the instrumentation and techniques that allow for the sensing and manipulation of nanoscale structures and molecules. One of the key instruments is the Scanning Probe Microscopy (SPM) which measures the near-field physical interactions, mainly van der Waals forces, between the scanning probe and the materials underneath [2]. Atomic force microscopy (AFM), a member of the SPM family, has taken a front seat in driving new developments of nanobiotechnology, and there is now ever-increasing emphasis on applying nanoscale forces to investigate biological events.

AFM was developed by Binnig and Quate in 1986 [3], with the first commercialized AFM available in 1989. AFM remains a high resolution imaging tool mainly used for surface science research, helping researchers visualize materials, such as semiconductors, at nanometer scale [4,5] or even sub-nano meter level to resolve atomic structures. Even today, new material characterizations still rely on the high spatial resolution capability of AFM, such as the identification of single layer graphene [6, 7]. However, the application of AFM in semiconductor and material sciences are being overwhelmed by new breakthroughs in AFM guided biological investigations [8–13]. The extension of AFM into nanobiotechnology relies on its unique working features that are par-

ticularly well suited for biological studies [14–16]. First, AFM can be operated in several environments, including vacuum, air and liquid, the most important of which is the liquid environment where normal physiological conditions for biological matters can be maintained. This is a key factor for AFM studies as compared with other high resolution imaging techniques such as Scanning Electron Microscopy (SEM). Second, due to the nature of its measurement properties, AFM does not require complicated sample preparation where sample contamination and damage can possibly be introduced. For example, electron microscopy requires sample fixation, dehydration and coating processes before each observation. Third, measurement using a sharp probe, as is done in AFM, is less destructive compared with many other commonly used imaging techniques. Furthermore, AFM measurement in stable conditions delivers a relatively high signal to noise ratio (SNR), allowing high image resolution at the nano and even sub-nano meter scale. With this level of resolution the membrane structure of single cells, single proteins and DNA molecules can be visualized in unparalleled detail.

The AFM tip can be controlled to mechanically pull, push and manipulate nanoscale objects, working as a nanorobotic arm under precise computer control. Therefore, traditional concepts in robotics such as feedback, stability, and frequency response can all be integrated into these miniatured nanorobotic systems. AFM based nanorobotics has been a tremendously useful tool in nanomanufacturing, as demonstrated by its ability to perform nanolithography, nanoassembly and manipulating nano particles [17–19]. In biology, nanomanipulation using the AFM based robotics system has substantially extended the reach of AFM in various biological fields. One such application is to functionalize the AFM tip to conduct so called single-molecule manipulations. Single strand intermediate filaments have been stretched by a controlled AFM tip to measure their tensile strength [20]. Nanosurgery has been performed on cell associated molecules with a resolution of less than 100 nm [21]. Individual DNA and protein molecules have been manipulated. The term

single molecular force spectroscopy (SMFS) has been applied when using the technology to probe forces at the molecular level on surface membranes [22, 23]. The cellular response to varying physiological conditions is often manifested as alterations in cellular mechanics. A recent AFM study [24] has shown that during apoptosis cytoskeleton elements such as actin filaments will form a thick layer wrapping around the collapsed nucleus, thus resulting in a time lapse stiffness change; first a decrease and then an increase. Dynamic mechanical properties such as elasticity and viscoelasticity can be revealed by AFM and may serve as biomarkers, or even regulators of signaling events and physiological processes. Furthermore, AFM allows these changes in biological structures to be visualized through high resolution images. Thus, AFM based nanorobotic operations are proving to be an exciting and novel technology that may be uniquely suited for the capture of biologically relevant information linking mechanostructural and functional events.

1.2 Sensing techniques

1.2.1 Structural sensing and force sensing

The imaging principle of AFM is relatively simple. A cantilever with a sharp tip is operated to scan across the sample surface to probe its topography. The main functioning unit is the piezoelectric actuator which drives the cantilever both horizontally, the XY scanning direction, and vertically, the Z motion direction. During the XY scanning, the interaction force (mostly van der Waals forces and sometimes electrostatic forces) between the scanning AFM tip and the sample surface will cause the bending of the cantilever. A laser beam which is reflected from the back of the cantilever is able to record this bending with a position sensitive device (PSD). The Z piezo will move accordingly to keep the tip at a constant oscillation (tapping mode) or in contact with the sample (contact mode). A schematic of the working principle of AFM is shown in Fig. 1.1. By

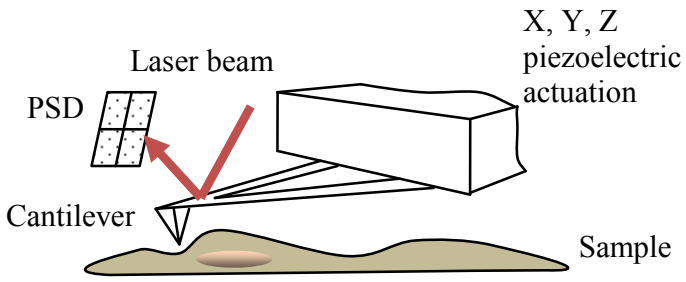

Figure 1.1 Schematic drawing of AFM working principle

this simple mechanism, complex biological structures can be visualized with nanoscale detail. When imaged in liquid, biological samples are often rendered soft and delicate. Therefore, the contact force must be well controlled to avoid damage to the sample surface. Typically for contact mode AFM imaging, the applied force should be adjusted to less than 100 pN for live cell imaging (this value varies for different cell types). At this interaction force, the deformation of the cell membrane can be recovered [25]; any force larger than this value would pose potential irreversible damage to the cell membrane and cytoskeleton. However, the applied force can also be used to highlight the stiffer structures underneath the soft cell membrane. In this case, the AFM tip will press against the soft cell membrane into the cytoplasm until the membrane is supported by the underlying filaments structures, allowing the underlying structures to be highlighted in both the topography and deflection images. The most important aspect for this imaging mode is to accurately control the applied force.

Not only is the normal force applied by contact mode a potential damaging factor for biological samples, but the lateral or frictional force that "scratches" the surface must also be considered. The development of tapping mode AFM imaging has proved a good solution to this problem [26]. By oscillating the cantilever at its resonance frequency in liquid with a pre-defined amplitude, the sharp tip at the end of the cantilever is free of contact with the sample. The interaction force between the sample and the tip reduces the oscillation amplitude and also induces a phase shift.

By controlling the vertical piezo to maintain the desired amplitude, topography information can be obtained. In fact, the phase shift provides indirect, quasi-quantitative data for mechanical property analysis.

The ever-developing techniques for AFM imaging of biological samples have led to a number of breakthroughs in the biological sciences. The surface structure of bacteria cells was visualized with lateral resolution around 2 nm with an applied force around 80 pN [27]. Membrane protein structures have been revealed with tetramer configurations at sub-angstrom resolution in the vertical direction. Animal cells have been imaged live to obtain structural information on cell membranes or underlying cytoskeleton structures [28]. At an even larger scale, cartilage tissues were imaged to determine their fibril composite [29]. These experiments truly demonstrate the spatial resolving capability of AFM for biological materials under physiological conditions; in some cases this has been used to confirm crystallography data for defined structural conformations.

The live cell images in Fig. 1.2 show the topography and the surface detail of keratinocytes in phosphate buffered saline (PBS). The cytoskeleton beneath the cell membrane was highlighted by the applied force, revealing actin filaments at the center of the cell and intermediate filaments at the peripheral connecting neighboring cells.

1.2.2 Structural sensing at the cell level

1.2.2.1 High resolution imaging by fluorescence imaging

Several studies have utilized a combination of AFM with optical microscopy techniques to localize desired targets (schematically shown in Fig. 1.3). For the majority of these studies, AFM is used to image the topography of a sample while a fluorescence image is collected simultaneously. The fluorescence image is used to guide the AFM tip to certain locations where a specific agent is

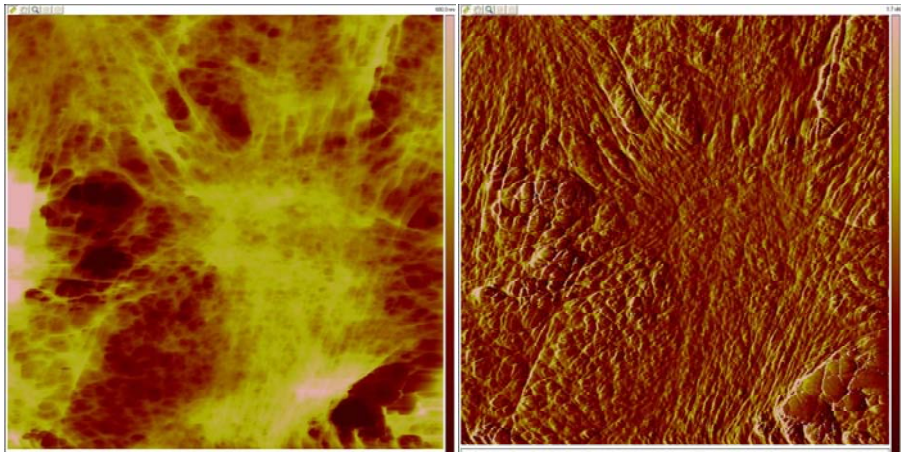

Figure 1.2 High resolution images showing the cytoskeleton structure under the applied peak force of 5 nN, scan size: 30 μm.

labeled, allowing detailed structural images to be obtained around the labeled molecule. In other cases, the AFM tip is employed as a mechanical device to manipulate the sample while at the same time conducting fluorescence imaging. A few papers have examined the mechanical properties of single molecules by using AFM to stretch them and simultaneously visualize the stretching process by fluorescence imaging [30]. However, a concern with this combination of techniques is the interference between the excitation light and the emission light from the fluorescence microscopy and the laser for AFM deflection recording. The laser used for cantilever deflection detection has a wavelength in near infrared (NIR) ranging from 700 to 1200 nm [31], while in most cases fluorescence excitation and emission wavelength is less than 700 nm, in the visible light range space; for FITC the excitation and emission wavelengths are 480 and 560 nm, respectively shown in Fig. 1.3.

1.2.2.2 Scanning Electron Microscopy (SEM) imaging

If we consider the combination of fluorescence imaging with AFM to be more of an instrumental combination, then AFM combined with SEM could be considered as a functional combination. A

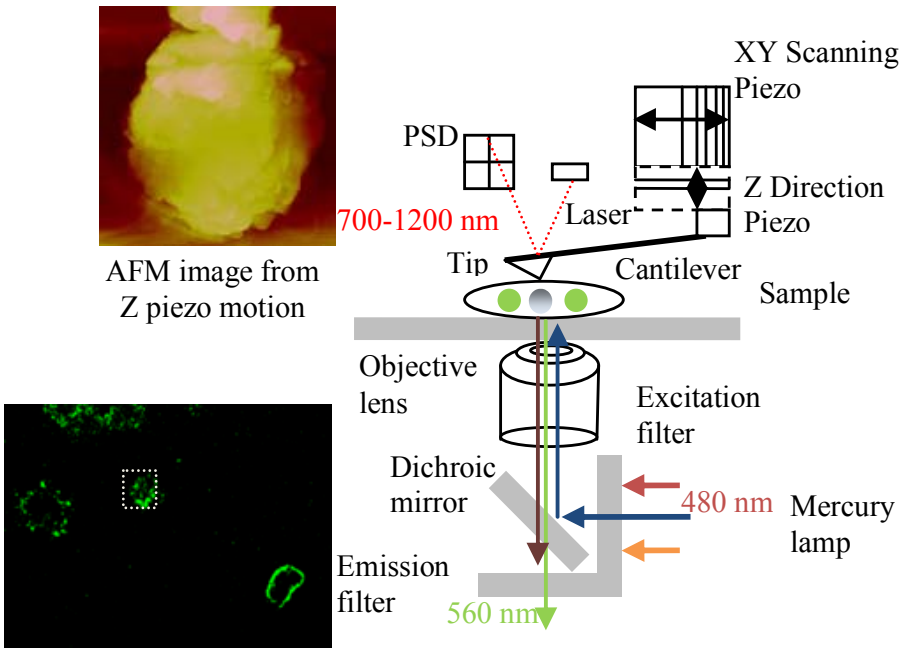

Figure 1.3 The combination configuration of fluorescence microscopy with AFM. Simultaneous imaging of B lymphoma cells labeled with anti-CD20 (FITC labeled) surface receptor and the AFM is shown.

few investigators have used SEM to confirm structures observed in AFM. SEM has much larger scanning area, and thereby can be used to complement the AFM measurement. In one study, SEM was operated in low acceleration voltage to observe vesicle structures on the cell membranes [32]. Vesicle pits normally contain a substantial amount of water. Thus, when imaged by AFM under low loading force, the pit structure may not be elevated. Only when a certain contact force is applied on the surface can the pit be visualized with higher contrast between the water-filled area and the unfilled area. However, this pit structure can be directly observed under SEM. Before SEM imaging, samples need to be dehydrated. Therefore, the water containing vesicles will be highlighted after shrinkage due to the drying process. The inhomogeneity of the membrane surface can then be confirmed.

1.2.2.3 Stochastic optical reconstruction microscopy (STORM)

A recent advancement of fluorescence microscopy has enabled, in principle, the optical imaging that reaches molecular scale [33], which was prevented by light diffraction in traditional optical imaging. The technique, STORM, short for stochastic optical reconstruction microscopy employs fluorophores that can be switched on and off at different measurement cycles to enable the precise measurement of positions of subset of fluorophores. When a subset of fluorophores was switched on, it effectively eliminates the light overlapping and allows the positions of fluorophores to be determined precisely.

1.2.2.4 AFM with Raman spectroscopy

The combination of AFM with Raman spectroscopy was introduced approximately ten years ago termed as tip enhanced Raman spectroscopy (TERS) [34]. This method takes advantage of the high spatial resolution of scanning probe microscopy to obtain topography images while performing surface chemical sensing at the nanoscale. The AFM tip is coated with metal (normally silver) to further enhance the Raman signal. When the laser is irradiated onto the metal surface of the AFM tip closely engaged with the sample surface, field- enhancement occurs to excite molecules around the tip that allows Raman spectroscopy with a higher lateral resolution as compared with surface enhanced Raman spectroscopy (SERS). The most common application of TERS in bio-imaging is to chemically characterize biomaterials [35]. Further development and refinement of this method is required before it can be routinely applied to more complex biological samples and processes.

1.2.3 Nanomechanical sensors for biological detection

The capability of AFM was further enhanced by the introduction of other modes of detection, e.g. capacitance, resistance and magnetisms. These detection modes leverage on the scanning capabilities of AFM while provided new dimensions of information as sensors. Recently, the development of micro- and nanoscale cantilevers utilized the same physical principle introduced new flexibility as well as accuracy to the sensing of physical interactions at the molecular level. Meanwhile, other type of sensors are trending towards the label free detection of force interactions during biological processes, such as optical and acoustic sensors.

1.2.3.1 Cantilever arrays and nano-resonators

With the similar concept as in an AFM, microfabricated cantilevers have been contributing in the detection of various biological phenomenons [36–38]. The versatility of cantilevers have been demonstrated with mechanical, electrostatic or piezoelectric drives and detections. The nature of these devices as nano-resonators enables them to sense extremely small mass changes or force interactions, thus a high sensitivity is guaranteed in the detection of gases, chemical compounds, biological receptors or DNA hybridizations. With the introduction of multi-cantilever arrays [39], the limitation of low throughput has been effectively overcome. There have been cantilever arrays coated with sugar contents for the detection of certain mutations in cancer cells [40], and nano-resonators monitoring the response of bacterial cells to specific antibiotics [41]. However, most of these applications demonstrate exceptional accuracy in air, once working in liquid environments, the viscous drag of the fluid will significantly reduce the quality factor of the sensor, rendering it ineffective in numerous cases [42].

1.2.3.2 Traction force microscopy (TFM)

The label free detection of physical forces at the cell-cell and cell-extracellular matrix (ECM) interaction poses another set of applications for nanomechanical sensors. The force interactions at the cell-ECM have been reported to regulate the normal growth of the cell, migration, metastasis and so forth through the focal adhesion-orchestrated cell signaling pathways [43]. Thus to quantify and map out the distribution of cell-ECM interactions is crucial to the understanding of the molecular mechanisms underlying the regulation processes. TFM utilizes the optical property to monitor the substrate displacement caused by the cellular traction forces. The displacement normally is revealed by the fluorescence beads that are embedded into the substrates and are coated with ECM binding agents. It could provide the three dimensional force profile of the cell-ECM interface [44].

A special group of force measurement at the cell-ECM adhesion sites uses microfabricated pillars [45] with same geometrical structure but different length, thus different elasticity, to indicate the displacement caused by traction. The variations in matrix elasticity have been reported capable of directing the differentiation of stem cells [46]. These revealing techniques, though effective, will pose a different growth environment for cells from their natural inhabitant, or even from the long established two dimensional petri-dish based culturing system. Thus, the effect may very well be the

1.2.3.3 QCM-D detecting energy dissipation in cell adhesion

Quartz Crystal Microbalance with Dissipation (QCM-D) is another nanomechanical senor that could measure interactions at the molecular level [47]. It has been used for molecular recognitions, such as membrane formations [48], protein adsorption [49], and cell spreading [50]. It operates at thickness-shear mode by oscillating a quartz crystal disk with high frequency (normally 5 MHz)

and low amplitude (less than 1 nm in lateral direction). It collects the frequency and amplitude changes of the quartz crystal and reveals the mechanical/structural status of the sample attached on top of the sensor disk: the shift in resonance frequency indicates the mass absorption or loss; while the energy dissipation alteration could be used to derive the viscoelasticity property of the adsorbed film on the disk [51, 52].

1.2.4 Force sensing at the cell level

Mechanical properties of structures can be characterized by recording force displacement curves via AFM nano indentation. Following Hertzian model analysis of force curves, a quantitative Young's modulus can be generated. For this purpose, the AFM tip is driven by piezoelectric actuator along its Z direction towards the sample and then retracted back over a pre-defined distance. The movement of the piezoelectric actuator is then used to drive the AFM cantilever vertically and the deflection signal from the cantilever is recorded as a force-displacement curve.

1.2.5 Force sensing at the molecular level

1.2.5.1 Tip functionalization based on self-assembly

Functionalization of AFM tips by coating them with antibodies or ligands has extended the application of AFM for studying specific interactions at a molecular level, e.g. binding force for molecular interaction or molecular recognition. The functionalization process is mainly based on the self-assembly ability of chemical agents at molecular level. There are three ways to functionalize the AFM probes with functional agents. The simplest method is by direct coating of a functional protein to the AFM tip. While this is not technically difficult, the binding strength here may not be strong enough. A common strategy to improve the binding is to employ certain crosslinking

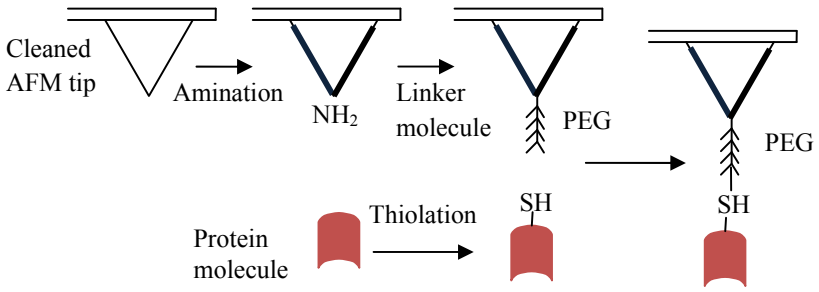

Figure 1.4 Tip functionalization with the intermediate linker molecules.

reagents to link the functional agents onto the AFM probe. The intermediate linking method is a much more complicated procedure, but it results in a larger binding force between the AFM tip and the functional agents. It also provides a higher degree of spatial specificity. This functionalization method usually employs a linker to covalently bind the proteins in order to expose specific site(s) within selected molecules. Polyethylene glycol (PEG) is a common crosslinking reagent. A terminal thiol group can be first attached to the antibody or protein and this thiol group will be able to covalently bind to PEG [53]. The AFM tip should be cleaned and processed to add an amine group layer, which can then be cross-linked to PEG. This functionalization process is schematically shown in Fig. 1.4. One of the most common ways to functionalize the AFM tip is by the formation of Self-Assembled Monolayers (SAMs) [54]. The formation of SAM is achieved by thiol chemistry, similar to the coating of polymer PEG. After the initial binding of thiol with gold, the large space between molecules enables the thiolyated alkyls to be horizontally oriented. As the density of the horizontally aligned alkyls increases, the lateral interaction through van der Waals forces drives the alkyls to lift off and finally align upright as depicted in Fig. 1.5.

1.2.5.2 Single molecule force microscopy (SMFM)

The AFM tip was first brought into contact with the cell sample (Process A in the Fig. 1.6). When there is affinity binding activity between the ligand coated AFM tip and the surface receptor, the

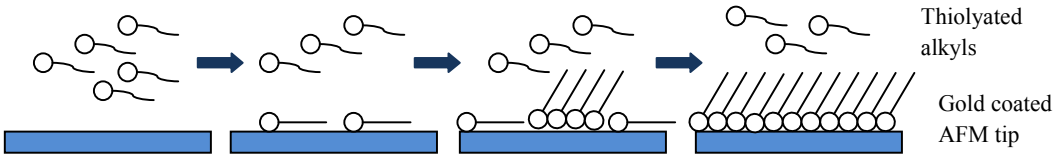

Figure 1.5 SAM formation onto goad coated AFM tip.

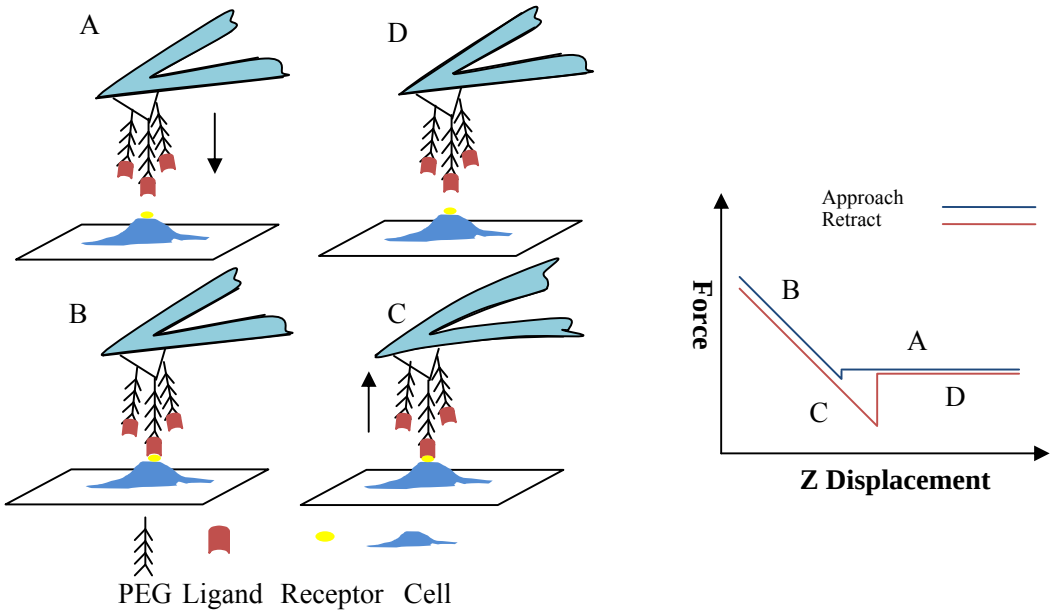

Figure 1.6 The binding force measuring process.

adhesive forces dominate the interaction between the AFM tip and the sample below (Fig. 1.6B). When the cantilever is pulled back from the sample, the adhesive interaction drag back the cantilever and this is detected by the high sensitivity cantilever bending (Fig. 1.6C). The bending of the cantilever through the whole process A to D is recorded as a function of the vertical displacement of the piezo drive. From the force distance curve, this dragging effect can be calculated as the force difference between the baseline and the minimum. Normally, drag effect always exists when the AFM cantilever pulls back from the sample due to the van der Waals force, but the force is quite small. To obtain the binding force for single bonds, more detailed analyses would need to be performed.

1.3 Cell signaling pathway

Cell signaling is a system of communications that governs various cell activities. The ability of cells to perceive the environment and respond accordingly determines the development and the fate of the related cellular system, the malfunction of which would cause serious consequences, diseases such as diabetes and cancer. Cellular signaling pathways have been studied extensively in biological context using traditional methods such as protein pooling. Epidermal growth factor (EGF) is a ligand for a cell surface receptor epidermal growth factor receptor (EGFR). Its activation by EGF can trigger a cascade of downstream signaling events. The A431 human epidermoid carcinoma cell line has been widely accepted as a model for this type of studies. The EGF stimulated A431 cells have been reported to exhibit significant rounding and stiffening, a phenomenon caused by cytoskeleton reorganization governed by cell signaling. We previously reported that these changes could be detected by AFM based mechanical measurements, in which both cellular stiffness and energy dissipation increased. Thus we conclude that a mechanical biomarker could be successfully established to signify the EGF stimulation and activation. Systems biology studies normally try to map out the underlying structure of cell signaling network and the flow of signal cascade. These networks are quite complex in their organizations. By far the traditional reductionist approach has failed to elucidate the decisive signaling reactions and molecules that are responsible for the cellular functions, which are often integrated outputs of multiple signaling pathways. A quantitative understanding of regulation of cellular functions is also seriously lacking. Thus, it becomes necessary to introduce computational modeling approach at the system level to examine cellular functions in order to determine the responsible properties and interactions of the cellular components and assess how these components work together to generate an integrated downstream signal output in response to various extracellular cues.

1.3.1 Models of molecular kinetics

In post-genomic research, high-throughput gene and protein profiling techniques have enabled the monitoring of biological systems in terms of expressed gens and proteins in real time at reasonable cost, and these information have helped people identify the signaling cascaded in various biological process. The identification of pathway could take a different tone as in a sequence of enzyme-catalyzed reactions of small molecules or signaling propagation though a set of protein phosphorylation reactions and gene regulations. The investigation would thus involve the analysis of protein-protein physical interaction, the kinetics simulation of small molecules or the steady state pathway analysis.

1.3.2 Michaelis-Menten reaction

Enzyme kinetics is at the center of all the singling cascade events. Enzymes are highly specific catalysts of biological systems and accelerate the chemical reaction of molecules to ensure the proper propagation of signals, and biological reactions do not occur at perceptible rates in the absence of enzymes.

When a signaling transduction reaction is catalyzed by an enzyme, the enzyme (kinase or phosphatase) is not consumed or produced by this reaction, but it may form a temporary complex with the substance in the reaction. For such a reaction, we can use Michaelis-Menten kinetics to describe its reaction rate under the key assumption of quasi steady state approximation, which is valid when the enzyme concentration is much lower than the substrate concentration and when the enzyme is not allosteric. Michaelis-Menten kinetics is named for Leonor Michaelis and Maud

Menten and has the following formulation:

$$v = \frac{v_m S}{k_m + S} \tag{1.1}$$

in which v is the rate of reaction and S is the concentration. v_m and k_m are maximum reaction rate and Michaelis constant, and k_m equals the substrate concentration that leads to the reaction rate of $\frac{v_m}{2}$.

1.3.3 Pathway regulation of cell adhesion

EGF is a compound that can bind to the cell surface receptor, EGFR [55]. The binding will trigger a series of signaling cascades that have complicated effects and implications in the normal function of cells. Specifically, the EGFR pathway could regulate cell migration, growth and proliferation in normal physiological conditions; while in pathological conditions, it is reported to be closely associated with the metastasis of certain cancers [56]. The EGFR pathway has been shown to be an extremely complicated interconnected network recruiting and involving numerous intermediate molecules [57]. One of the essential consequences of EGFR signaling is the regulation of cell motility through the promotion and inhibition of assembly or disassembly of focal adhesion complexes [58], or the so called cell-extracellular matrix (ECM) adhesion. Overexpression of EGFR has been associated with cancer metastasis which are featured by compromised cell adhesions. Thus it is of paramount interest to dissect the signing pathways that regulate the cell adhesion after EGFR signaling.

The focal adhesion complex comprises of discrete sites where physical contacts between the cell cytoskeleton and the ECM, extracellular tissue that mainly composed of interlocked fibrous proteins, are established. The foundation of the physical entanglement starts from the binding of

integrin molecules of their extracellular domain, a transmembrane receptor, to the RGD sequences in the ECM (Fig. 1.7A). This binding will recruit a number of proteins in the intracellular domain to tether the integrin molecule to the actin filament, one of the three cytoskeleton elements. Thus, a change in the adhesion site, binding/unbinding of integrin molecules with RGD sequence, assembly/disassembly of focal adhesion complex, adhesion/deadhesion of cell motility, will essentially tip the delicate balance established between the cell cytoskeleton and the ECM [59]. The focal adhesion was visualized as discrete sites of contact as shown in Fig. 1.7B and the cell structure was captured by AFM live cell imaging in Fig. 1.7C. This biophysical process has been investigated from the ligand-receptor binding dynamics perspective. Most of these models are derivations of the thermodynamic framework pioneered by [60]. The biophysical property of cell adhesion emerges from the delicate equilibrium of integrin-RGD binding, where the stochastic bond formation and dissociation rates were expressed in the form of thermodynamics and the load bore by the integrin-RGD bond. A number of models have extended the reach of the Bell model to more complicated scenarios, such as the cell membrane peeling model when the blood cell in rolling motion through the vein and these extended models have exert influence on the understanding of cell spreading, migration, proliferation and differentiation [61].

The regulation of cell adhesion by EGFR signaling pathways has been reported to work through three branches of cascades and their inter-branch crosstalks: the phosphoinositide 3-kinase (PI3K) pathway, the mitogen-activated protein kinase/extracellular signal-regulated kinase (MAPK/ERK) pathway, and the phospholipase C (PLC) pathway [62]. Significant progress has been made since the discovery of EGF and EGFR, resulting in the identification of key molecules in these pathways. Nevertheless, the complexity of these pathways and their crosstalks prevents the full understanding of impacts of each pathway to the adhesion/deadehsion process, and ultimately cell motility and migration in a bigger picture [63]. From the intricacy of the pathway dynamics it also raises

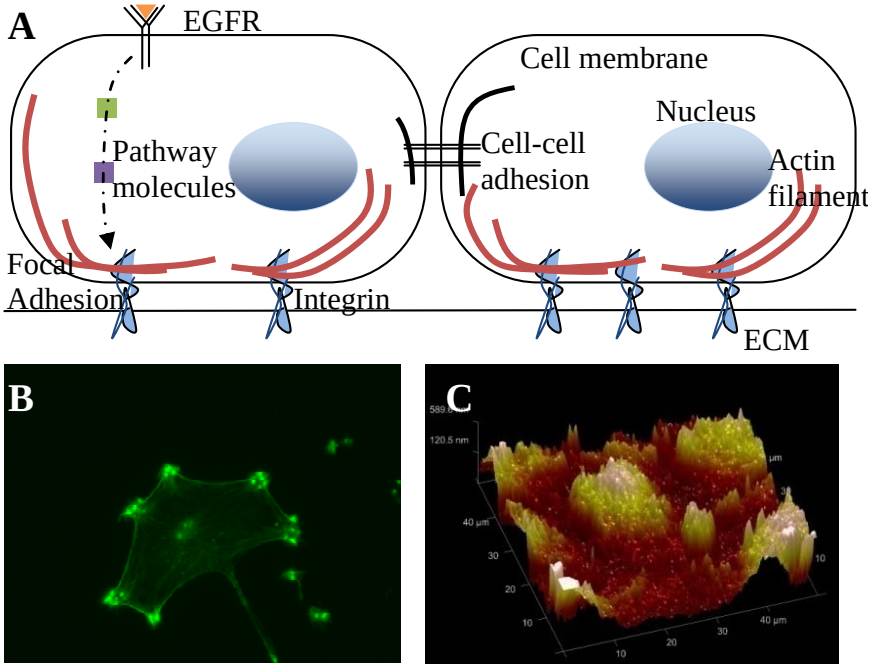

Figure 1.7 A: The diagram of cell adhesion regulation pathways. B: Image of focal adhesion by florescence. C: AFM image of the living cells with focal adhesion complex.

the nonlinearity issues that are inherent to the various feedback and feedforward loops prevalent in these networks of molecules, issues of paramount interest to the modeling and control community [64].

To understand these exquisite balances of molecules in the process of cell motility regulation, system biologists often refer to the computational modeling techniques at the system level to elucidate the steps and molecules, and try to assess quantitatively the rise and fall of these molecules in terms of expression level or concentrations at each step, as well as break down the contributions from each component during the dynamic interactions [63]. The resulting product is computational models written in the form of ordinary differential equations (ODE) derived from the reactions of chemical species based on the kinetics of reaction with knowledge of sets of rate constants. This approach has produced a number of well-defined pathway structures for various aspects of EGFR signaling [65]. To analyze the modeling results and verify them by experiments, however, requires

significant amount of biochemical assays, which are often time consuming themselves.

To circumvent the problem, researchers have proposed a paradigm-shifting methodology to integrate the biophysical model of cell structure and its dynamic remodeling and reconfiguration process with the control and regulation from the signaling cascade upon stimulation by various extracellular cues. The only concrete model so far that has been proposed for mechanistic regulation of cell adhesion by signaling pathways was developed by [66]. The Rho pathway was considered in the model as the main regulator of cell adhesion and the level of enzymatic activities were converted to applied load similar as the Bell model. The lack of components from other key molecules poses a challenge for the general acceptance of the model. The linkage between the expression level of Rho and the applied load to the molecular bond is debatable.

The physical properties of the focal adhesion and its impact on the cell mechanical property as a whole provide unique peek into the end product of the signaling pathway controlled cell adhesion. The mechanical characterization of the strength of focal adhesion by an oscillating sensor and its implication to cell mechanical state by AFM probing has been reported previously [67]. The relationship between the size of focal adhesion and the readout from the QCM-D sensor has been elaborated [68]. Thus to build an integrated EGFR signaling/cell adhesion model, we tried to shed the light from the system control perspective, in which the cellular physical state and its interaction with the nanomechanical sensor are deemed as the micro and nano mechanical system under the control of the signaling pathway cascade. Leverage on the unique capability of QCM-D which can provide real-time continues mechanical measurement, a mechanical model can be built as the plant, and then various signaling pathway structures and molecular interactions of different rate constants and parameters can be put on trial against the real-time data as to verify their legitimacy and accuracy.

1.4 Objectives and challenges for AFM based nanorobotics integrated platform

AFM applications are providing increasing insights onto biological processes that are otherwise not offered by other techniques. With its unique operating environment, AFM high resolution structural imaging and nanomechanical measurement provide real-time structural and functional information during the course of biological events. AFM imaging can be combined with other imaging modalities such as florescence imaging and electron microscopy to boost its capability. Furthermore, with the introduction of robotic concepts nanobiomanipulation can be performed on single cells, DNA molecules and membrane proteins. However, there are still technological challenges that need to be solved for even more precise monitoring of biological phenomenon. AFM nanorobotics is not merely an extension on AFM, although some AFM could also perform nanomanipulation, these systems lack the human interface and the precision control in position, velocity and force, trademarks of traditional robotics.

Thus nanorobotics could be a replacement of AFM, since it integrates the basic elements together: normal imaging, area survey with compressive sensing based fast scan, and manipulation with human interaction and position/force feedback. With these control capabilities, the nanorobot can have a workspace of nanoscale, but the controllability of a traditional robot. Thus, the handling of matters in the nanoscale would be achieved with stability, accuracy and efficiency. The AFM nanorobotic system provide the human-directed position, velocity and force control with high frequency feedback, and more importantly it can feed the operator with the real-time imaging of manipulation result from the fast-imaging based local scanning. These technical advantages is crucial to the success of nanobiomanipulations. Firstly, human directed control with a haptic device can ensure that the survey fashion of measurement of binding force and local mechanical properties

can cover larger area and more precisely location wise. Secondly, three-dimensional force control can provide the manipulation force tailored for different biological matters. Velocity control can measure and extract the dynamics nature of biological materials than a static measurement model.

Last but not least, a fast imaging system to scan locally of the surrounding area could provide the operator an updated image of manipulation result in real-time, a necessity in situations where the temporal resolution of biological processes is in the minutes or even seconds. Biological events are normally time sensitive. Most of these processes occur much faster than the time it takes to capture a full frame AFM image. Therefore, a continuing goal is to improve temporal resolution while maintaining spatial resolution. The use of high-speed AFM to track macromolecules may be useful for this purpose [69]. Future exploration may include developing AFM imaging modalities correlated with a series of newer techniques to capture more precise biomarkers for various biological processes.

AFM based nanobiomanipulation requires *in situ* sensing while the manipulation operation is being performed. Thus, the AFM process needs to be able to switch between imaging mode and manipulation mode periodically with high frequency during manipulation. In manipulation mode the AFM tracks the operator input, while in imaging mode it performs in a zigzag motion allowing the effect of the operations to be visualized simultaneously. Dual probe systems have also been proposed in which one cantilever performs the manipulation while a second cantilever senses the manipulation. This technique may be particularly useful for experiments involving local drug delivery or site-specific nanosurgery [70]. Multiple probe sensing arrays have also been envisioned to enhance the capacity of AFM readouts [71]. These exciting new developments in AFM suggest that we are on the cusp of revolutionary technologies that will no doubt open unforeseen windows into the mechanism of cellular and molecular process that underlie normal physiological as well as disease states.

1.5 Organization of the Study

The first half of the study used AFM based nanorobotics and other imaging modalities such as SEM, Fluorescence imaging and force measurement to characterize the role of cell-cell adhesion (in the form of desmosome) plays in the cell model that we described as the tensegrity. The static model will only provide the qualitative evaluation of the relationship between cell mechanical stimulation and the response. Thus we sought to build a dynamical model to address both the structural dynamics and ultimately the molecular dynamics. The second half of the study mainly focused on the development of AFM nanorobotics and QCM-D nanomechanical sensing in the identification of signaling pathways that mainly modifies the cell-ECM adhesion. The study verifies the important role the cell-ECM plays in maintaining the cell force balance in the process of cell physiological conditions. In the mean time, the study would also provide the use of this model and characterization as a screen tool used to replace the messy biochemical characterizations such as protein blotting. Therefore, this technique would provide the real time dynamics of the molecules in the regulation of cell-ECM adhesion. This would predict how the protein dynamics follows certain biochemical stimuli *in situ*.

Chapter 2

Nanobiomechanics in the identification of pathophysiological conditions

2.1 Introduction

Nanobiomechanics is an emerging field of study with the aim of understanding the mechanics governing the various biological, especially cellular processes [72]. It started off with the study of tissues and their mechanical behavior , thus so called biomechanics [73]. As the development of nanotechnology enables the detection of forces at the nanometer scale, the field of biomechanics has gradually derived a new frontier in nanobiomechanics, in which the study focuses on cells, or even molecules [74].

This development has opened up the research in biological science with new possibilities. The study of nanobiomechanics thus mainly evolves around the physical forces as small as a pico-Newton -a trillions of a Newton. These physical forces govern, however undiscernibly, all the biological process that happens in every instant in the cells. They work in every facet of the cell life cycle, including the bindings of molecules, which are normally regarded as chemistry or biochemistry, and the growth and migration of cell body, in which the physical force could be the regulator or the indicator, as well as the formation of cells into tissues, i.e. tissue morphogenesis. The field of nanobiomechanics, setting in this context, aims to decipher of the underlying mechanism of forces in the regulation of cellular processes, and to mark the pathological state of cells

which would aid the diagnosis of diseases. For instance, the malaria infected red blood cells were distorted and have difficulty passing through blood vesicles [75], and certain type of cancer cells are 70 percent softer than their original phenotypes for the aid of metastasis [76].

2.2 Cell Mechanics

The study of cell mechanics is a subset of nanobiomechanics and they have taken on a new name, mechanobiology [77].The understanding of the mechanical behavior of cells have been closely associated with, or more precisely limited by the signatures of the techniques used for the characterizations.The engineering methodologies that have been driving the study of the cell mechanics have evolved from micropipette aspirations to optical and magnetic twisting, and AFM probing. The unique capabilities and shortcomings of each technique define what the research consider as a proper structure the cell should be and which model could best depict these structures and behaviors. Thus, each technique would be limited by their can and cannot dos, which resulted in the unfulfillment of understanding the whole picture. The models that followed the techniques have also evolved from liquid drops to composite viscoelastic materials and finally to a interconnected network of strings and struts encompassed by a membrane.

2.2.1 Membrane, Channels and Cytoskeleton

The cells, now we know, is a complex network of structures. The outmost layer is a semi-permeable membrane, composed of drifting islands of lipid bilayer, hosting a range of receptors and ion channels that can take the input of chemical signals and direct the influx and outflux of ions, as well as manage the transportation of proteins in and out of the cell. The cytoplasm contains fluid as media for the various biochemical reactions to take place as well as the cytoskeleton, and the

nucleus sits in the center of the cell and is composed of condensed chromosomes. The shape of the cell is mainly determined by the intracellular cytoskeleton, since the lipid bilayer membrane is extremely delicate and could not bear any load, thus it could not maintained a defined shape without the underlying support of the fiber-intensive cytoskeleton structures.

The easiness of bending of membranes is reflected by the bending modulus, which is in the range of 10^{-19} J. However, the low bending modulus dose not prevent the membranes to be a material difficult to extend or compress in the lateral direction. The lateral compressibility of lipid bilayer is in the range of 100-200 dyn/cm as determined by X-ray diffraction [78].

The ion channels are pore-forming proteins on the membrane. Their main functions include maintaining a resting membrane potential and control the ions flows across the membrane, as well as regulating cell volume. They can either controlled by voltage, i.e. voltage-gated, or by ligands, i.e. ligand-gated. Or they can be classified based on the types of ions they are directing, such as potassium or sodium channels. The gating of ion channels are closely related with the membrane mechanics as well as the cytoskeleton mechanics. The conformational changes undergone by transmembrane ion channels in response to stimuli will pose a certain amount of free-energy in the range of 10 k_BT in the case of voltage gated channels [79], which would cause the subsequently deformation of the lipid bilayer. The endocrine secretion cells would also experience major cytoskeleton changes, i.e. actin congregation at the site of granule secretion [80].

The cytoskeleton structure maintains the mechanical integrity of the cell structure. The microtubule, actin filament and intermediate filament are the three types of filaments that run through the cytoplasm, connecting the membrane, the nucleus and holding the functioning unit in the cytoplasm together. These protein fibreous structures are with the diameter of a few to tens of nanometers. They form a inter-connected network which defines the mechanical response from external load and the mechanical response in the normal and disease conditions when probed. They are

responsible for the establishment of cell-ECM contact through actin filament and they also coordinate the inter-cellular connection with neighboring cells through intermediate filaments.

2.2.2 Mechanical model of cells

Cells constantly receive mechanical stimuli from the external environment as well as from the internal signaling regulation [81]. Thus, mechanical cues can be crucial regulators of biochemical processes that govern the cell fate. In the mean time, cell would also display certain mechanical status at certain stages of their development or in pathological conditions [82]. From this perspective, mechanical states of the cell could also be used as biomarkers for the identification of cell pathophysiological conditions. To utilize these information, however, requires the detection mechanisms that have both high spatial and temporal resolution, such as an instrumentation based on AFM and QCM-D. Besides, the interpretation of these mechanical information requires the modeling technique that could take advantage of them.

The main cell mechanical models are divided into two different categories [83]: one is the micro/nano structure approach for a cytoskeleton based cell structure model that mainly used for adherent cells [84, 85] and only occasionally for suspended cells [86]. For cytoskeleton based cell models, the cell would establish force balance through the interaction of the cytoskeletal network and their interaction with the extra cellular matrix and/or the neighboring cells. Therefore the cell is a discrete network of structures, bounded by the cell membrane that bears most of the force. The cell membrane will not bear any forces that are significant enough to cause any deformation or distortion of the cell body.

2.2.2.1 Continuum models

The early use of a micropipette aspiration in the study of cell mechanical property provoked a series of models that consider the membrane as a incompressible layer and the material inside the membrane as Newtonian fluid. This approach along with other that treat the cell as a composite material all took the continuum mechanics methodology. The overall cell model was governed by one constitutive equation.

The continuum mechanics [83] implores the material properties of the cells by considering them as a composite material. It bears no condition for the cell biochemical processes since the cells are consider as no different to a non-living composite material, either pure elastic or viscoelastic. Through experimental observations, proper constitutive equations can be built, and then the related parameters can be identified. It is easy to derive and straightforward but the continuum mechanics approach will not shine any light onto the detailed biochemical and molecular mechanisms underlying the cell mechanical states. Nevertheless, the parameters and characterizations of distribution of stress and strain would provide more insights in building the micro/nano structure models that would link the mechanical behavior and the cell biochemical processes. Continuum mechanics models are normally divided into solid models [87], which consider the cell a single material of either elastic or viscoelastic properties and cortical shell-liquid core models which consider the cell as a viscoelastic material that enclosed inside a elastic membrane [88].

The viscoelastic models include the liquid drop models and the solid models. The liquid drop model suits the early researches using micropipette as a manipulation and measurement tool. It was developed by Yeung and Evans to describe the flow of the Leukocyte into the micropipette with a slightly smaller diameter than the cell [88]. It considers the membrane or cortex as a fluid layer with a constant tension and the cytoplasm as a Newtonian liquid droplet. The ensuing studies

have proposed different constitutive equations for the liquid drop inside the cortex, such as the compound liquid drop with an additional layer of cortex for the nucleus, the shear thinning liquid drop model, in which the liquid is modeled as a power law droplet, as well as the Maxwell liquid drop model.

The solid models treat the whole cell as a homogeneous body without considering the membrane itself. The cell material has been perceived as either incompressible elastic solid or viscoelastic solid. For a pure elastic solid, a constitutive equation defines:

$$\tau_{ij} = G\gamma_{ij} \tag{2.1}$$

in which G is the shear modulus and is related to the Young's modulus E by $E = 2(1+\nu)G$ with ν being the Poisson's ratio. For a live cell in liquid environment, the pure elastic solid model is inherently inadequate in describing the viscous behavior of cells. However, in most situations, the approximation would not cause any defect in describing the mechanical condition of the cell. Such practice has been constantly adopted by researchers with AFM nanoindentation measurement which provides the force-displacement curve.

The force curve plots the relation between the cantilever displacement (z) and its vertical deflection (d). A hard sample surface is regarded as indefinitely stiff compared with the cantilever and thus will not be indented at all. Therefore, the force curve has a slope of one, meaning the deflection equals the cantilever displacement. The deflection sensitivity which correlates the photodiode voltage with the deflection of the cantilever can be calibrated by this hard surface force curve. Moreover, it is a natural reference for soft surface force curves. The soft surface on which indentation becomes dominant will have a slope less than one. The difference between the two in

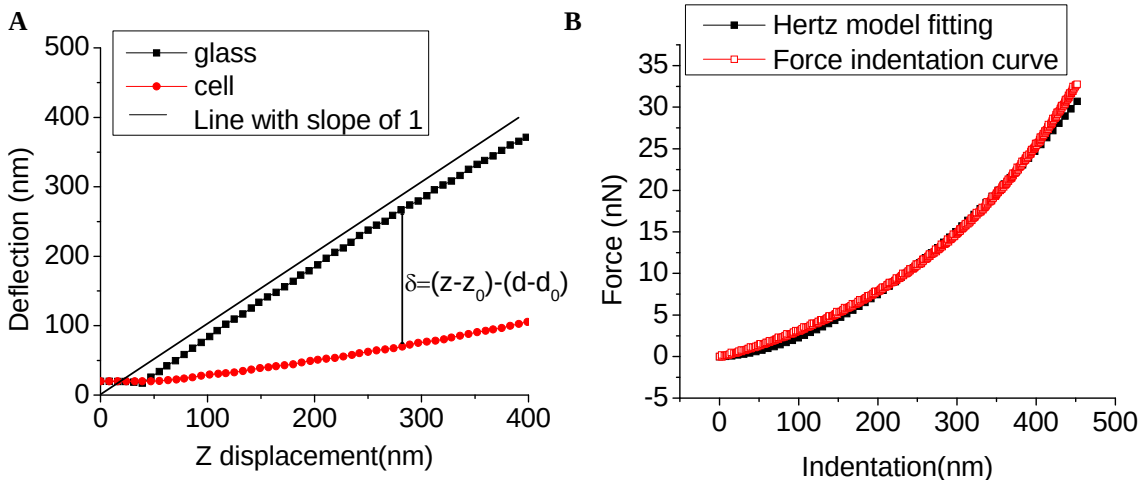

Figure 2.1 A: The conversion of force-displacement curve to force-indentation curve; B: The fitting of the force indentation curve by Hertz model to generate the Youngs modulus.

the deflection axis is the indentation depth δ.

$$\delta = z - d \tag{2.2}$$

The point from where the force curve slope starts is called the contact point, where the initial contact between the tip and the sample surface was established. Thus, the offset of both the displacement (z_0) and the deflection (d_0) before the contact point should be subtracted, as shown in Fig. 2.1A.

$$\delta = (z - z_0) - (d - d_0) \tag{2.3}$$

The indentation force can be easily calculated by applying Hooke's law to the cantilever, where k is the spring constant of the cantilever.

$$F = k(d - d_0) \tag{2.4}$$

Therefore, the force displacement is converted to the force indentation curve which directly

depicts the stiffness of the cell surface (Fig. 2.1A). The force indentation curve can be further fitted to the Hertzian model to generate the quantitative data on the Young's modulus (E) of the cell surface (Fig. 2.1B). For a conical tip the relationship between the applied force and the indentation can be expressed as:

$$F = \frac{2}{\pi tan(\alpha)} \frac{E}{1-\upsilon^2} \delta^2 \tag{2.5}$$

where α is the half opening angle of a conical shaped indenter and ε is the Poisson ratio.

A number of studies have used a spherical tip at the end of the cantilever instead of a conical shape for indentation measurement. The fabrication process involves gluing a spherical particle, normally polymeric and with 1 μm to 5 μm diameter, to one end of the cantilever. In this case, the relationship between the indentation and the applied load will be slightly different:

$$F = \frac{4}{3} \frac{E}{1-\upsilon^2} R^{\frac{1}{2}} \delta^{\frac{3}{2}} \tag{2.6}$$

where R is the radius of the sphere and the other quantities remain.

The main advantage of using a spherical AFM tip for nanoindentation is less damage to a soft sample compared with the sharp conical tip, normally 10 to 40 nm in diameter at the apex. The spherical tip can induce deformation of a large area; therefore, the global stiffness can be measured [89]. On the other hand, a sharp tip indents a much smaller area, and it resolves local stiffness very well. This is especially useful when the inhomogeneity of the biological samples matters most. With cells, for example, the underlying cytoskeleton that supports the soft membrane is not evenly distributed and organized. In this case, the dynamic distribution and organization of cytoskeleton may be best monitored by measuring the local stiffness using the conical tip. To identify the mechanical property of a cell population which is not homogenous, statistical analysis of a large number of cells must be undertaken.

Force modulation imaging is an AFM technique that maps differences in surface stiffness [90]. It is based on contact mode AFM imaging. The basic principle for force modulation is to add a small vertical oscillation of the tip during the contact scanning. That means the contact force is modulated while the average is still the same as in contact mode. When the tip is modulated with a vertical displacement around 10 nm with a frequency ranging from 0.5 Hz to 500 Hz [91], there will be a difference in the resistance of this oscillation among areas with different mechanical properties. This resistance can be measured as the viscoelasticity of the sample.

For a spherical shaped AFM tip, the applied normal force, a complex with different modulation frequency can be denoted as (derived from Eq. 2.5) [90]:

$$F^* = \frac{R^{\frac{1}{2}}}{1-\upsilon^2}(E_0\delta^{\frac{3}{2}} + \frac{3}{2}E_1^*\delta_0^{\frac{1}{2}}\delta_1^*) \tag{2.7}$$

where υ is the Poisson ratio, R is the radius of the probe and E_0 is the elastic modulus at zero frequency. E_1^* is the frequency-dependent elastic modulus. δ_1^* is the indentation displacement caused by the oscillation force, and δ_0 is the main indentation caused by the applied force by contact AFM.

Two components constitute the applied force: the contact force and the oscillation force. The original Hertz model force is the same as Eq. 2.6. And the oscillation force is:

$$F_{osc}^* = \frac{2R^{\frac{1}{2}}}{1-\upsilon^2}\frac{4}{3}E_1^*\delta_0^{\frac{1}{2}}\delta_1^* \tag{2.8}$$

The complex modulus can therefore be expressed as the relation between the applied complex

force and the indentation as well as the indentation displacement:

$$G^* = G' + iG'' = \frac{f^*_{osc}}{2\delta^*_1 (R\delta_0)^{\frac{1}{2}}} \tag{2.9}$$

From Eq. 2.9, we can calculate the elastic moduli of the viscoelastic biological samples with the real part G' as the storage modulus and the imaginary part G'' as loss modulus.

For viscoelastic model, the standard linear solid model has a configuration of a serial connection of spring and dashpot in parallel with a spring of different spring constant. The constitutive equation defines:

$$\tau_{ij} + \frac{\mu}{k_2}\dot{\tau}_{ij} = k_1\gamma_{ij} + \mu(1 + \frac{k_1}{k_2})\dot{\gamma}_{ij} \tag{2.10}$$

in which τ_{ij} is the stress component, and γ_{ij} is the strain component. k_1 and k_2 are the spring constants and μ is the viscous damping of the dashpot.

2.2.2.2 Structural models

One of the structural models that caused a large impact is the tensegrity model that was introduced by Ingber, which assigns the roles of three basic cytoskeletal elements [92](microtubule, actin filament, also called microfilament, and intermediate filament) play in the establishment of force balance of the cell structure based on the different intrinsic property of these cytoskeletal element. The microtubule is the stiffest of the three, and would bear the compressional force and the actin and intermediate filaments would bear the tensional force, thus the structure itself composed of these three type of elements would be able to balance itself with the help of anchoring point through cell adhesion [93](Shown in Fig. 2.2A). The change of structure, or so called reconfiguration of the cell would go through the dynamic biochemical processes: assembly and disassembly of these microtubule and filaments, crosslink of the filaments. Of these processes, one of the most important

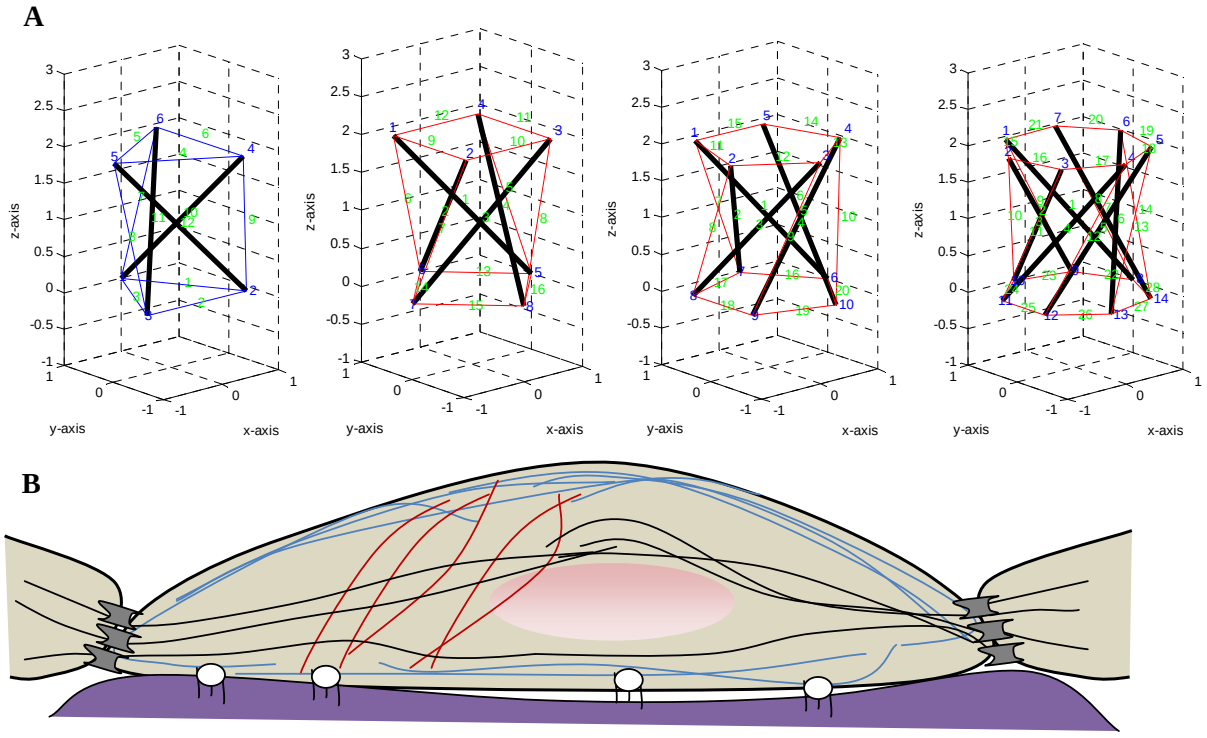

Figure 2.2 A: The cell structure is based on cytoskeleton tensegrity. B: Tensegrity structures.

is the regulation of the cell adhesions, since the cell adhesions are the de facto external support that cell use to balance itself [66].

2.2.3 Importance of cell adhesion in the establishment of cell mechanical states

Cell adhesion comprises two main categories: one is the cell-ECM adhesions, that's normally called the focal adhesions [92] as shown in Fig. 2.2B. It is a anchoring point of the cell to the ECM. It recruits a cluster of proteins to form the mechanical stabilization mechanism; in the mean time, it serves as the signaling harbor for the various downstream signaling pathways that regulate the fundamental cell development and fate: cell migration, inflammation response, apoptosis, and cancer metastasis [59]. Another type of cell adhesion is the cell-cell adhesion. They are mainly

cadherin based cell adhesions. The desmosome is one type of the cadherin based cell adhesion, which is divalent-cation-dependent, proteolytic enzyme such as trypsin as well as removal of extracellular Ca^{2+} and Mg^{2+} with a divalent cation chelator such as EDTA would cause dissociation of these adhesions [92].

2.2.4 Different model could apply at different scenarios

The fact that the cell structure and the dynamics are so complicated that no single model is detailed or suitable enough for all applications and cell related process. Thus you would see through out the whole study that different models have been utilized in order to parse the parameters of certain properties, or to extract certain properties. In these cases, different assumptions were made to facilitate the building of these models and to use these models for predictions. And also based on this fact, we can deduce that no single measurement of imaging modality would be enough to address these complicated and complex matters and related processes, thus you would also see the use of a combination of imaging modalities and measurement techniques in order to build a more complete profile of the cell dynamic responses during the extracellular stimulation process.

2.3 Manipulation and measurements at the molecular level

The identification and measurement of biomechanical information on live cells requires the use of micro/nano manipulation and measurement instruments. Among them, the most popular is the AFM as we introduced in the previous sections. The earliest measurement and manipulation often employs the micropipette aspiration technique [94], in which a suction pressure is applied to a static cell body until a hemispherical projection is formed inside the pipette. The relationship between the applied suction pressure and the property of the cell body, in this case modeled as a liquid drop

enclosed by a cortical shell can be derived. Similar techniques of this sort is the optical tweezers which also consider the cell as a shell-liquid model. Laser traps the microbeads which attached at two distal end of the cell would cause significant deformation, normally stretching of the cell [95]. Magnetic twisting cytometry [96] was used to assess the rheological properties of smooth muscle cells; a magnetic field of varying frequency was applied to the microbeads, initially magnetized in a predefined direction, that were trapped on the membrane of the cell. An angle of rotation would then be measured by a magnetic detector and used to interpret the complex modulus of the cell.

2.3.1 DNA manipulation

DNA molecules are mechanically flexible and physicochemically stable. The capability of AFM to maneuver objects at the molecular level has allowed the manipulation of DNA. Based on the behavior model of DNA, the operation can be displayed in real time in an augmented reality environment as studied by Li and coworkers [8].

2.3.2 Single cell manipulation

There are a number of different mechanisms for single cell manipulation, including micropipette aspiration, optical trapping, magnetic twisting, and nanoindentation, etc. Each technique works differently to fit different mechanical models for single cell structures. Regarding AFM based single cell manipulation, the main operation is AFM based nanoindentation. There are two different types of AFM based nanomanipulation: unpenetrated nanoindentation and penetrated nanoindentation.

For unpenetrated nanoindentation, the sharp AFM tip only deforms the membrane surface of the cell. Because the cell membrane is supported by and propagated through the cytoskeleton,

deformation at the surface can result in cytoskeletal re-configuration. Altered cytoskeleton organization results in an altered response to the applied load, and is eventually manifested in the form of changes in the overall stiffness of the cell body. There is also work to suggest that the tension in the cell membrane is mainly responsible for the stiffness behavior of the cell body, like a balloon filled with liquid [83]. However, recent findings indicate that the cell may behave more like a globally interconnected structure covered by a soft membrane, like a tent that is nailed to the ground [85]. This is also consistent with AFM imaging data where high applied contact force elevates the intracellular actin network.

For penetrated nanoindentation, the sharp AFM tip is used as a nanoneedle to penetrate the membrane and reach the actin filament network underneath. The applied force just before the penetration can be correlated with the indentation depth just before penetration. One important potential application of penetrated nanoindentation is for controlled drug delivery [97]. The nanoneedle can be fabricated with a hollow inner structure whereby certain drugs can be pumped into the cell upon penetration in a controlled fashion.

2.3.3 Filament manipulation and characterization

The cytoskeletal structure supports the cell, performs functions such as vesicle transportation and protein anchoring, and regulates the cell shape and movement. It composed of three different filament structures: actin filaments, intermediate filaments and microtubules. Each group of proteins is critical for cellular functioning. Dynein is a basic protein that is assembled together to make microtubules. It functions as a motor protein that converts chemical energy conserved in ATP to mechanical energy required for movement [92]. This process may provide a powerhouse for the development of future self-assembly fabrication processes to construct complex devices from nano building blocks.

Recently, mechanical properties of intermediate filaments have been studied [53]. For one study, intermediate filaments absorbed on the mica surface were stretched by AFM tip. The manipulation operation itself in this case was routine, but the findings from the experiment were striking. Intermediate filaments could be stretched more than two fold of original length. This in vitro experiment also confirmed the role of intermediate filament in the maintenance of mechanical integrity of the cell body and in providing strength for the entire tissue. These roles are performed particularly well when cells are undergoing a large extent of deformation, and can be systematically studied by this AFM nanomanipulation technique.

2.3.4 Nanodissection and nanosurgery

A very special group of operations using AFM involves nanodissection, or nanosurgery. The main purpose of this operation is to isolate, or partially isolate a group of cellular and/or molecular structures from other structures. There is literature on the dissection of DNA molecules, proteins, cell membranes, intermediate filaments, among other structures. Most of these experiments were performed for the sole purpose of demonstrating the capability of AFM based nanobiomanipulation systems in handling and changing biological matters. Our group has extended the application of nanosurgery to demonstrate that it can be a novel tool to re-create and disrupt specific functional biological activities with unparalleled precision.

2.4 Cellular nanosurgery mimics the effect of antibody treatment in cell-cell adhesion

The identification and measurement of biomechanical information on live cells require the use of micro/nano manipulation and measurement instruments. Among them, the most popular is the AFM as we introduced in the previous sections. The earliest measurement and manipulation often employs the micropipette aspiration technique [94], in which a suction pressure is applied to a static cell body until a hemispherical projection is formed inside the pipette. The relationship between the applied suction pressure and the property of the cell body, in this case modeled as a liquid drop enclosed by a cortical shell can be derived. Similar technique of this sort is the optical tweezers which also consider the cell as a shell-liquid model. Laser traps the microbeads which attached at two distal end of the cell would cause significant deformation, normally stretching of the cell [95]. Magnetic twisting cytometry [96] was used to assess the rheological properties of smooth muscle cells; a magnetic field of varying frequency was applied to the microbeads, initially magnetized in a predefined direction, that were trapped on the membrane of the cell. An angle of rotation would then be measured by a magnetic detector and used to interpret the complex modulus of the cell.

Chapter 3

In situ sensing of ion channel activities after glucose stimulation

3.1 Introduction

The molecular mechanism of insulin secretion from pancreatic β-cells in times of elevated glucose levels has been well documented over the past decade. Insulin is produced by β-cells to maintain glucose homeostasis. When the extracellular glucose level rises, glucose will be transported to the cytoplasm through the glucose transporter GLUT2 [98]. The intracellular glucose level rise will increase the pace of glucose metabolism resulting in increased ATP/ADP ratio inside the β-cell [99] followed by the closure of the ATP-sensitive K^+ channel (KATP) [100]. The closure of KATP channels causes the increase in plasma membrane (PM) potential [101] and cellular depolarization, a process leading to activation of voltage-dependent calcium channels (VDCC). Activation of VDCC allows Ca^{2+} to flow into the cytoplasm and gives rise to the intracellular Ca^{2+} levels ($[Ca^{2+}]_i$) [102]. In response to the elevated $[Ca^{2+}]_i$, insulin-containing vesicles will fuse with plasma membrane to release the insulin [103]. The whole process is referred to as the stimulation-secretion coupling, a biphasic process in nature. The initial 5-10 minutes with the rapid insulin exocytosis is referred to as the first phase [104], while the subsequent second phase is characterized by a sustained insulin exocytosis, an ATP-dependent process which releases insulin-containing vesicles in reserve pools further away from the releasing site [105].

Capsaicin, the pungent component of chili peppers, is a specific agonist of the transient receptor potential vanilloid type 1 (TRPV1) channel or the vanilloid receptor [106]. TRPV1 receptor protein is expressed in nerve fibers innervating the pancreatic islets of rats and mice [107]. It has also been reported that TRPV1 expression is detected in rat insulinoma cell lines, RIN and INS-1 [108, 109]. Capsaicin may modulate insulin secretion through activation of capsaicin-sensitive afferent nerves [110]. Additionally, capsaicin may stimulate islet β-cells by binding to the intracellular domain of TRPV1 and thereby activating TRPV1 channels [111, 112] as illustrated in Fig. 3.1A. Thus the regulatory role of capsaicin on insulin secretion may be direct or indirect, a complex effect which remains to be defined. In comparison with glucose stimulation, capsaicin stimulated insulin secretion from islet β-cells is reported to be a sustained process [109] without the biphasic characteristics.

With the unique capability of AFM based nanorobotic manipulator (Fig. 3.1B), the current study went a step further and combines optical microscopy and AFM to unravel the ion channel dynamics in insulin release upon glucose and capsaicin stimulation. The ion channel activity was monitored by capturing fluorescence images of intracellular Ca^{2+} levels upon stimulation. Simultaneously, cellular stiffness was measured in real time with AFM nanoindentation to reveal the reorganization of the cell membrane and cytoskeleton resulting from ion channel reconfiguration.

3.2 Materials and methods

The insulinoma β-cell line RINm5f cells (ATCC, Manassas, VA) were cultured in RPMI-1640 medium (Invitrogen, Carlsbad, CA) supplemented with 10% fetal calf serum and 1% penicillin and streptomycin (Invitrogen, Carlsbad, CA) at 37°C in a humidified atmosphere containing 5% CO_2. The RINm5f cells used were between passages 20 and 30.

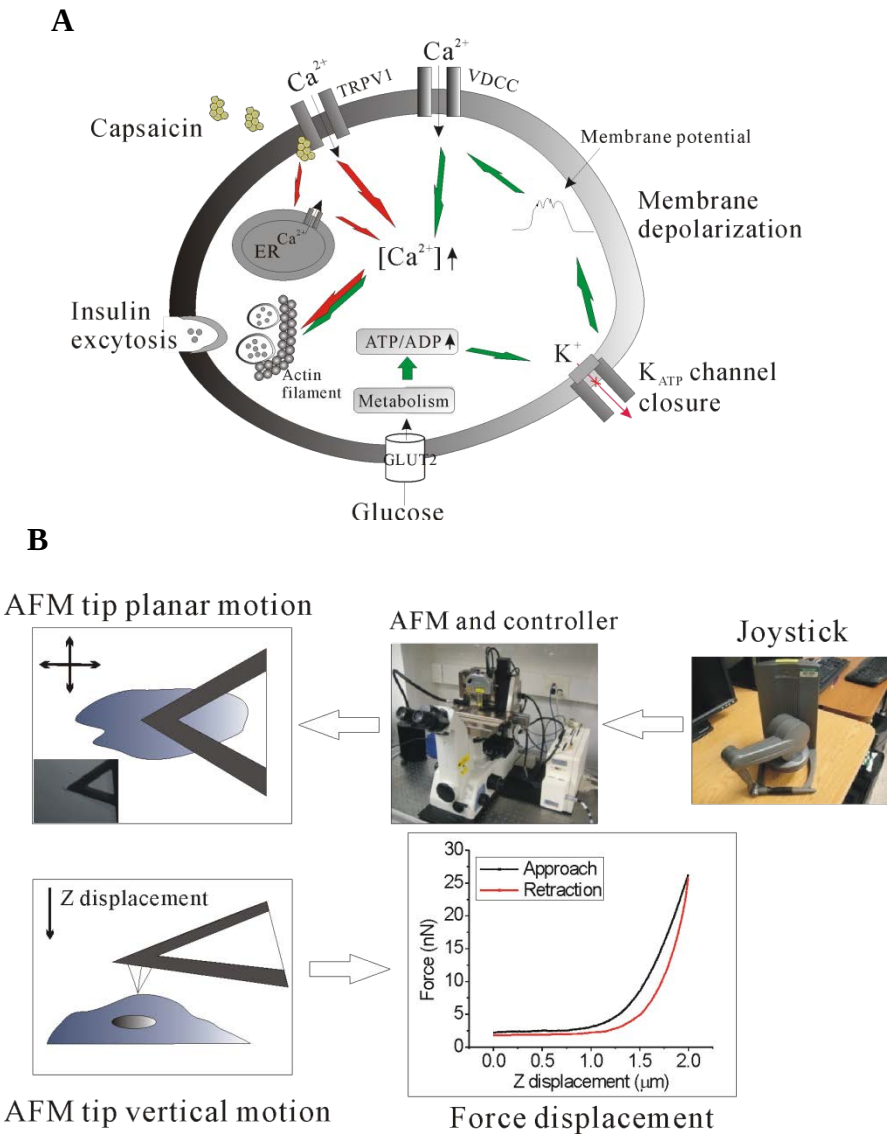

Figure 3.1 A: The stimulus-secretion coupling model of β-cells. Increased plasma glucose levels will increase the intracellular ATP/ADP ratio after glucose being uptaked by cells, which leads to the closure of ATP-dependent potassium channels, membrane depolarization, and the increase in intracellular Ca^{2+} concentrations through the activation of voltage dependent calcium channels (VDCC) and ultimately insulin secretion. Capsaicin binds to the intracellular domain of the TRPV1 receptor and causes the influx of Ca^{2+}, which triggers the release of Ca^{2+} into the cytoplasm from the endoplasmic reticulum (ER) and increases $[Ca^{2+}]_i$ concentrations. B: The AFM based nanorobotic manipulator uses a joystick as position input to facilitate the movement of the AFM tip in the planar area during the force measurement process.

3.2.1 TRPV1 immunofluorescence

For immunoreaction, RINm5f cells were seeded on glass-bottom petri dishes (MatTek Co., Ashland, MA) coated with poly-L-ornithine and incubated under standard conditions until they were 90% confluent. Cultured cells were then processed for immunofluorescence. After three washes with phosphate buffered saline (PBS), cells were fixed by incubation in 4% (v/v) paraformaldehyde in PBS for 15 min at room temperature, rinsed with PBS and incubated overnight at room temperature with anti-TRPV1 antibody, goat polyclonal IgG diluted 1:250 with 1% (w/v) bovine serum albumin (BSA) in PBS (Santa Cruz Biotechnology, Santa Cruz, CA). Control samples were incubated with 1% BSA in PBS. After three washes in PBS, fluorescence was revealed by incubation for 2 h in AlexaFluor488 labeled secondary antibody, donkey anti-goat IgG diluted 1:100 (Invitrogen, Carlsbad, CA) in PBS. Imaging of immunofluorescence was performed with an epifluorescence microscope equipped with the Nikon B-2A filter (excitation wavelength 450-490 nm). Images were acquired using a digital camera (Photometrics, Tucson, AZ) connected to the microscope and image was captured using software QCapture Pro 6.0.

3.2.2 Loading of Fur-2 AM to RINm5f cells

Fura-2 AM (Invitrogen, Carlsbad, CA) was diluted in the low glucose base medium (2 mM glucose + 1mM $CaCl_2$+140 mM NaCl + 2.8 mM KCl + 2mM $MgCl_2$ + 10 mM Hepes-NaOH) to a final concentration of 0.5 μ M. The RINm5f cells were rinsed with PBS three times. One ml of diluted Fura-2 AM ester solution was added to the dish and incubated for 30 minutes at 37°C. The cells were then washed with PBS three times and then incubated in the low glucose base medium for additional 30 minutes to allow complete de-esterification of intracellular AM esters.

3.2.3 Glucose and capsaicin stimulation and dosage-dependent study

All the experiments were performed at room temperature. Before each glucose stimulation experiment, the cells in the glass-bottom petri dishes loaded with Fura-2 AM were incubated with 5 ml of low glucose base medium (2 mM glucose, 1mM $CaCl_2$+140 mM NaCl + 2.8 mM KCl + 2mM $MgCl_2$ + 10 mM Hepes-NaOH) for additional 30 minutes until equilibrium. For glucose stimulation, a volume of 40 μl of high glucose medium (2M) was added into the dish to make the final glucose concentrations at 16 mM; a 40 μl of low glucose base medium was added to the control plates. Similar with glucose stimulation, the cells in the glass-bottom petri dishes loaded with Ca2+ binding agents were incubated with 5 ml of low glucose base medium for additional 30 minutes until equilibrium before capsaicin was applied. One ml of low glucose base medium with capsaicin (Sigma-Aldrich, St. Louis, MO) concentrations of 100 nM was added to the dish to obtain the final concentrations of 16.7 nM; One ml of low glucose base medium was added to the control plates.

Dosage-dependent experiments for glucose and capsaicin stimulation were carried out in the similar method described above. Dosages of 40 mM, 20 mM and 16 mM for glucose and 1.67 nM, 16.7 nM, 167 nM and 1.67 μM for capsaicin were examined with AFM analysis. One ml of low glucose based medium was used as control. For glucose stimulation, the stiffness calculated from the first 20 force curves before switching to high glucose were averaged as the baseline. The moduli from the first 20 minutes of measurements after addition of high glucose medium were averaged as the positive results. For capsaicin, 100 cells were randomly selected before the stimulation for base line measurement and another 100 cells 20 minutes after the stimulation on the same cell population, stiffness was measured and compared statistically. To test the specificity of capsaicin stimulation, the TRPV1 was blocked with 1.0 μM capsazepine (Capz) 30 minutes prior

to the capsaicin stimulation. Each data represents a minimum of three independent experiments.

3.2.4 Simultaneous fluorescence imaging of $[Ca^{2+}]_i$ and AFM measurements on RINm5f cells

Before adding glucose or capsaicin, 10 force displacement curves were taken as the baseline on the center of the same cell. After stimulation, force displacement curves were taken at a frequency of 1 Hz to dynamically monitor the stiffness change in real time for an hour. To obtain higher sensitivity and to prevent potential damage of the sharp AFM tip to the delicate cell membrane, force applied to indent the cell was kept minimal. The maximum force applied is controlled at below 10 nN with the resulted deformation less than 100 nm, and all the force curves are taken at a loading rate of 1 Hz, corresponding to a tip velocity of 5.98 μm/s. At the same time, the cells loaded with Fura-2 AM was observed under the inverted microscope with excitation wavelength 340-380 nm (UV-2E/C Nikon filter). Images were captured in a similar fashion as in the immunofluorescence for TRPV1 except at a much shorter exposure time (0.3 sec). The time-lapse images taken at 1 frame/s were then processed with ImageJ software (NIH) to obtain the mean gray scale values. The images were displayed in 8 bit gray scale (0-255) and each cell in each image was outlined and from which the gray scale value was obtained, averaged and normalized. Each data represents a minimum of three independent experiments.

3.2.5 Actin filament staining and imaging

Cells grown on glass coverslips were allowed to pre-incubate in 1 mL of the PBS at 37 C for 1 h. After pre-incubation, the buffer was removed and replaced with either 16 mM of glucose or 16.7 nM of capsaicin; the low glucose base medium was used for the control samples. After

various reaction times (0 min, 1 min, 5 min and 10 min) at 37°C, cells on glass coverslips were fixed/permeabilized in a solution containing 0.1% Triton X-100 and 3% paraformaldehyde in PBS buffer for 20 min. They were then washed three times by PBS buffer with 1% BSA. The resulting cells were stained with CF488A phalloidin conjugate (Biotium, Inc., Hayward, CA) in PBS with 1% BSA at room temperature for 20 min. Then the excess phalliodin solution was removed by rinsing with 1% BSA in PBS. Coverslips with stained cells were imaged with an inverted fluorescence microscope (Photometrics, Tucson, AZ). Images were processed with the use of QCapture Pro 6.0 software.

3.3 Results

3.3.1 Immunofluorescence of TRPV1 on RINm5F cells

Immunofluorescence staining of RINm5f cells with antibody selective for TRPV1 receptors revealed the positive fluorescence signals, primarily distributed peripherally of the cells (Fig. 3.2A), consistent with the notion that TRPV1 receptors are localized in the cell membrane of RINm5f cells [109]. The control samples incubated with 1% BSA in PBS show negative immunoreactivity (Fig. 3.2B). The result confirms that RINm5f cells express TRPV1 receptors on their cell membrane.

3.3.2 AFM stiffness observation of dosage responses to glucose and capsaicin stimulation

The normal Young's modulus value for insulinoma RINm5f cells in the low glucose medium was around 7.0 kPa, a similar value as previous reports by AFM based studies [113]. High glucose

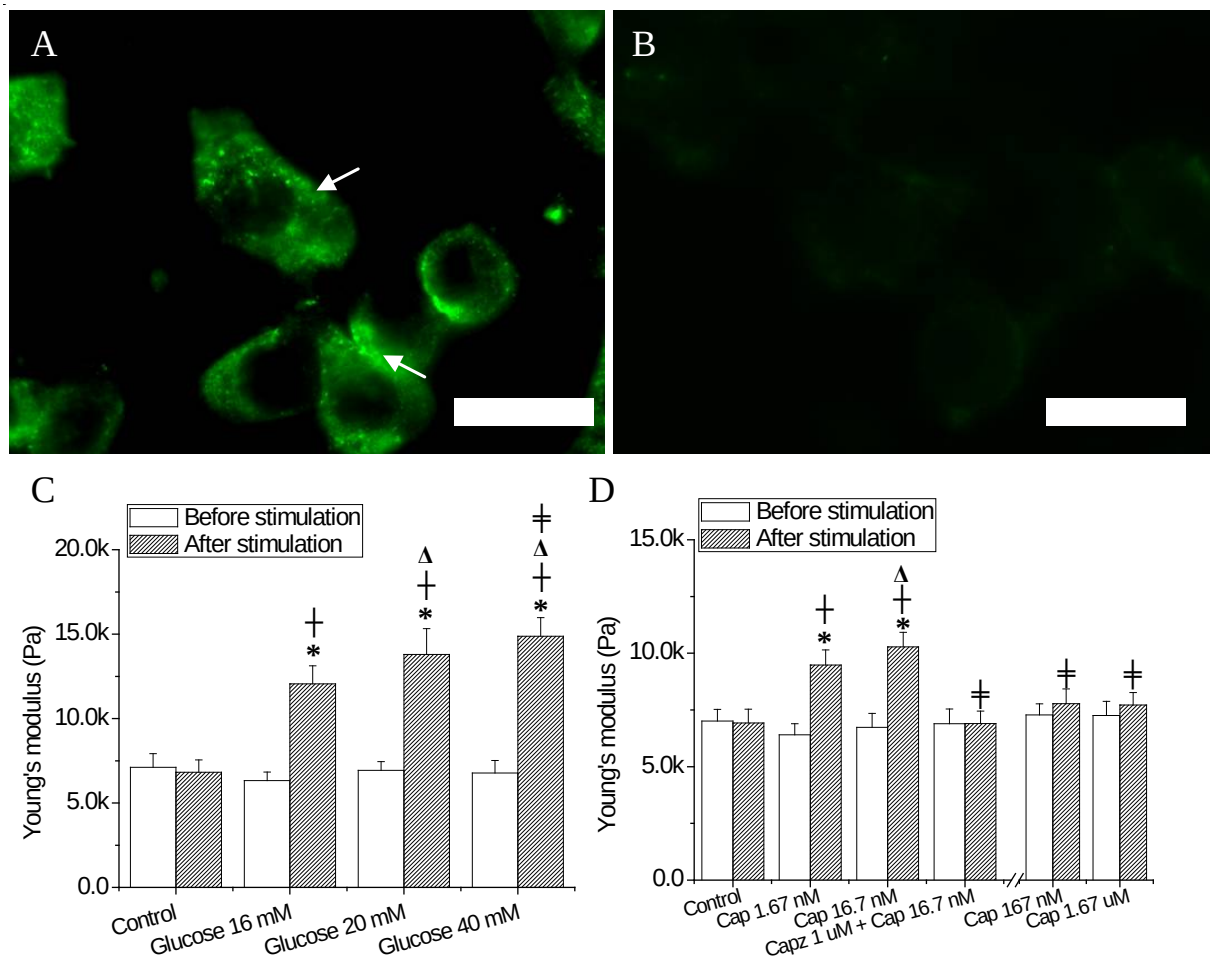

Figure 3.2 Immunofluorescence imaging of TRPV1 receptors in RINm5f insulinoma cells. A: Cell plasma membrane localization of TRPV1 receptors in RINm5f cells, positive staining indicated by arrows. B: Control RINm5f cells in which primary antibody was replaced with 1% BSA in PBS show negative staining. Scale bar: 20 μ m. C: The stiffness changes before and after administration of glucose at three concentrations, 16 mM, 20 mM, and 40 mM, plus the control. * $p<0.05$ vs. before stimulation; $p<0.05$ vs. control; $p<0.05$ vs. glucose 16 mM; $p<0.05$ vs. glucose 16 mM and 20 mM (n=20). D: The stiffness changes before and after administration of Cap (capsaicin) at four concentrations (1.67 nM, 16.7 nM, 167 nM and 1.67 μM), with *$p<0.05$ vs. before stimulation; $p<0.05$ vs. control; $p<0.05$ vs. Cap 1.67 nM; $p<0.05$ vs. Cap 1.67 nM and 16.7 nM. Each datum is expressed as mean SEM (n=100).

increased the stiffness, and the increase displayed a dose-dependent pattern (Fig. 3.2C). The modulus increase for 40 mM glucose stimulation was more than one fold, reaching 14.8 kPa. Stiffness increased to 13.8 kPa and 12.0 kPa for 20 mM and 16 mM, respectively. The control experiment with an equal volume of low glucose medium showed no significant changes in stiffness. Thus cellular stiffness in response to various doses of glucose stimulation is dose-dependent. The dose studies for capsaicin stimulation showed a different pattern compared with glucose. Statistical analysis showed that stiffness increased for lower concentrations of capsaicin at 1.67 nM and 16.7 nM but not at higher concentrations of 167 nM and 1.67 μM (Fig. 3.2D). These data support the finding [114] that the high dose of capsaicin had insignificant effects on insulin secretion, possibly due to desensitization of TRPV1 induced by high concentrations of capsaicin [113]. The control samples and the samples treated with Capz, an antagonist of TRPV1, showed no significant change of mechanical property (Fig. 3.2D). Taken together, these results indicate that increases in cell stiffness are linked to insulin secretion, and the nanomechanical properties may well serve as biomarkers for insulin secretion.

3.3.3 $[Ca^{2+}]_i$ and stiffness observation of glucose stimulation

To look at the activities of ion channel and cellular mechanical property under stimulation, real time observation was performed on a single RINm5f cell. The normal Young's modulus value for the individual RINm5f cell was around 7.0 kPa for the 10 minutes baseline measurement before the addition of high glucose medium to make the final glucose concentration 16 mM in the dish. Immediately following the glucose stimulation at 16 mM, altered ion channel activity was indicated by the sharp increase by about 20% in light intensity of $[Ca^{2+}]_i$ imaging (shown in Fig. 3.3A). The light intensity remained at a relatively higher level for 3-4 minutes before it dropped to the baseline. It is worth mentioning that the initial slight drop of light intensity was probably due

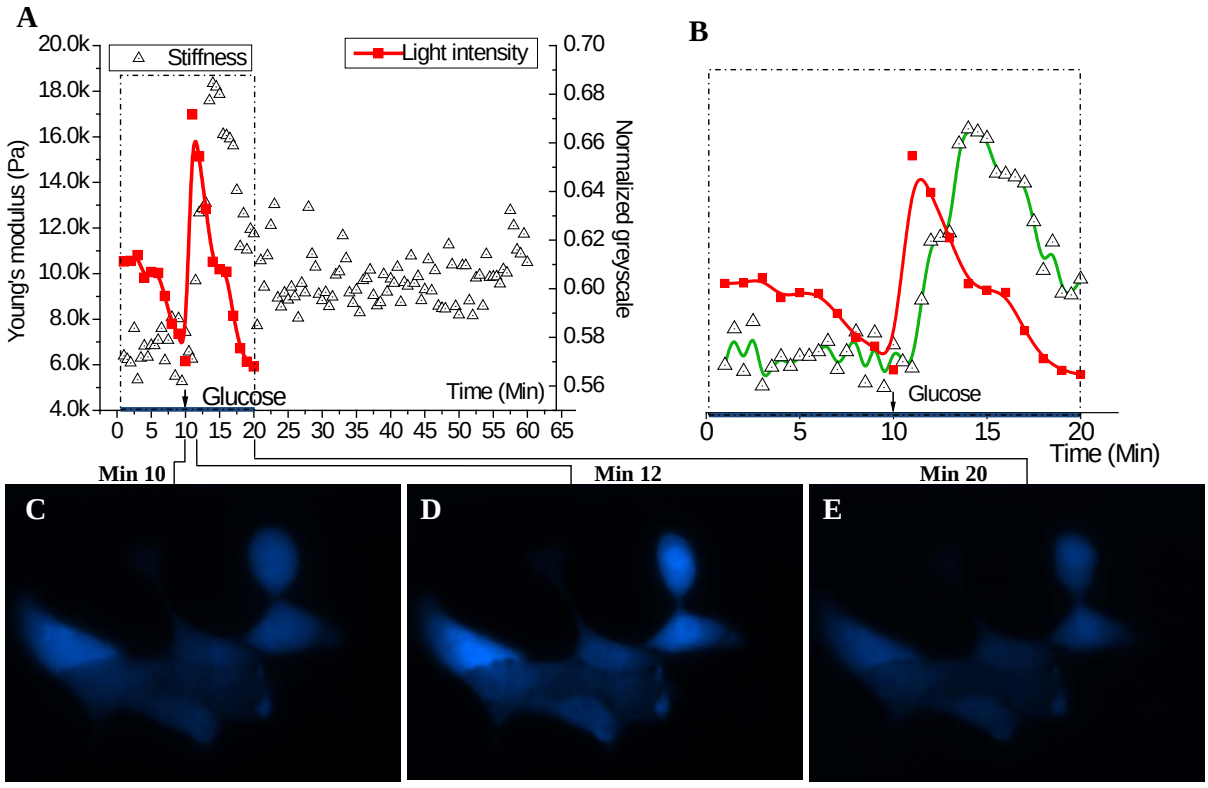

Figure 3.3 Dynamic characterization of cellular stiffness simultaneously with $[Ca_{2+}]_i$ fluorescence imaging after glucose (16 mM) stimulation. A: The ion channel activities overlaps with the overall cellular stiffness change in the first phase when the onset of stimulation induced rapid structural rearrangement. A second sustained phase follows to maintain the structural configuration and stiffness at a relatively higher level than the baseline. B: A close-look at the lagging of stiffness response compared with that of intracellular Ca^{2+} concentrations, a 2 minute-delay was observed. C, D, E: The fluorescence imaging of $[Ca^{2+}]_i$ before stimulation (C), 12 minutes after stimulation when the light intensity reaches the peak (D), and 20 minutes after stimulation (E) when the light intensity falls to the baseline.

to the photo-bleaching effect, and for the same reason, the imaging capture stopped at minute 20 when the light intensity was bleached to the level below the baseline. The fluorescence images of RINm5f cells at minute 10 (before stimulation), 12 (plateau was reached) and 20 (returns to baseline) were shown in Figs. 3.3C, D and E. At the same time, the cellular stiffness increased sharply as well, and it took about 5 minutes for the stiffness to reach a plateau at around 18.0 kPa. This was followed by a rapid decline at a similar rate as the climbing. About 10 minutes post stimulation, the stiffness dropped to a value around 10.5 kPa, about 1.5 times the baseline value and leveled off through the rest of the observation. Note that in Fig. 3B, a close up look of the stiffness and light intensity measurement 10 minutes prior and 10 minute post stimulation showed a 2-minute lagging of mechanical property changes when compared with the ion channel activities. The nanomechanical analysis results were echoed by the changes of cytoskeleton structures. The staining of actin showed a disorganized filament structure one minute after glucose stimulation while the control displayed no visible changes shown in Fig. 3.6.

3.3.4 $[Ca^{2+}]_i$ and stiffness observation of capsaicin stimulation

Upon capsaicin stimulation at 16.7 nM, the light intensity increased immediately (Fig. 3.4A). Lack of altered light intensity was observed for samples treated with Capz 30 minutes prior to capsaicin stimulation (Fig. 3.4B). A pulse-like response lasted approximately 3-5 minutes before it dropped to the baseline. The images corresponding to minute 10, 12 and 20 were shown in Fig. 3.4C, D and E. The Ca^{2+} influx response after capsaicin treatment experienced a similar pattern as that of glucose. The baseline value of stiffness for the cell population under capsaicin stimulation is similar to the one in glucose experiment. However, no rapid increase of stiffness was observed following the administration of capsaicin. Instead, the stiffness increased gradually, reached the peak at approximately 11.0 kPa about 20 minutes after the stimulation. This sustained stiffness response

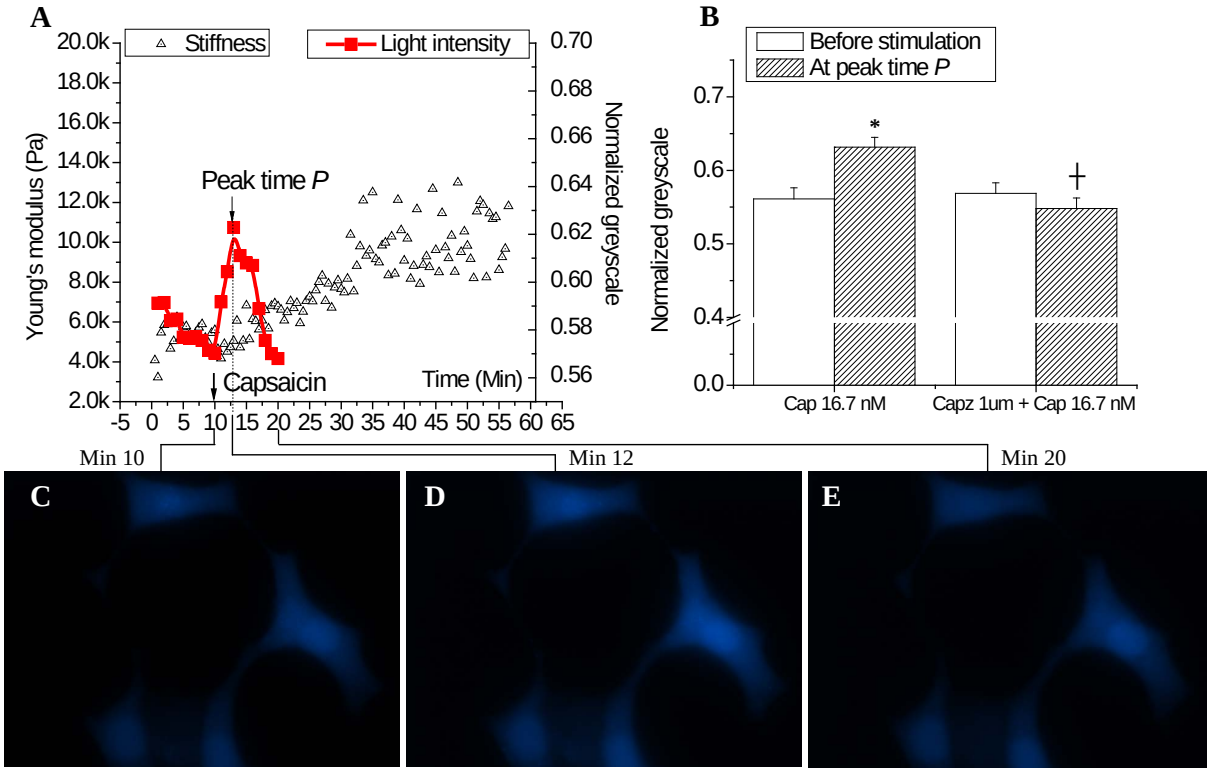

Figure 3.4 Dynamic characterization of cellular stiffness simultaneously with $[Ca^{2+}]_i$ fluorescence imaging after capsaicin (16.7 nM) stimulation. A: The ion channel shows similar pulse-shape response pattern as that of glucose albeit with smaller peak value. B: The cells were also pretreated with Capz 30 minutes before capsaicin stimulation to block TRPV1 receptors. No increase in light intensity was observed for TRPV1-blockade samples shown in the normalized gray scale before and after capsaicin stimulation. *$p<0.05$ vs. before stimulation; $p<0.05$ vs. Cap 16.7 nM. C, D, E: The fluorescence imaging of $[Ca^{2+}]_i$ before (C), 12 minutes after stimulation (D) when the light intensity reaches the plateau, and 20 minutes after stimulation (E) when the light intensity falls to the base line. The normalized gray scale value was obtained the same way as the Fig. 3.3.

stopped after the plateau was reached and remained at that value for the rest of the observation. Similar change of actin filament structures was observed but with a distinctive temporal pattern; the structural disorganization didn't start to surface until after 10 minutes of capsaicin stimulation as shown in Fig. 3.6.

3.4 Discussion

It is well documented that increased glucose concentration in the extracellular environment would lead to increases in plasma membrane potential, elevated $[Ca^{2+}]_i$ and ultimately insulin secretion, a process commonly referred to as stimulus-secretion coupling [115–117]. Studies have also shown that capsaicin is an effective compound stimulating insulin secretion from insulinoma β-cells including RINm5f and INS-1 cells [109, 114]. Although glucose and capsaicin have been shown to induce distinctive patterns of insulin release, i.e., a biphasic secretion response upon glucose but not capsaicin stimulation [118, 119], the biophysical characteristics of cells in response to these stimuli have not been well defined. The present study aimed to study the temporal relation of ion channel activity, cell membrane biophysical dynamics, and cytoskeleton reorganization of β-cells in real time with AFM nanoindentation to reveal potential mechanisms underlying distinct insulin-secretion processes in response to glucose and capsaicin.

The results from the present study using AFM based nanomechanical analysis show for the first time that the β-cells biomechanically respond to glucose stimulation in a biphasic manner, consistent with the pattern of insulin release. The cellular stiffness increases rapidly and then decreases sharply within 10 minutes of glucose stimulation, followed by a sustained second phase to maintain the cellular stiffness at a relative higher level than the baseline. The biphasic pattern of cell stiffness in response to glucose stimulation is distinct from that induced by capsaicin (fitted curve

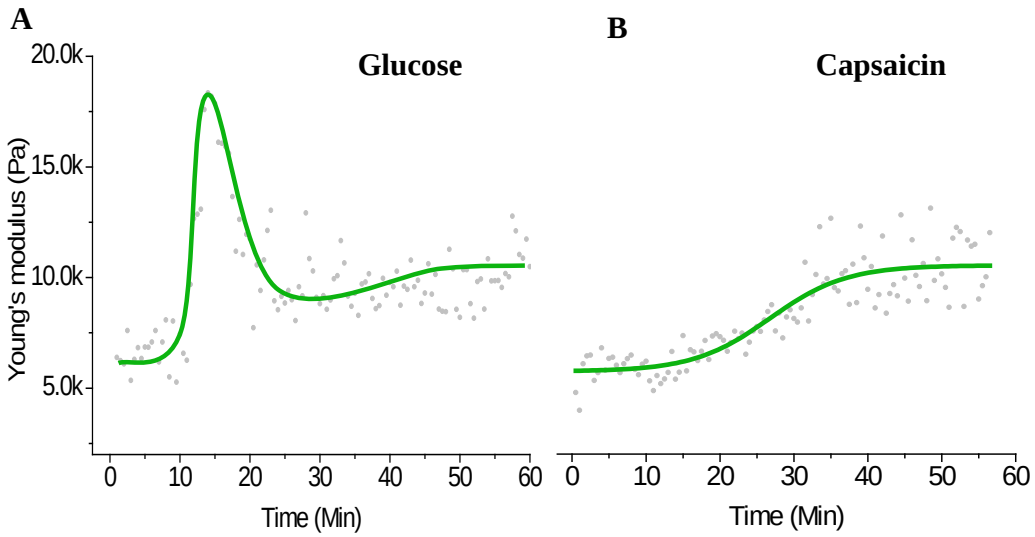

Figure 3.5 The overall trend of the stiffness responses. A: Glucose stimulation resulted in a two-phase response: a rapid increase phase in stiffness followed by a sustained elevation phase; B: Capsaicin stimulation induced a slow and sustained increase in stiffness.

showing the overall trend in Fig. 3.5). Capsaicin induces a sustained and slow increase of cellular stiffness without a rapid increase or decrease pattern, a change consistent with that of insulin secretion in response to capsaicin. Although it is known that biophysical changes may result from reorganization of cytoskeleton structure to facilitate the transport and fusion of insulin-containing vesicles with the plasma membrane [80, 118, 119], the nature of fine changes in cellular structure and mechanical property presents a daunting challenge for the detection and measurement techniques. The present study shows that biophysical markers captured by AFM based nanomechanical analysis may be used as indicators for altered ion channel activities and thereby insulin secretion.

The initial phase of sharp increases in stiffness in response to glucose stimulation overlaps temporally with altered ion channel activities that result in elevated intracellular Ca^{2+} concentrations, with a few minutes of delay in stiffness to reach the peak. These results indicate that structural changes in the cell membrane or cytoskeleton follow the rapid responses of ion channels activated by stimuli. In contrast, the increases in stiffness in response to capsaicin stimulation do not coincide temporally with increased intracellular Ca^{2+} concentrations, with a long delay in stiffness to

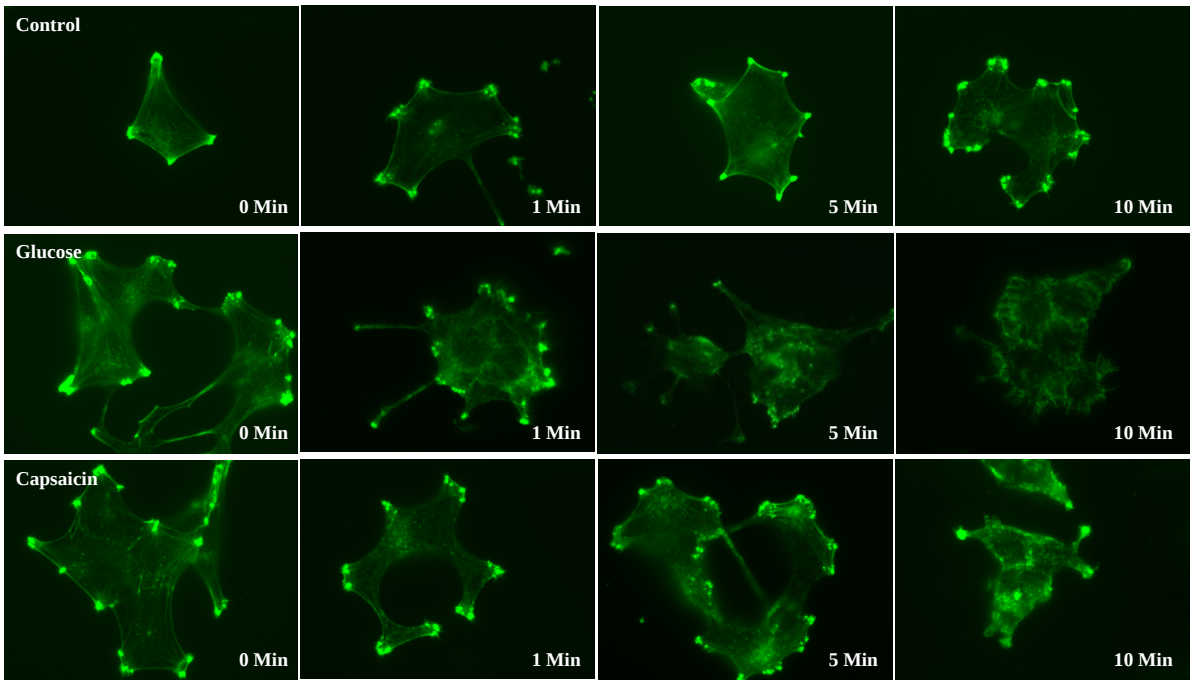

Figure 3.6 The actin filament reorganization after treatment of low glucose based medium as control, 16 mM glucose and 16.7 nM capsaicin for 0 min, 1 min, 5 min and 10 min. F-actin was labeled with CF488A-conjugated phalloidin. The treatment of glucose and capsaicin causes time-lapse change of cytoskeleton especially actin filament structures with distinct patterns. A delayed disorganization of actin around 10 minutes after stimulation was observed in capsaicin treatment, whereas glucose triggered the disorganization 1 minute after treatment, similar with the biophysical data obtained by AFM nanomechanical analysis. No distinctive change was observed for the control sample.

reach the peak. These results indicate that structural changes in the cell membrane or cytoskeleton in response to TRPV1 activation induced by capsaicin or to glucose are dissimilar and agonist-specific albeit the changes in $[Ca^{2+}]_i$ concentrations showed similar pulse-response patterns for capsaicin and glucose. The results of immunocytochemistry study of actin filament concur with the biophysical measurements obtained with AFM examination. As seem in Fig. 3.6, the treatment of glucose and capsaicin causes time-lapse changes of cytoskeleton especially actin filament structures with distinct patterns. A delayed disorganization of actin around 10 minutes after stimulation was observed in capsaicin treatment, whereas glucose triggered the disorganization 1 minute after treatment, similarly with the biophysical data obtained by AFM nanomechanical analysis.

The biphasic model of insulin secretion from pancreatic β-cells is well established and can be elicited by several compounds including glucose, arginine, and protein kinase C activators [120, 121]; under certain conditions, the first phase of insulin secretion may appear alone, without the second phase [120]. Until recently, there was no compound or treatment condition that elicited the second phase only. Our data shows that the initial calcium influx induced by glucose or capsaicin is similar with a sharp increase in $[Ca^{2+}]_i$, but it diverges hereafter. While a signaling cascade situated between altered $[Ca^{2+}]_i$ and insulin secretion induced by capsaicin has yet to be fully elucidated, our data from cell stiffness changes and actin reorganization support the notion that capsaicin causes only a delayed-phase insulin secretion. It has been indicated that the delayed phase of insulin secretion involves the Rho family of kinases that interacts with and causes the re-arrangement of actin cytoskeleton in β-cells [118]. Interestingly, TRPV1 activation with capsaicin may trigger the Rho kinase pathway [121]albeit this has yet to be shown in pancreatic β-cells. Taken together, our data show that in contrast to well described glucose-stimulated dual phase secretion of insulin, capsaicin causes a delayed phase of insulin secretion through TRPV1 activation resulting in actin reorganization and cell stiffness changes.

The islet β-cell insulin secretion process is highly regulated by electrical and ion channel activities [122]. The electrophysiological properties of ion channels play a crucial role in the secretion process, the defect of which may lead to metabolic disorders [123]. These ion channel properties have been investigated to elucidate the underlying secretion mechanism through membrane capacitance measurements. Patch-clamp technique has been employed to measure the capacitance increase resulting from the membrane expansion due to insulin exocytosis [124]. While effective, patch-clamp studies are normally time consuming and demand highly skilled workers. More importantly, electrically-regulated insulin secretion is coupled with biophysical changes of the membrane [119], and the electromechanical coupling can be revealed fully by integrated studies

of electrical activity and biophysical monitoring [125].

3.5 Chapter summary

In this chapter, we have successfully established a biomechanical marker during the stimulated ion channel responses. All the evidence indicates that islet β-cells exhibit a different physical state during the insulin secretion process, on which the biophysically biphasic glucose stimulation and single-phased capsaicin stimulation depend. These biophysical features may be addressed by identifying and characterizing signatures of ion channel activities. Many have reported that β-cells showed similar patterns of Ca^{2+} levels and insulin release in vitro and in vivo in responses to glucose stimulation [126, 127]. Taking into consideration the fact that islet cells tend to cluster in vivo [126], changes in biophysical property are expected with three dimensional environments as compared with a cell monolayer. A continued study with cell encapsulation would be better positioned to address these speculations. The current study aimed to develop and apply novel techniques such as this AFM nanorobotic system to examine physical properties of pancreatic insulin secreting cells by characterizing nanomechanical properties of a single cell or a cell population so that unique biomarker(s) in response to general or specific channel activators may be identified. Among many biophysical characterization techniques used for living cells, AFM stands out for a better fit for the task. In recent years, AFM has become an increasingly versatile tool in studies of biological processes for in situ nanoscale measurements [14]. With the use of the AFM nanoindentation, nano- even pico- Newton forces may be applied for the biophysics dynamic measurement, rendering the capture of tiny changes of cellular structure and property possible. The integrated approach with AFM and optical microscopy, aimed at unraveling the dynamic responses to ion channel stimulation, may provide a new perspective in the study of pancreatic β-cell stimulation.

Chapter 4

In situ biomarker detection during signaling events

4.1 Introduction

Desmosomal junctions are specialized structures critical to cellular adhesion within epithelial tissues. Disassembly of these junctions (acantholysis) can occur following autoimmune attack. Pemphigus vulgaris (PV) is a prototypical organ-specific human autoimmune disease characterized clinically by flaccid blister formation in the skin and mucous membranes that can be life-threatening. Histologically, there is an intraepidermal split resulting from acantholysis of suprabasilar keratinocytes that occurs in the presence of autoantibodies to specific desmosomal proteins, primarily desmoglein 3 (Dsg3) [128]. Anti-Dsg3 autoantibodies have been shown to induce acantholysis in cultured keratinocytes [129] and blister formation in vivo in neonatal mice [130]. Splenocytes from Dsg3-/- mice adoptively transferred into Rag2-/- recipient mice (that express Dsg3) produce anti-Dsg3 antibodies that lead to the development of suprabasilar acantholysis in the oral mucosa and esophagus [130].

Although lesion development in patients with PV is generally associated with high titers of anti-Dsg3 autoantibodies, the precise molecular mechanisms by which autoantibodies direct the loss of cell-cell adhesion is not known. In particular, it is unclear if acantholysis is the direct result of structural changes at the keratinocyte cell surface that occur subsequent to autoantibody binding

and/or is dependent upon functional changes within the cell. Moreover, there is now clear evidence that PV patients harbor both anti-Dsg3 antibodies that lead to blister formation (pathogenic) and anti-Dsg3 antibodies that do not lead to blister formation (nonpathogenic) [129, 131]. While both pathogenic and nonpathogenic autoantibodies are capable of binding to Dsg3 molecules expressed within desmosomal bodies at the keratinocyte surface, it is not known why they lead to different clinico-pathological outcomes.

To address these outstanding questions, novel experimental technologies and strategies are required. To date, it has been extremely challenging to study the morphology of cell junctions by standard light microscopy in living cells because of their small size (< 1 μm) and complex structure [132, 133]. While electron microscopy has provided insight into the fine structure of cell adhesion molecules [134], a model system for addressing dynamic changes due to (patho-) physiological mechanisms has been lacking.

We utilized established, as well as novel roboticized AFM methods to visualize desmosomes in physiologic and disease conditions at the nanoscale, and determine detailed nano-structural correlates of the acantholythic process not previously attainable. Furthermore, we have linked AFM data to functional alterations in cell behavior to develop a new paradigm for autoantibody mediated tissue destruction in the skin. We reveal for the first time that pathogenic anti-Dsg 3 antibody attack is associated with changes in cellular stiffness that are distinct from the changes induced by non-pathogenic antibody. Both pathogenic and non-pathogenic autoantibodies induce an early, but incomplete, disruption of intercellular adhesion (“hit 1”), but pathogenic antibodies alone lead to a later induction of apoptosis-related signaling (“hit 2”).

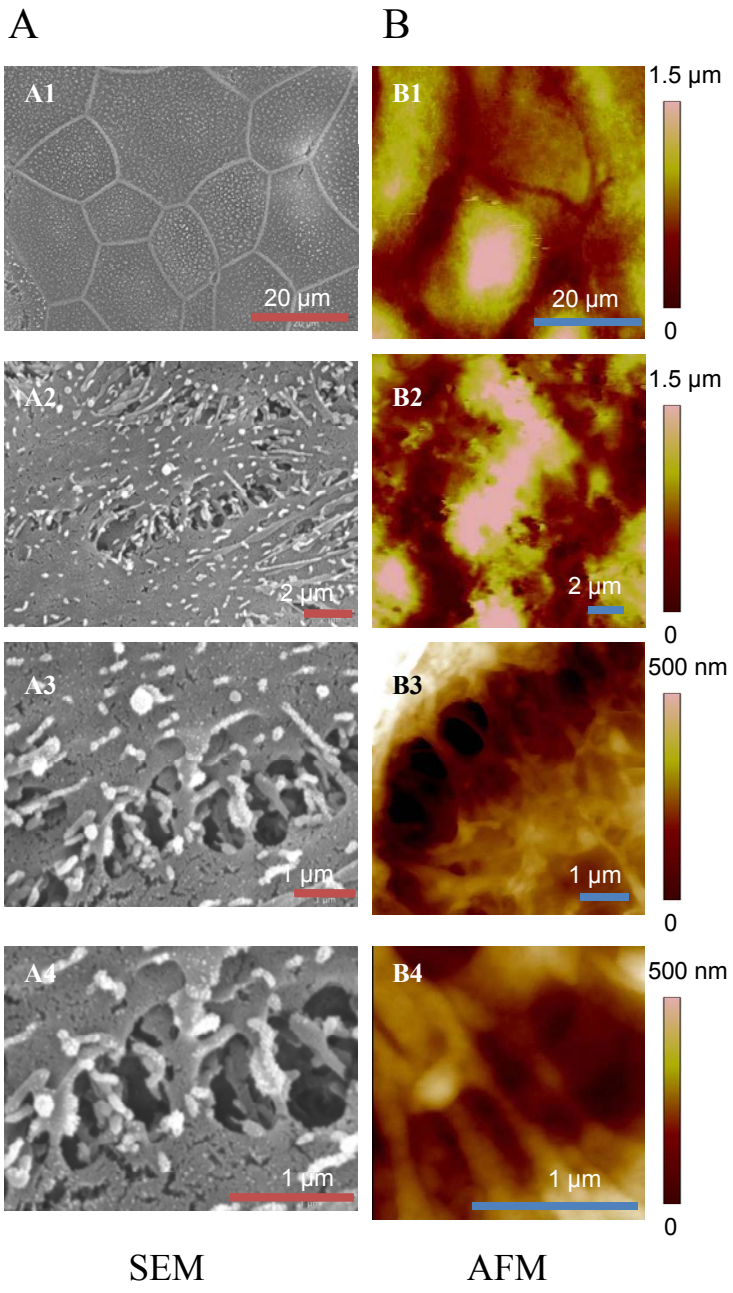

Figure 4.1 Integrated SEM and AFM imaging of intercellular adhesion structures. A: Correlation of SEM imaging with AFM imaging. Identically cultured plates of confluent HaCaT cells were fixed and imaged by SEM and Multimode AFM in increasing magnifications. The lower magnification images (SEM: A1, A2; AFM: B1, B2) show the cells with clear boundaries between neighboring cells where cell-cell adhesion occurs. The higher magnification images (SEM: A3, A4; AFM: B3, B4) show details of the adhesion junction with strand-shaped structures in parallel distribution between two cells.

4.2 Visualization of keratinocyte junctions under physiologic and disease conditions by AFM methods

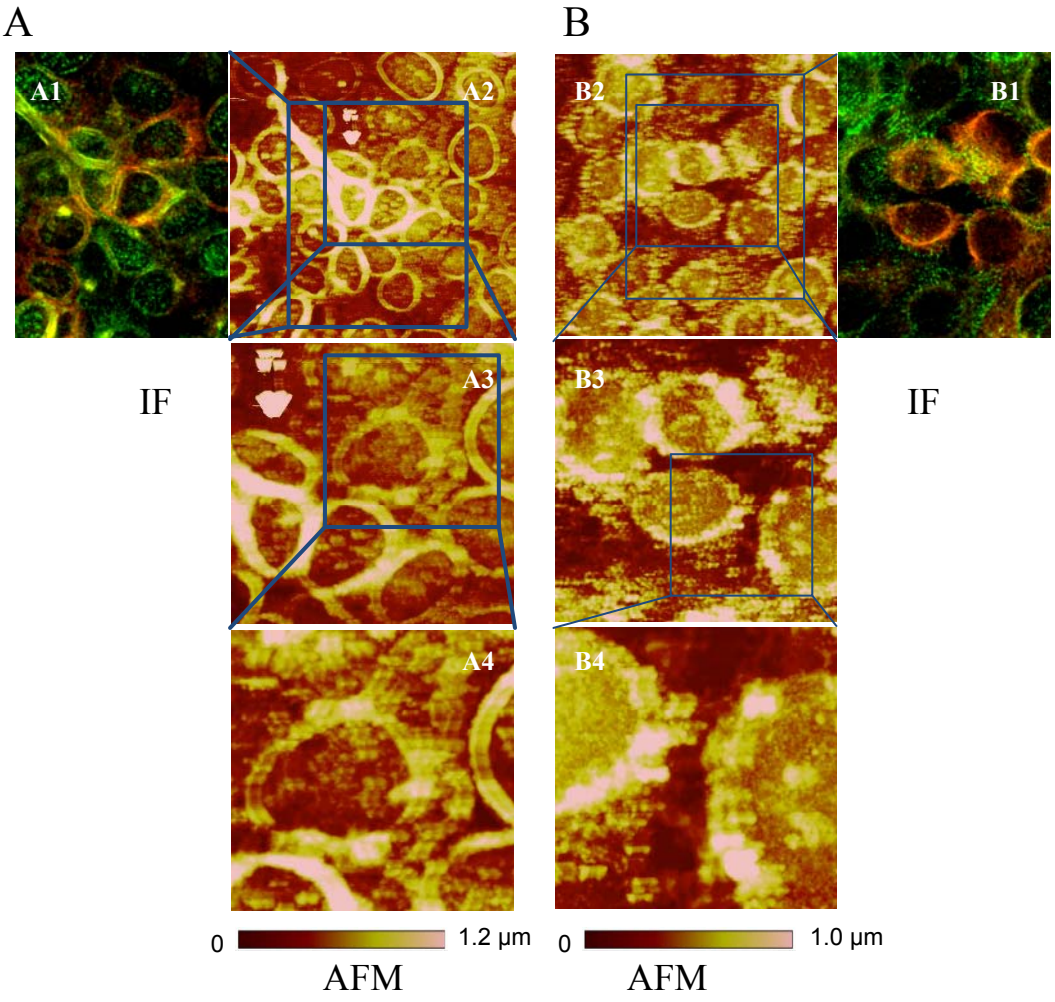

Figure 4.2 Integrated immunofluorescence (IF) and AFM imaging of intercellular adhesion structures. The same area on a confluent slide of HaCaT cells was captured simultaneously by IF and AFM after fixation of the cells. For IF imaging, HaCaT cells were labeled with anti-cytokeratin antibodies (red) and anti-desmoplakin antibodies (green). AFM images were captured by Bioscope AFM at increasing resolution with scan sizes of 100 μm (B2), 50 μm (B3) and 20 μm (B4). C: Correlation of IF imaging (C1) with AFM imaging [scan sizes of 100 μm (C2), 50 μm (C3) and 20 μm (C4) after treatment with 10 g/ml of the pathogenic anti-Dsg3 antibody Px4-3 for 24h

To validate the applicability of AFM for the investigation of cell-cell adhesion, we conducted high magnification AFM imaging of fixed HaCaT cells, a well-established keratinocyte cell line.

We show that the AFM images correspond well with SEM imaging (considered the gold standard in high resolution imaging of detailed intercellular adhesion structures in previous work [135])(Fig. 4.1A and B).

Next, we demonstrate a close correlation of AFM images with IF images that visualize desmoplakin, an anchoring protein that links desmosomal proteins to intermediate filaments (Fig. 4.2A, B). Autoantibody-treated cells (Fig. 4.2B) display a distinctive enlarged spacing between neighboring cells when compared to untreated cells (Fig. 4.2A), indicating cell dissociation that is clearly observed both by IF and AFM in fixed cells likely based on a rearrangement of desmosomal and cell-structural components [136].

In the higher resolution AFM images of untreated fixed keratinocytes (Fig. 4.3A), we observe structures in parallel organization between the cell membranes. However, in cells incubated with pathogenic anti-Dsg3 antibody or non-pathogenic anti-Dsg3 antibody for 24h, these structures linking adjacent cells are no longer clearly detectable (Fig. 4.3A and B, respectively), indicating that Dsg3-specific antibody binding leads to a perturbation of normal cell-cell adhesion. Conversely, the addition of two disease-irrelevant antibodies (goat anti-mouse Ig and mouse anti-human HLA A, B, C) does not alter the intercellular structures observed without treatment (Fig. 4.3C and D, respectively).

To visually follow disease processes in real-time, we obtained images of living keratinocytes in culture before and after treatment with the same test and control antibodies used above over a time-course of 30 min to 4 hs. Prior to antibody treatment (0h), multiple intact intercellular structures can be observed. After treatment with the blister-inducing pathogenic anti-Dsg3 antibody, an initial perturbation of cell-cell adhesion can be visualized between 30m-1h, with all cells completely disconnected after 2h (Fig. 4.4A), likely as a result of cytoskeletal reorganization as shown previously for pathogenic Ab attack [137]. Treatment with the non-pathogenic antibody,

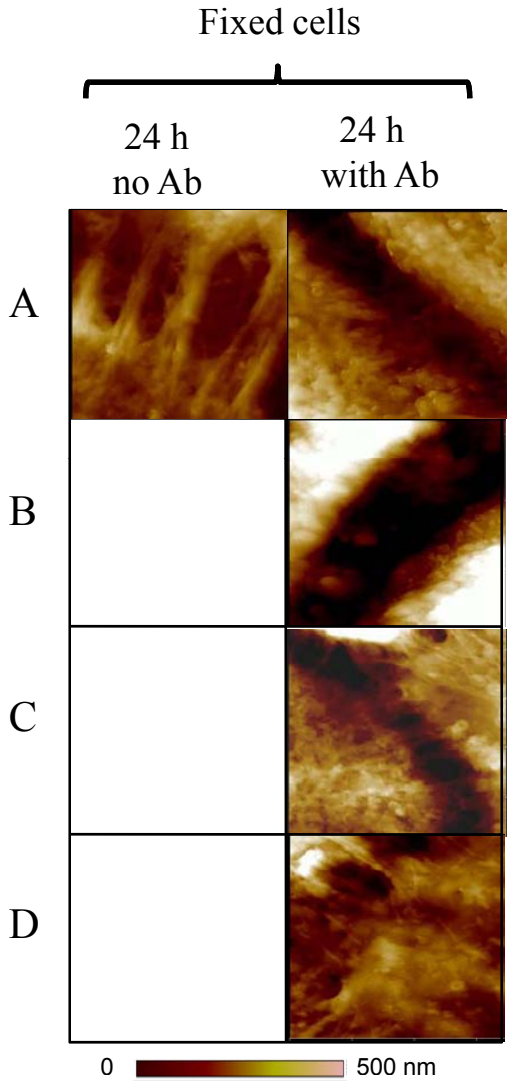

Figure 4.3 AFM imaging of autoantibody mediated desmosomal disruption in fixed cells. HaCaT cells were grown to confluence, and left with no antibody treatment, or were treated for 24h with (A) the pathogenic anti-Dsg3 antibody Px4-3, (B) non-pathogenic antibody Px4-4, (C) non-binding irrelevant control antibody goat anti-mouse Ig, or (D) irrelevant control antibody

which does not lead to blister formation in vivo, results in a similar initial disruption of cell-cell adhesion structures as seen with the pathogenic antibody. However, the non-pathogenic antibody associated changes appear with a delayed onset and do not lead to a complete loss of cellular shape (Fig. 4.4B). It is theoretically possible that the presumed “non”-pathogenic antibody does hold pathogenic potential at much higher concentrations per target cell not tested here. Neither of the

irrelevant control antibodies alters the intercellular structures between adjacent cells at the corresponding time points (Fig. 4.4C and D). These data demonstrate the facility of AFM technology not only to document autoantibody associated effects at static time points in fixed specimens, but also to track autoantibody mediated effects on intracellular adhesion in real-time.

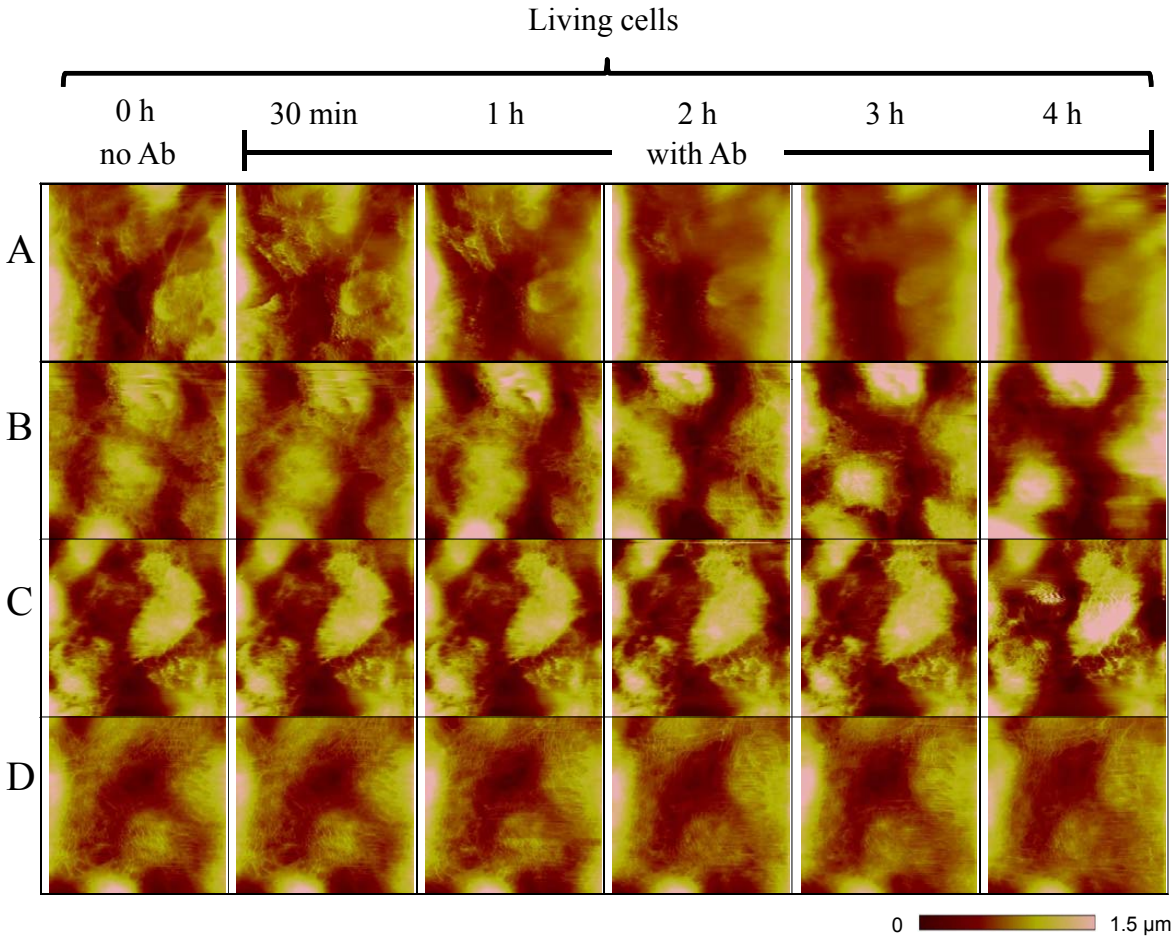

Figure 4.4 AFM imaging of autoantibody mediated desmosomal disruption in live cellsconfluent HaCaT cells were imaged live before antibody treatment or treated with the antibodies as in Fig. 4.3 for 30 min, 1 h, 2 h, 3 h, and 4 h

4.3 Mechanical characterization

4.3.1 AFM based quantification of cell surface stiffness reveals autoantibody-associated nanostructural changes

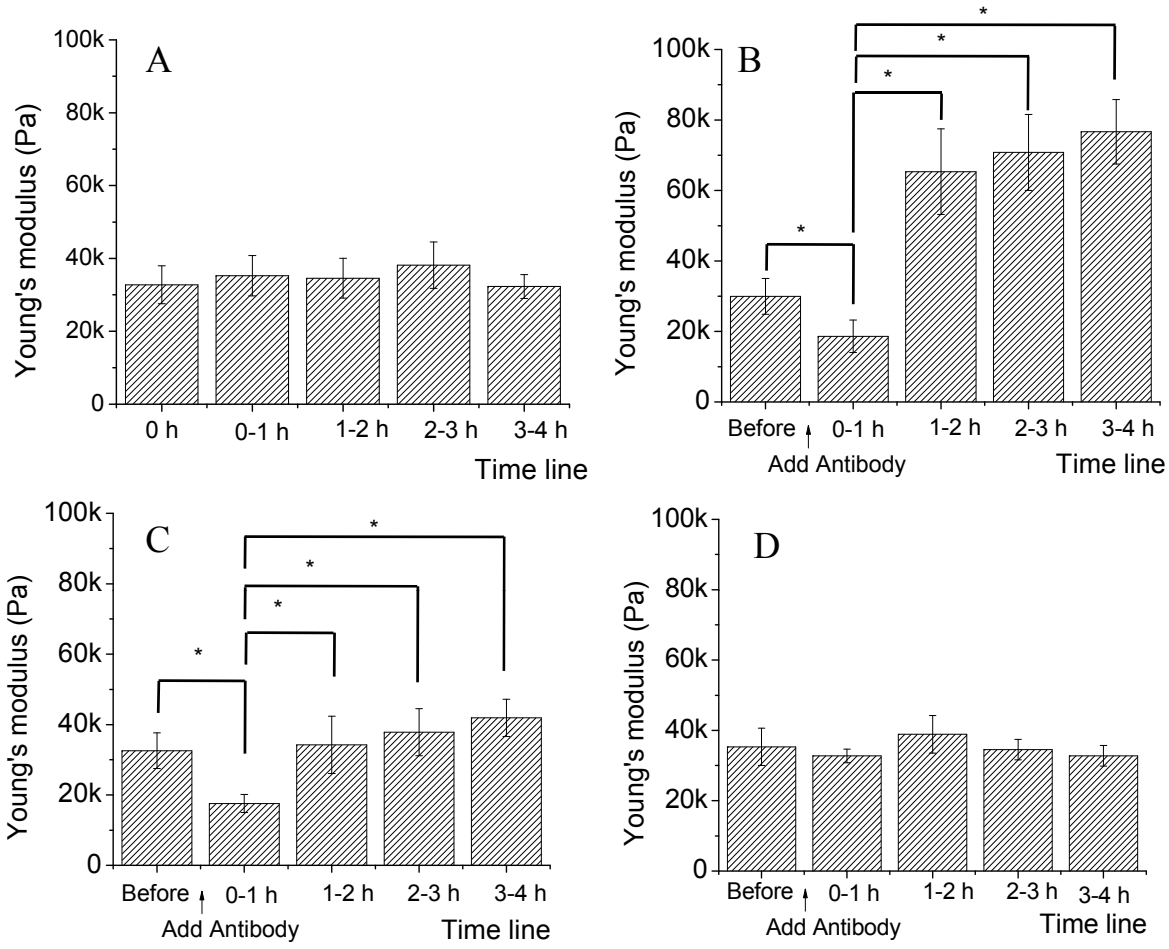

Figure 4.5 AFM-guided elasticity measurements on HaCaT cells before and after treatment with anti-Dsg3 and control antibodies. At each time point, between 20 and 40 HaCaT cells were tested, and the force curves obtained from these measurements were processed to generate the corresponding Young's modulus as a measure of cellular elasticity. In parallel experiments, measurement were obtained before antibody treatment and after treatment with 10 g/ml of the pathogenic anti-Dsg3 antibody Px4-3 (B), the non-pathogenic antibody Px4-4 (C), the non-binding irrelevant control antibody goat anti-mouse Ig (D).*$p<0.05$.

Dynamic mechanical properties of cells are increasingly being recognized as indicators and

regulators of physiological processes. For example, it has been shown that changes in cell elasticity/stiffness can effectively and reliably differentiate cellular conditions, such as non-cancerous vs. metastatic cells [28, 76, 138], or the induction of apoptosis [24, 139]. To obtain dynamic measurements under physiological and pathophysiological conditions, we continuously measured elasticity/stiffness changes over a 4-hour time course following antibody treatment of HaCaT cells. In untreated cells, or those treated with irrelevant control antibodies, the overall elasticity remained at the same level over the measurement interval of 4 hours with means ranging from 32 kPa to 36 kPa (Fig. 4.5A, B, and D, respectively). In the presence of the non-pathogenic antibody Px4-4, however, elasticity initially decreases within 2 hs from baseline levels of 32.5 ± 5.1 kPa to 17.6 ± 2.6 kPa, then returns to baseline after 2 hs, and remains between 35 kPa and 40 kPa thereafter, slightly higher than the initial value (Fig. 4.5C). In cells treated with the pathogenic antibody Px4-3, stiffness first drops at 1 hour to 18.6 ± 4.6 kPa, similar to the results with non-pathogenic antibody. However, in contrast to the non-pathogenic antibody condition, at 2 hs there is a consistent, sharp increase (three-fold) in stiffness to levels around 70 kPa for the remaining period (Fig. 4.5B).

4.3.2 Desmosome disruption by other means

To define the (patho-) physiological correlates of the early decrease in cell stiffness induced by both pathogenic and non-pathogenic antibody binding, we first investigated how the directed detachment of intercellular adhesion molecules via the manipulation of calcium levels in culture media (calcium depletion) or by nanorobotic surgical methods (nanodissection) affects elasticity measurements.

The formation of desmosomes requires the presence of calcium [140]. By depleting calcium from the growth medium in vitro, the formation of desmosomes can be interrupted. Calcium-depleted cells grow separately from their neighboring cells, or, if they had previously reached

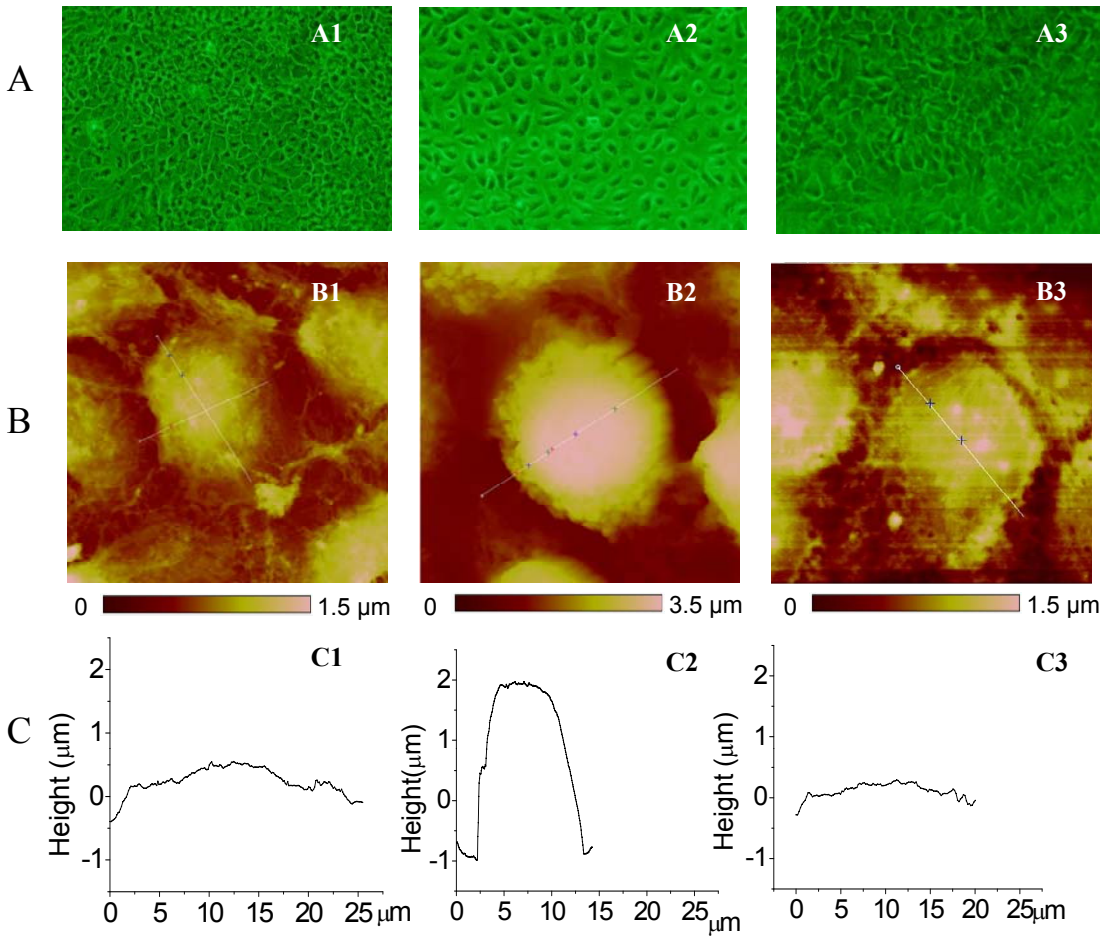

Figure 4.6 Cell desmosome disruption by calcium depletion.

confluence, dissociate from adjacent cells. In our experiments, cells grown in calcium-containing medium were shown to form stable cell attachments to their neighboring cells, have a somewhat flat appearance (diameter 25μm, height 1 μm), and intercellular filame nts bridging neighboring cells can clearly be observed (Fig. 4.6A1, B1, C1). Calcium depletion leads to a loss of cell-cell adhesion that can be observed microscopically by an enlarged spacing between cells, and via AFM by a disappearance of intercellular filaments (Fig. 4.6A2 and B2). Additionally, calcium depleted cells become approximately three times smaller in diameter (10 μm), but almost three times higher (3 μm) (Fig. 4.6C2). Once Ca^{2+} containing medium is reconstituted to cultures, cells recover to normal pre-depletion shape (Fig. 4.6A3, B3, C3). AFM-measurements of cellular stiffness at the 3

states (pre-depletion, post-depletion, and recovery) show that the loss of intercellular adhesion, and thus change in cell shape, is tightly correlated with a decrease in cellular stiffness (from 36.5 $\pm$4.7 kPa to 19.1 $\pm$ 3.9 kPa). The re-formation of intercellular adhesion, however, restores stiffness back to levels seen before the loss of cell-cell connections (35.2 $\pm$6.7 kPa).

As an alternative method of disrupting intercellular adhesion, we performed novel, targeted nanodissection at the intracellular adhesion junction of keratinocytes using an AFM based nanorobotic surgery system. Corresponding AFM measurements of cellular elasticity indicate that the stiffness of an individual HaCaT cell decreases after nanodissection. The detailed process of AFM nanosurgery will be discussed in Chapter 5.

Both the calcium depletion, as well as the nanorobotic manipulation experiments indicate that a disruption of intercellular adhesion leads to a dependable decrease in cellular stiffness as measured by AFM, and are consistent with the initial decrease in cell stiffness measured by AFM within one hour after addition of autoantibody. Our data fits well with reports in the literature that see early effects of PV IgG on cell adhesion [141, 142] and cytoskeleton disassembly [143] within 30 min to 2 hs. While significant Pemphigus IgG induced acantholysis usually takes 12-24 hs to occur (reviewed in [141]), complete loss of cell adhesion has been observed within 1-6 hs after antibody treatment with pathogenic antibody in experimental models [144].

To define the (patho-) physiological correlates of the later increase in cell stiffness induced by pathogenic-, but not non-pathogenic antibody binding, we next investigated whether the internal remodeling of the cytoskeleton and nucleus in cells undergoing apoptosis is reflected in dynamic changes in the structural properties of the cell that are measurable by AFM, as has been suggested [24, 139]. While the morphological characteristics of apoptosis are not necessarily detected in the histopathology of PV lesions, increased expression of apoptotic signaling molecules has been detected in both PV lesions and patient serum when compared to healthy controls, and PVIg

can trigger the activation of apoptotic signaling pathways in vitro [145]. Thus, we investigated whether the late increase in cell stiffness detectable at 2 hs after pathogenic antibody treatment has its pathophysiological correlate in an induction of apoptotic processes by exploring the extent to which (i) apoptosis is induced by pathogenic anti-Dsg3 antibodies, (ii) similar levels of cell stiffness increases can be observed with established inducers of apoptosis, and (iii) the antibody induced stiffness increase can be reversed by blocking apoptotic signaling.

4.4 Two-hit hypothesis

We first measured whether pathogenic anti-Dsg3 antibodies induce an activation of apoptotic pathways in cultured keratinocytes. In cells treated with pathogenic anti-Dsg3 antibodies, we observe an increase in combined Annexin V and PI positivity starting at 4h, with a peak at 12h and a return to baseline levels at 24h (Fig. 4.7). The non-pathogenic antibody induces a slight increase in Annexin V and PI positivity as well, but this increase does not reach significant levels at any time point, peaks later (around 16h) and returns to baseline levels earlier (at 20 hs) (Fig. 4.7). The return to baseline levels within 24 hour after pathogenic antibody treatment indicates that the cells, while exhibiting apoptosis-related phenomena, have not undergone terminal apoptosis. Our data support previous findings by Pelacho et al. [146] that showed nuclear changes characteristic of apoptosis, with a clear peak after an 8h incubation with PV-IgG, but a decrease thereafter.

Contrary to long held beliefs about the irreversible fate of apoptotic cells, it has recently been shown that the initiation of apoptosis can be reversible with only transient exhibition of morphological signs of apoptosis at the cellular level [147]. Additionally, phosphatidylserine (PS) externalization (as measured by Annexin V binding in this study) is not restricted to apoptotic cells but has also been described for human CD8 cytotoxic T lymphocytes that reversibly expose PS upon

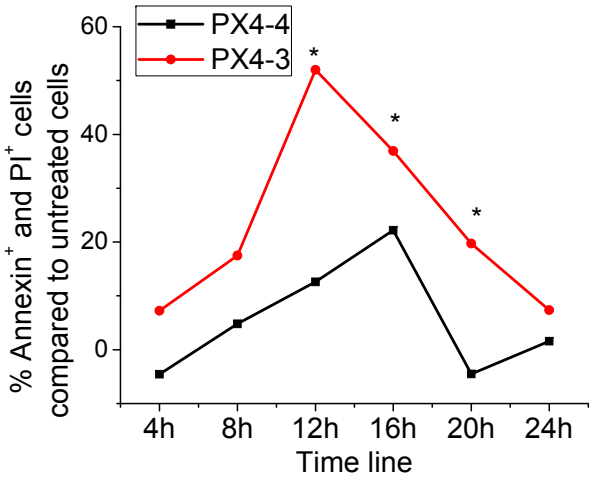

Figure 4.7 Apoptotic processes are induced by nonpathogenic and pathogenic anti-Dsg3 antibodies

T-cell receptor mediated antigen recognition [148]. Thus, the reversible PS externalization seen in our study may indicate an antigen recognition-mediated initiation of apoptotic signaling cascades that has the potential to, but does not necessarily progress to apoptotic cell death in all conditions.

To verify that the sustained increase in cellular stiffness observed after pathogenic anti-Dsg3 antibody binding can also be found as a result of apoptosis induction, we used the well established apoptosis-inducer Fas ligand (FasL) [149]. Addition of FasL significantly increases the number of apoptotic HaCaT cells in culture, while pretreatment of FasL-treated cultures with FasL neutralizing antibody significantly reduces FasL-induced apoptosis back to baseline levels. Parallel AFM force measurements show that untreated HaCaT cells and Fas ligand treated cells have a low peak in their stiffness distribution around 30 kPa and a high peak around 80 kPa. In FasL treated cells the high stiffness peak sharply increases (28% of all cells, Fig. 4.8B2) when compared to untreated cells (12 %, Fig. 4.8A2). When apoptosis is blocked by FasL neutralizing antibody, the second peak of higher stiffness completely disappears (Fig. 4.8C2). The AFM measurements are echoed by the data obtained from flow cytometry of the corresponding groups (Fig. 4.8A1,B1,C1). These data indicate that the induction of apoptosis in HaCaT cell cultures leads to a sharp increase in cell

stiffness.

In order to provide evidence that the secondary increase in cellular stiffness produced by the pathogenic autoantibodies is due to the induction of apoptosis, we attempted to block apoptosis in pathogenic anti-Dsg3 antibody treated cells by (a) inhibiting all caspases, a family of cysteine proteases that play essential roles in programmed cell death, or by (b) blocking the Fas/FasL pathway. Compared to baseline (Fig. 4.9A), addition of Px4-3 pathogenic antibody leads to a sharp increase in the number of cells with higher stiffness (22.5%, Fig. 4.9B), that is similar to the distribution of cell stiffness (both in terms of percentage of cells showing cellular stiffening as well as Young's modulus values) as treatment with FasL (see Fig. 4.8B2). Pre-treatment of HaCaT cells with caspase inhibitor before addition of Px4-3 antibody completely abrogates the development of cells with a stiffer profile, even below background levels (Fig. 4.9C), indicating that anti-Dsg3 antibody-induced apoptosis and blocking thereof can be monitored by AFM stiffness measurements. Pre-treatment of HaCaT cells with FasL neutralizing antibody before addition of Px4-3 antibody, however, does not reduce the number of stiffer cells (Fig. 4.9D).

The disparate findings regarding the blocking of caspases or the FasL pathway indicate that while inhibition of apoptotic processes can reverse pathogenic autoantibody mediated phenomena, they are not mediated by the Fas/FasL signaling pathway. The inability of FasL neutralizing antibodies to reverse the pathogenic antibody-induced increase in stiffness is somewhat surprising, as an activation of the Fas-FasL apoptotic pathway has repeatedly been implicated in PV pathomechanisms [150–152]. However, previous studies relied on observations from biopsy materials or in vitro studies with patient sera or purified IgG. It has been shown that sera from untreated PV patients contains high levels of FasL [150], which could conceivably lead to apoptosis independent of the effect of anti-Dsg antibodies. This notion is supported by the fact that inhibition of FasL or caspase 8 can only partially inhibit PV sera induced apoptosis [150]. In addition to

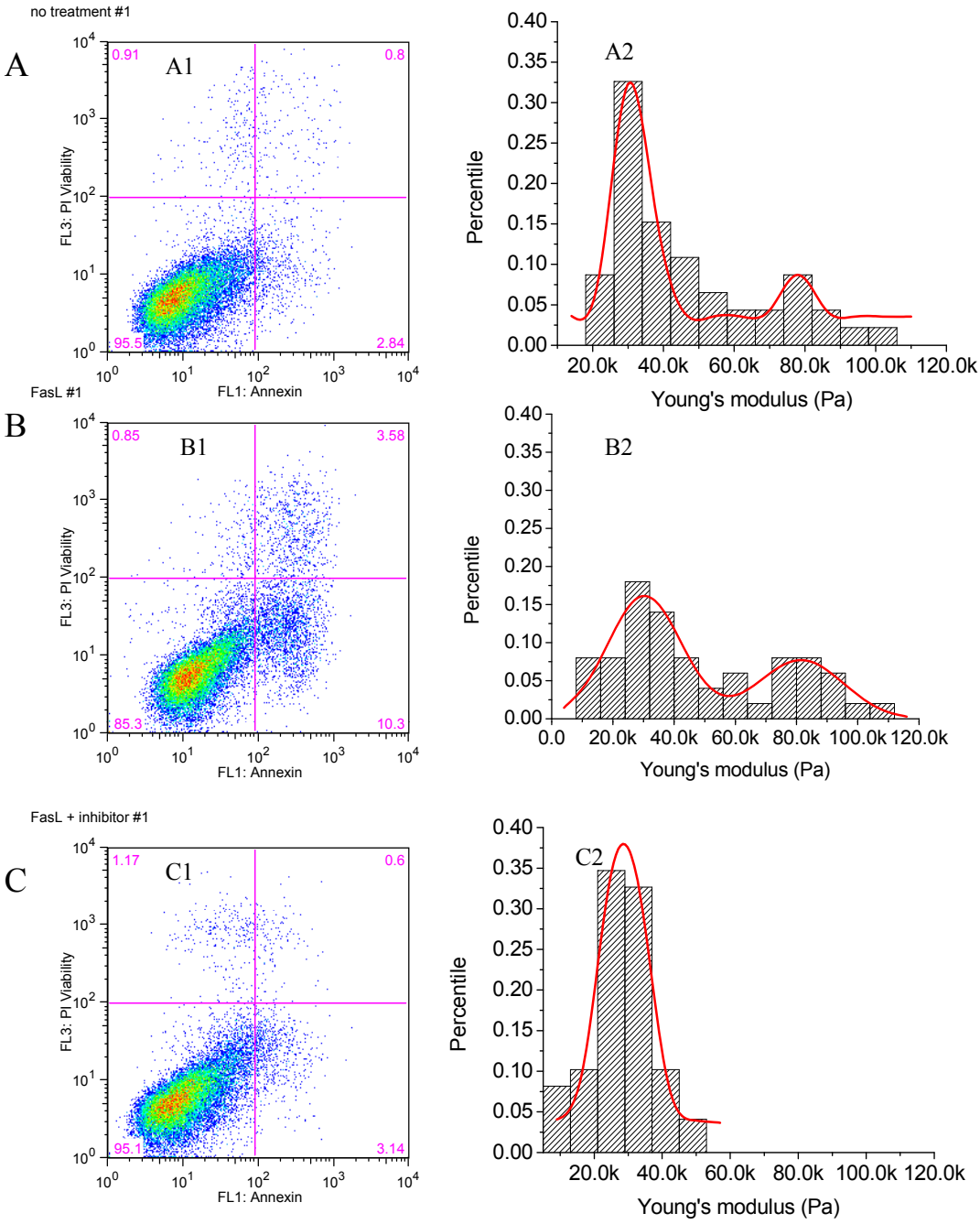

Figure 4.8 Apoptotic processes are induced by pathogenic anti-Dsg3 antibodies detected by flow cytometry and AFM nanomechanical analysis. A: No treatment; B: pathogenic antibody treatment and C: pathogenic antibody treatment blocked by FasL inhibitor

containing FasL, serum autoantibody profiles vary among patients and may contain autoantibodies to targets other than Dsg [153], whose effects have not been well studied. In this study, we use a well-characterized and reproducible source of pathogenic PV anti-Dsg mAbs [131, 144] with non-pathogenic PV anti-Dsg mAbs as controls, in order to discern effects that can be attributed solely to the action of anti-Dsg3 on its cellular target.

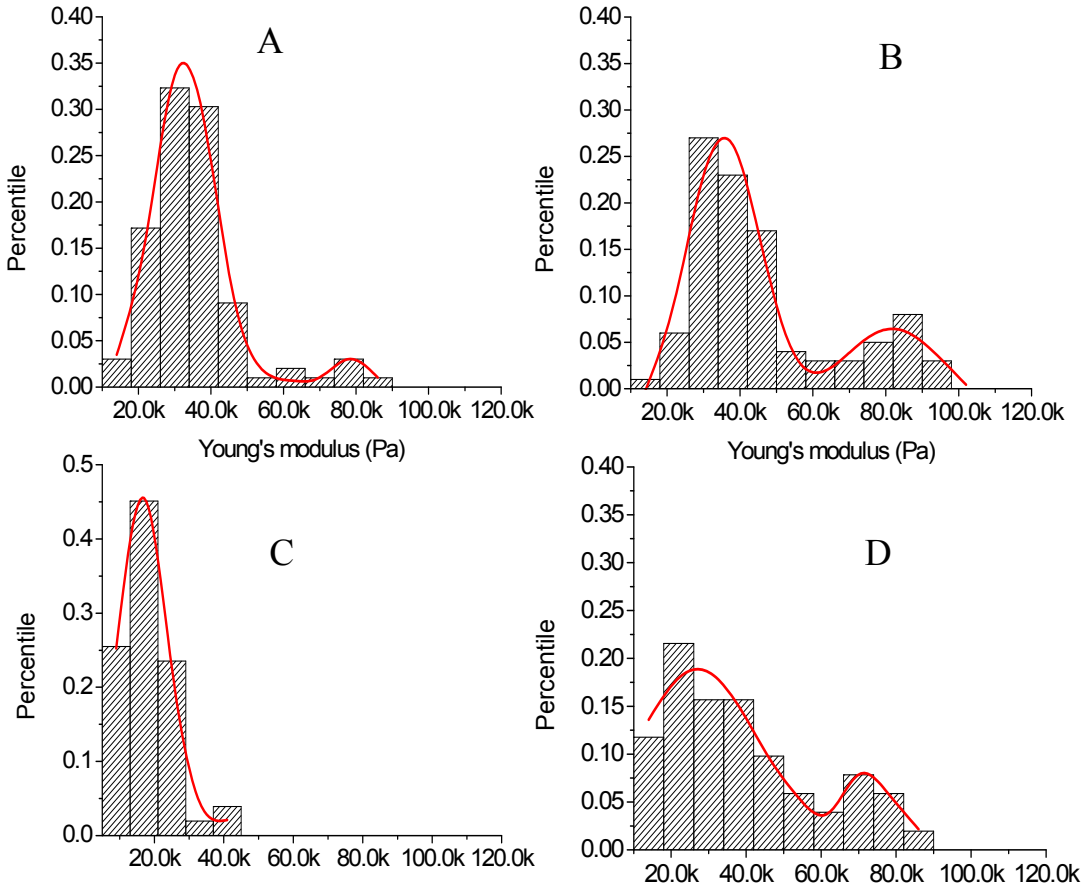

Figure 4.9 The pathogenic anti-Dsg3 antibody-induced increase in keratinocyte stiffness can be blocked by caspase inhibitor, but not by Fas ligand neutralizer

Similar to FasL, activation of caspases has been observed in PV model systems, and caspase inhibitors have been shown to block PV IgG-induced acantholysis in keratinocyte monolayers and skin organ culture [154]. Our finding that a caspase inhibitor can completely abrogate anti-Dsg3 induced changes in cell stiffness supports the notion that apoptotic signaling mechanisms are indeed

involved in the downstream processes after antibody binding. However, as stated earlier, apoptotic signaling in PV may not necessarily progress to cell death, but exert its influence elsewhere, such as by targeting proteins involved in the regulation of cell contacts and of the cytoskeleton during [155]. As such, caspase 3 has been shown to specifically cleave the cytoplasmic tail of Dsg3 and help release its extracellular domain from the cell surface, resulting in the disruption of the desmosome structure and contributing to cell rounding and disintegration of the intermediate filament system [154]. Along these lines, our ability to block anti-Dsg3 induced cell stiffening by blocking caspases could simply reflect an inhibition of Dsg3 cleavage, and not apoptosis. However, in keeping with our own data on the disruption of i.c. adhesion structures presented above, a disintegration of the keratin network should lead to cell softening and not stiffening. Thus, it is conceivable that the anti-Dsg3 induced cell stiffening observed by AFM in this study can be viewed as a sensitive marker for the early initiation of apoptotic signaling pathways that may contribute to cellular dissociation, but not necessarily reach full apoptotic cell death.

4.5 An integrated model for antibody-mediated damage in the skin

Three major hypotheses have been proposed regarding the mechanisms by which anti-Dsg antibody binding to the cell surface leads to acantholysis: (i) “steric hindrance”, the direct inhibition of Dsg transinteractions [156, 157], (ii) depletion of desmosomal proteins from the keratinocyte surface [158], and (iii) initiation of signal transduction events that lead to altered desmosome assembly, cytoskeleton derangement, cell cycle alterations, and apoptosis [159]. However, to date, there is no conclusive theory of antibody-mediated acantholysis, and the role of apoptosis is unsettled [145]. While apoptotic phenomena have been observed in PV, there is considerable disagree-

ment regarding its role in acantholysis. Some groups have shown that acantholysis can occur in the absence of apoptosis [160], and find that hallmarks of apoptosis, such as changes in nuclear morphology and cell death, are detectable only late and subsequent to acantholysis [145]. Others favor the theory that apoptotic signaling precedes acantholysis, but necessarily leads to apoptosis, and have termed this paradigm "apoptolysis" [161]. The data presented in this study support the notion that a dissociation of cell adhesion structures precedes the detection of apoptotic signaling phenomena after pathogenic antibody attack.

While it has been suggested before that multiple steps are needed for PV mAb-initiated acantholysis [160, 161], we propose a novel "2-Hit hypothesis" of anti-Dsg3 autoantibody effects in PV. "Hit 1" reflects structural changes in the keratinocyte that are induced both by pathogenic and non-pathogenic antibodies. "Hit 2" involves a functional change in the keratinocyte biology that is promoted by pathogenic, but not non-pathogenic antibodies. In this model, "Hit 1" has the pathophysiological correlate of an initial, but incomplete cellular dissociation, while "Hit 2" correlates with the initiation of apoptotic signaling pathways. Given that the non-pathogenic antibody leads to an initial cellular dissociation that is also seen with pathogenic antibody binding, but does not alter the overall shape of the cell and does not induce the later cell structural changes seen with pathogenic antibodies, it follows logically that "Hit 2" is needed to progress to clinical disease, while "Hit 1" may be a reversible phenomenon.

4.6 Chapter summary

While AFM has been previously used to study the binding properties of anti-Dsg1 and 3 antibodies to planar surfaces in a cell-free environment [158, 162], we have for the first time established novel nanorobotic AFM technologies for the investigation of PV pathomechanisms in vitro. We show

that, in addition to visually tracking the effects of anti-Dsg3 autoantibody binding on cellular adhesion in high resolution and real-time, AFM can reliably detect nanostuctural changes at the cell surface in response to pathogenic and non-pathogenic antibody binding and downstream signaling events that allow conclusions regarding disease pathomechanisms relevant to autoimmunity. We demonstrate that AFM is an exquisitely sensitive technique capable of detecting cellular mechanostructural changes at a higher resolution and at earlier time-points than standard techniques, and could, thus, serve as an excellent investigative tool and predictive screen to assess the impact disease associated disturbances in defined cellular parameters and functional pathways and blockage of those pathways with potential novel therapeutic agents.

Chapter 5

Modeling and experimental verifications of cell tensegrity

5.1 Introduction

The tensegrity cell model is a qualitative modeling technique for adherent cells [85]. It has been proved to be consistent with the mechanical behavior of living cells [163]. The main concept in delineating the mechanical properties of cells is that the cell body is a tensional integrity structure, thus the name *tens*egrity. The cytoskeleton behaves as a discrete mechanical network composed of three elements: microtubule, actin filament and intermediate filament [92]. The three elements have different mechanical property themselves. In that, microtubule is the stiffest of the three and thus would bear the compressional force when the cytoskeleton is compressed; while actin filament and intermediate filament would assume more tension when the cell is stretched [85]. Through the inter-connected cytoskeletal network, cells would maintain the structure integrity under different force interactions.

It is generally accepted that cell can establish tensegrity force balance with its cytoskeletal network and the ECM. The ECM provides the external support for the force balance, in which the integrin of cells binds to ECM in the formation of the so-called focal adhesion complex [164]. The focal adhesion sites are discrete, non-uniform protrusion regions of the cell periphery [59]. On one hand, they provide the linkage between the cell and ECM, and at the same time serve as the

signaling transduction hub. They also host a cluster of proteins that behave as force sensors [59].

In tensegrity force balance, pre-stress in the filaments is a major factor governing cell mechanics. Under certain force balance or structural configuration, cell will have a corresponding pre-stress, and ultimately a certain level of elasticity that can generally be revealed by AFM probing. Thus by measuring the elasticity of the cell, either locally or globally [89], the pre-stress of the cell can be determined and its physical configuration can be predicted. Therefore to determine whether cells can be modeled as tensegrity structures, one would need to tune the cell pre-stress by biochemically modifying its living conditions and monitor whether the elasticity changes accordingly.

Metastatic adenocarcinoma cells show anchorage-independent growth patterns, and they become round in shape; whereas normal mesothelial cells show a large, and more stretched morphology. Experiments have verified that the cancerous type is seventy percent less stiff [76]. From the force balancing perspective, cells with weak focal adhesions should less pre-stressed than cells with stronger and denser focal adhesions. An analogy can be drawn for the cells with focal adhesion of different strength and the tent set up with varied number of anchors to the ground. Another evidence that signifies the difference in pre-stress lies in the cytoskeleton structure itself, when cells are less pre-stressed, they tend to have a disorganized actin filament network [165], a sign of less tensional forces in individual actin filaments.

The tensegrity modeling of adherent cells is normally about single cells and only cell-ECM interaction is considered in most cases. Cell-cell interactions, although often ignored when considering cell anchorage, could also be a source of external support in term of force balancing. Being a special type of cell-cell adhesion structure, desmosome is one of the main cell-cell adhesion complexes in epithelial cells, provides mechanical strength to maintain the tissue integrity. Desmosome links the intermediate filaments of neighboring cells through cadherin type of adhe-

sion. From the development point of view, desmosomes from different layers of epidermis vary in size and appearance: basal layer epidermis have less-organized desmosomes with smaller dimensions compared with desmosome in the suprabasal layers [166]. Apparently, cells at the suprabasal layers are tougher and stronger. We speculate that when desmosome becomes denser, cellular tension becomes stronger and the pre-stress becomes larger. All these evidences point to the idea that cell-cell adhesions, especially desmosomes play an important role in providing the external support just like focal adhesions do. In this study, we put this hypothesis into test by modulating the cell-cell adhesions between neighboring cells using biochemical and mechanical methods, we were able to obtain quantitative stiffness data validating the change of cellular stiffness.

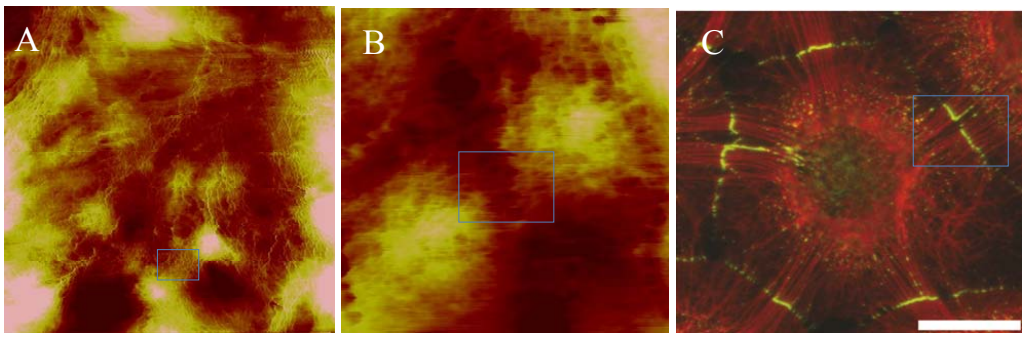

Figure 5.1 Desmosome structure with different desmosomal proteins connecting each other all the way to the intermediate filaments. AFM image and zoom-in (B) correlates with fluorescence image (C)

5.2 Desmosome disruption leads to decrease in cell stiffness

Keratinocyte is a major constituent of the epidermis and is abundant in desmosome-based cell-cell adhesions (Fig. 5.1). As mentioned above, desmosome provides the strength to maintain the mechanical integrity of the tissue by "spot-welding" the intermediate filaments from neighboring cells. Desmosome is composed of a cluster of proteins to form a molecular structure. The desmo-

some complex employs the cytoplasmic protein plaque to tether to the intermediate filament. To disrupt the connection between neighboring cells would require the disassembly of the desmosome, which would release the intermediate filament linkage, which normally plays the role of anchor points. The disassembly of the desmosome would therefore remove the anchor points from the tensegrity structure and ultimately reduce the amount of stress in the system. This hypothesis was verified by two biochemical experiments.

5.2.1 Desmosome disassembly results in stiffness decrease

The desmosome sometimes can be damaged in certain diseases, and one of them is called PV, a potentially fatal autoimmune disease that targets one of the proteins in the complex, Dsg3 [145]. The binding of the autoimmune antibody would caused the release of the protein from the complex and eventually leads to the disassembly of the desmosome structure. The damaged desmosome leads to the loss of cellular adhesion between neighboring keratinocyte cells and eventually causes blistering of the skin from the body fluid underneath the cells.

We tested the effect of the autoimmune antibody in vitro on keratinocytes. The administration of anti-Dsg3 antibody induced the loss of cellular adhesion structures. This was confirmed by comparing images obtained before and after the administration of the antibody. The AFM images show the enlarged spacing between neighboring cells, a clear evidence of cell adhesion loss, as well as retracted filament structures from the cell peripheral [10]. The topographical change is accompanied by the decrease of the cell stiffness as measured by AFM based nanoindentation. The Young's modulus value of normal cells dropped from 29.8 ± 4.9 to 18.6 ± 4.6 kPa for anti-Dsg3 antibody treated cells (Fig. 5.2A).

Since the formation of desmosome requires the presence in the growth medium of Ca^{2+}, which would form covalent bond with the desmosomal protein Dsg [167]. Depletion of the Ca^{2+} in the

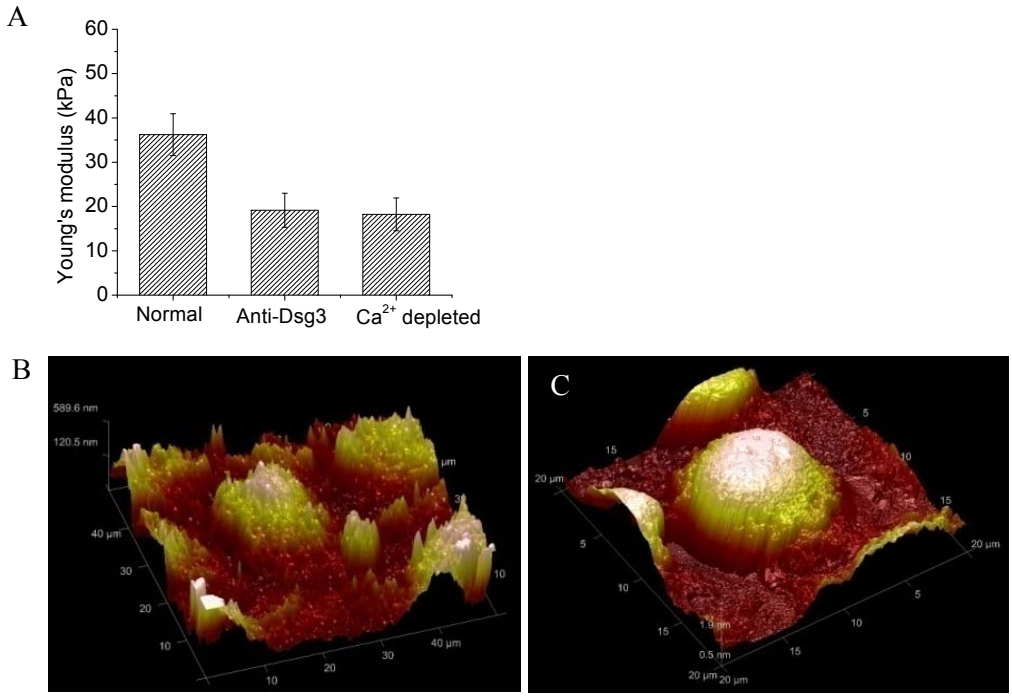

Figure 5.2 Young's modulus comparison for normal and calcium depleted cells

growth medium would hinder the formation of desmosome between cells. AFM imaging shows a significant difference in terms of dimensions for cells cultured in normal growth medium and the ones from mediums with Ca^{2+} depleted. Normal cells are stretched with a diameter around 25 μm and a height around 1 μm; while Calcium depleted cells are rounded up with a diameter around 12 μm and a cell height around 3 μm. The stiffness of both types of cells were also measured and compared. The Young's modulus values agree well with previous measurements for normal cells and antibody treated cells. The stiffness decreases from 36 ± 4.7 kPa to around 19 ± 3.9 kPa for normal and Calcium depleted cells in Fig. 5.2A. These biochemical methods indeed verified that the disruption of desmosome would lead to the decrease in cellular stiffness, an indication of reduced pre-stress in the tensegrity-based cytoskeletal structure. The release of intermediate filament connection was induced by desmosome disassembly or non-formation. We then demonstrated that by severing the intermediate filament mechanically and directly, we could

also achieve the similar effect.

5.2.2 AFM based nanosurgery resulting in the decrease of stiffness

There have been reports of nanodissection on fixed rat aortic smooth muscle cells [21] and mouse endothelial cells [168]; in both cases, a 'scar' was created successfully on top of the cell surface. The dissection of live cells proves to be more complicated than fixed cells. Once fixed, the polymeric structure of the cell membrane as well as the cytoskeleton will be cross-linked, evidenced by the large increase of stiffness of fixed cells [113]. Thus fixed cellular bodies can be regarded as a single material structure. However, live cells display distinct mechanical properties, elasticity in their delicate membrane and the cytoskeleton structure and viscosity in their cytoplasm. It was shown that intermediate filaments have extremely high tensile strength by AFM stretching [53, 169, 170]. Therefore, it behaves as a composite material structure. To dissect the intermediate filament network inside the cell poses larger challenges (illustrated in Fig. 5.3A). The cell body will deform when the AFM tip is pushed against the membrane. A tip sharp enough is required to penetrate the cell membrane before it reaches the cytoplasm and the intermediate filaments. Moreover, the lateral force, which is the primary driving force that causes the incision should be controlled to cut through the filament and also monitored to confirm the dissection is successfully done.

The force displacement curve in Fig. 5.3C shows the whole process when the AFM tip was driven towards the cell membrane until it penetrates the cell membrane compared with the process without penetration in Fig. 5.3B. Beginning with the contact point denoted as the circle when the AFM tip starts to deform the cell membrane and when the laser detector starts to detect vertical deflection; subsequently at certain point when tip deflection large enough, AFM tip generate a force to penetrate the cell membrane. The penetration force was observed when there is a sharp drop

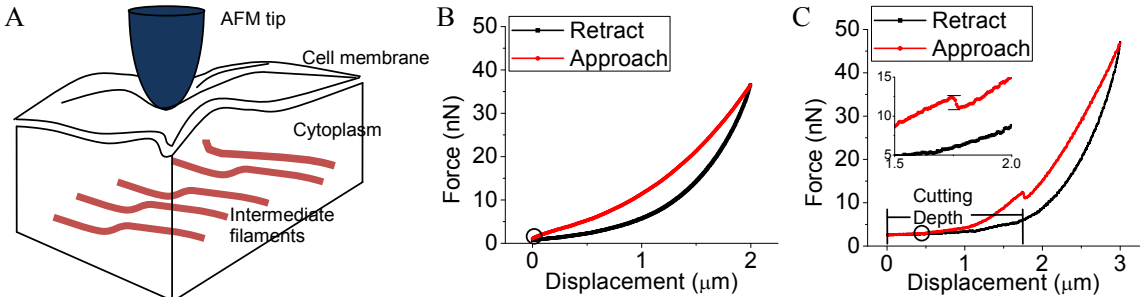

Figure 5.3 A: Illustration of composite cell structure during cell indentation and dissection; B: Force-displacement curve without penetration of the cell membrane; C: Force displacement curve with penetration of the cell membrane with the kink zoomed-in in the inset.

of repulsive force indicating a smaller resistance of cytoplasm compared with the cell membrane. The measured penetration force for keratinocytes is around 1.9 ± 0.5 nN. The distance traveled by the vertical piezo actuator between the contact point and penetration point can be used as a guide to set the overall cutting depth for the nanomanipulation operation.

AFM force measurement has been applied in investigations of biological process. Most of these applications focus on the normal force obtained from vertical deflection of the cantilever. For AFM based nanodissection, we utilize the lateral force to cut through the elastic filament structures. By maintaining a constant normal force and moving the AFM cantilever horizontally, the lateral deflection of the cantilever can be obtained (as illustrated in Fig. 5.4A) from the PSD signal. The normal force applied to the cantilever was determined by the depth of penetration and depth of AFM tip contacting the substrate underneath as measured by force displacement in the previous section.

The lateral position of the AFM tip was determined by a pre-defined trajectory around a specific cell shown as the 3D construction of the original AFM image from the custom-made nanomanipulation software in Fig. 5.4C. When moving along the trajectory, at each time t, the cutting force in the planar direction can be determined by $F = F_l/\cos(\theta)$, where F_l is the lateral force due to the

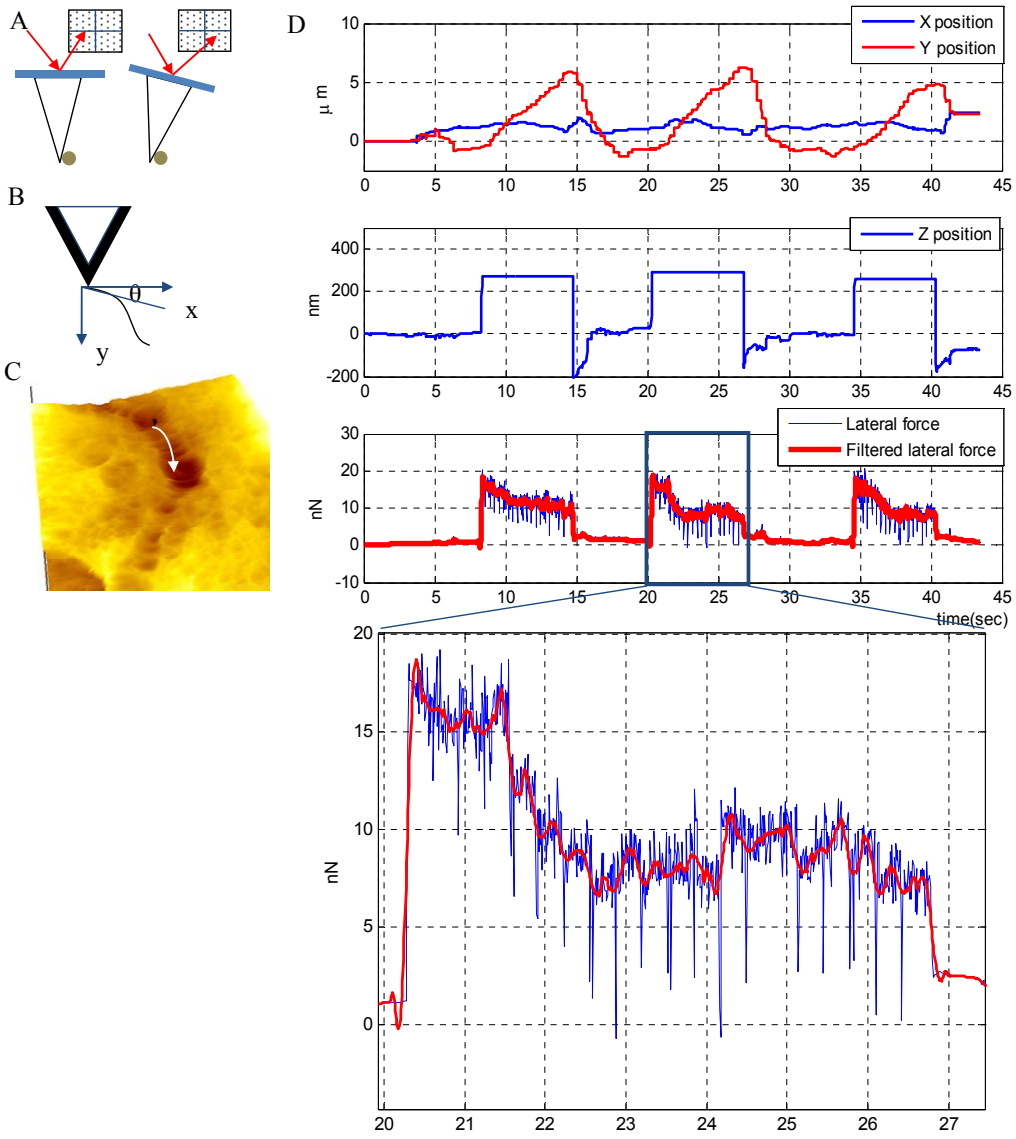

Figure 5.4 A:The lateral force was the laser position shift in the horizontal direction on the detector; B: The tangent direction of the trajectory defines the angle (θ) between the cutting force F and the lateral force F_l ; C: The trajectory of the nanosurgery on the cell peripheral between neighboring cells with the black triangle indicating the tip position; D: the XY position, cutting force and the Z piezo position in the process of the nanosurgery along the path in C with a cutting depth of 100 nm.

twist of the cantilever perpendicular to its longitude direction and θ is the angle at each position (illustrated in Fig.5.4B). The trajectory was then translated to position information, which directs the lateral movement of the probe. A real time measurement data was shown in Fig. 5.4D, in which

the XY position, the cutting force F and the Z cutting depth were recorded. Three repeated cutting procedures were performed, the lateral movement is at 1.5 $\mu m/s$ maximum for both X and Y; while a constant Z position is maintained immediately when the probe engages with the cell sample. The maximum cutting force recorded during the operation was around 20 nN. Similar force profile was observed for all three cutting procedures, it was maintained at higher level less than 20 nN for about 2 seconds before lowered to around 10 nN. Sudden release of force to extreme low levels, or spikes, in the force profile should be caused by the snap of bundles of intermediate filaments. Images in Fig. 5.5A and B show the AFM image before and after three repetitions of nanosurgery with cutting depth of 100 nm. A line segment section at the working area shows the topographical change in Fig. 5.5C and D. The filaments structures were removed as indicated by the height decrease in the topography image, and the removal was controlled within 300 nm.

The stiffness data was collected before and after the dissection operations, which cut off the connections between neighboring cells through repetition of nanosurgery. The Young's modulus value drops from 36.1 ± 3.5 kPa to 18.4 ± 1.9 kPa (Fig. 5.6). Thus it is conclusive that the stiffness of cells follows the same pattern as antibody treated cells and Calcium depleted cells. The well-connected cells are around 1.5-2 times stiffer than the cells whose intermediate filaments are cut loose thus lose their anchoring point from neighboring cells. The well-connected cells with intact cell-cell adhesion are around 1.5 times stiffer than the cells whose intermediate filaments are cut loose. When cells are modeled as tensegrity, prestress determines the mechanical response of the whole cytoskeleton structure to external load such as the nanoindentation force from the probe. With less external support from intermediate filaments of their neighbors, cells would have to establish a new force balance, one which presumably receives no contribution from tension in the intermediate filaments. Theoretical calculation was then performed to verify the stiffness change with and without intermediate filament tensions in the structural model.

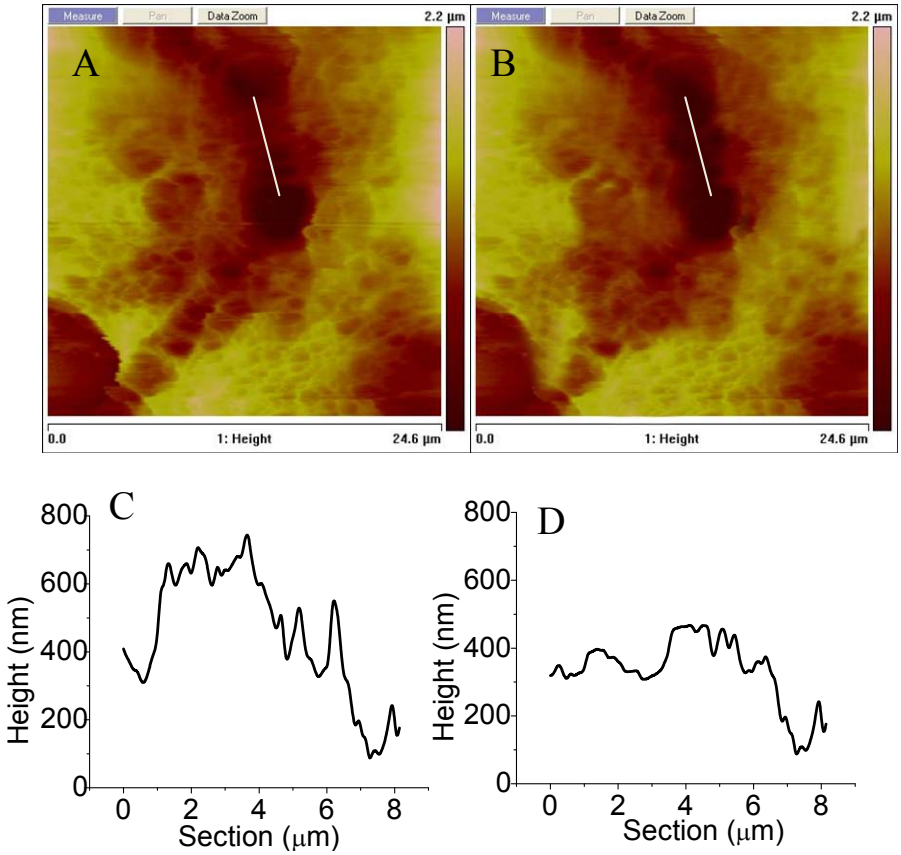

Figure 5.5 Nanodissection of intermediate filaments by AFM (before and after) with cross section to indicate the cut-off bundle

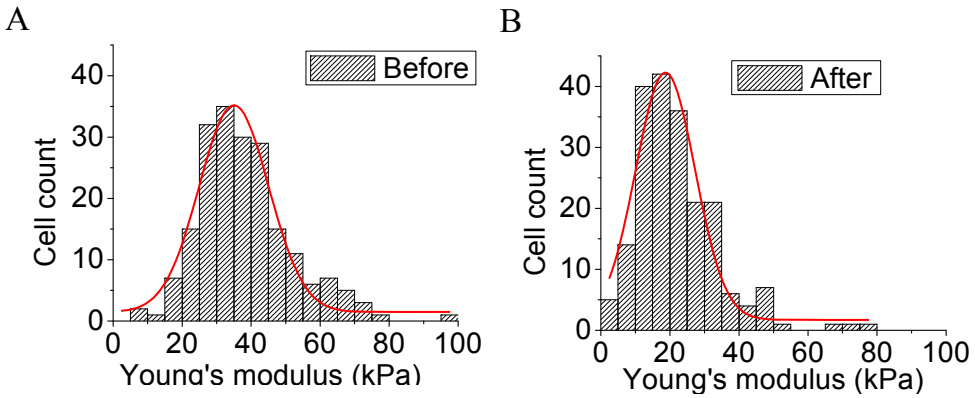

Figure 5.6 The stiffness response before and after AFM based nanodissection.

Therefore both modulations of desmosome yielded a cell sample without cell-cell adhesion, and both cases the cell display a decrease in stiffness. Thus it confirms that the loss of cell-cell

adhesion either through mechanical dissection of intermediate filament or through desmosome disassembly would result in the loss of cell stiffness. Conceptually, when cells are modeled as tensegrity prestress becomes the main characteristics that determine the stiffness of the cytoskeleton structure; and it has been well documented that cell will become stiffer when prestress increases [93, 171, 172]. Similar conditions can be drawn for the keratinocytes with their intermediate filaments damaged. Since the intermediate filaments are tensional elements in the cytoskeleton system, therefore the loss of tension due to the loss of intermediate filament based adhesions either from antibody binding, calcium depletion or mechanical dissection would lower the prestress in the tensional elements, so as the stiffness. Theoretical calculation was then performed to verify the stiffness change with and without intermediate filament in the structural model, thus to confirm if the dissection operation was successfully achieved.

5.3 Quantitative modeling based on six struts tensegrity structure

The structure model shown below with 6 struts (black) and 24 cables (blue) was originally developed by Ingber [173] as a conceptual model for cellular tensegrity (Fig. 5.7A). It is constructed by connecting the ends of compressional struts with the tensional cables. The struts mimic the role of microtubule in the cytoskeleton while the cables denote the actin filaments. Considering actin filaments normally lie beneath the cell membrane and are abundant at the cell peripheral [92], the design ensures that all the tensional cables for microfilament are at the boundary of the structure. Since in each direction, we have a symmetric structure of two struts, thus the same notation is used for both struts in each direction, as AA, BB and CC. The length of each strut is L and the distance between them is $s = L/2$. The distance between each pair of notes (cable length of AB, BC or AC)

is l.

To quantify the relationship between the stress and the strain, a signature characteristics of mechanical behavior, parallel loads are applied to both ends of the structure in one direction. A force of $\frac{T}{2}$ is applied to each node of C along the x direction to stretch the structure. At this configuration and with the applied load, we want to find out the relationship between the strain and the stress, or in other words, the modulus in the load direction.

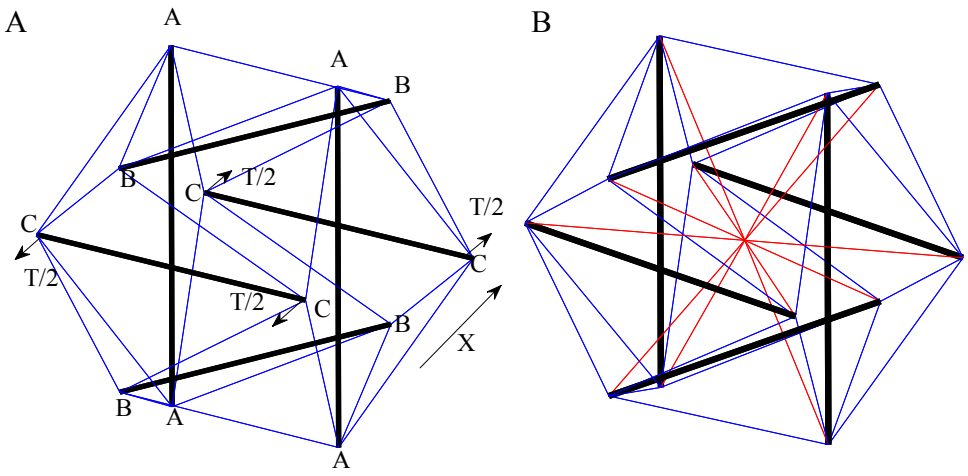

Figure 5.7 The configuration of the tensegrity structure without intermediate filaments, the black lines indicate the microtubule as the compressive elements and the blue line indicate the actin filament as the tensional elements

By virtual work method, we define that the work of T on an incremental extension δ_{s_X} per unit reference volume V of the model equals the work of uniaxial stress on the incremental change in uniaxial strain δ_{e_X}, a relationship captured in Eq. 5.1.

$$\frac{T\,\delta_{s_X}}{V} = \sigma_X\,\delta_{e_X} \tag{5.1}$$

where e_X and s_X denote the strain and extension in X direction, and σ_X denotes stress in the same direction. Since we know the dimension of the structure, we can calculate the volume (V) enclosed

by it as in Eq. 5.2:

$$V = \frac{5L^3}{16} \tag{5.2}$$

Strain is defined as the unit extension, so we have:

$$\delta_{e_X} = \frac{\delta_{s_X}}{s} \tag{5.3}$$

From Eq. 5.3 and considering the distance between the parallel struts, it follows that $\delta_{e_X} = 2\frac{\delta_{s_X}}{L}$. By substituting it and Eq. 5.3 becomes:

$$\frac{16T\,\delta_{s_X}}{5L^3} = \sigma_X \frac{2\delta_{s_X}}{L} \tag{5.4}$$

thus,

$$\sigma_X = \frac{8T}{5L^2} \tag{5.5}$$

By definition of modulus as the ratio between strain and stress in X direction:

$$E^* = \frac{d\sigma_X}{de_X} = s\frac{d\sigma_X}{ds_X} = \frac{L}{2}\frac{d\sigma_X}{ds_X} \tag{5.6}$$

Taking the derivative of Eq. 5.5, we obtain the relationship between strain and stress:

$$\frac{d\sigma_X}{ds_X} = \frac{8}{5L^2}\frac{dT}{ds_X} \tag{5.7}$$

By substituting Eq. 5.7 into Eq. 5.6, we finally arrive at the expression of modulus as:

$$E^* = \frac{L}{2}\frac{8}{5L^2}\frac{dT}{ds_X} = \frac{0.8}{L}\frac{dT}{ds_X} \tag{5.8}$$

The E^* in Eq. 5.8 is the Young's modulus obtained from the structural derivation, and it will be applied to both structure with and without intermediate filaments by plug-in the $\frac{dT}{ds_X}$ from the two structures.

5.3.1 Without intermediate filaments

From Eq. 5.8, we found the expression of E^* that is written in terms of $\frac{dT}{ds_X}$. Then the only remaining term is to find the relation between the force T and the distance between the struts s_X. For the configuration without the intermediate filaments, the calculation is as follows. The relationship between the force T and the extension is:

$$T = 2F_{AB}\frac{s_X - L_{BB}}{l_{AB}} + 2F_{AC}\frac{s_X}{l_{AC}} \tag{5.9}$$

where F_{AB} and F_AC are the forces in the corresponding cable. The kinematics of the configuration in Fig. 5.7 is:

$$\begin{aligned} l_{AB} &= \frac{1}{2}\sqrt{(L_{BB} - s_X)^2 + (s_Y)^2 + (L_{AA})^2} \\ l_{AC} &= \frac{1}{2}\sqrt{(L_{AA} - s_Z)^2 + (s_X)^2 + L_{CC}^2} \\ l_{BC} &= \frac{1}{2}\sqrt{(L_{CC} - s_Y)^2 + (s_Z)^2 + L_{BB}^2} \end{aligned} \tag{5.10}$$

If we assume that the cables are linearly elastic of stiffness k and resting length l_r. The force then in each cable is given:

$$F = \begin{cases} k(l - l_r) & \text{if } l > l_r \\ 0 & \text{if } l < l_r \end{cases} \tag{5.11}$$

By plugging the kinematics of the structure in Eq. 5.10 and the force expression in Eq. 5.11, we have the relationship between T and s_X. Taking the derivation of that, we can obtain $\frac{dT}{ds_X}$. This

derivation will be evaluated in the initial state (the reference state) where the parameters are:

$$\begin{aligned} l_{AB} = l_{AC} = l_{BC} = l_0 \\ L_{AA} = L_{BB} = L_{CC} = L_0 \\ s_X = s_Y = s_Z = \frac{L_0}{2} \\ l_0 = \sqrt{\frac{8}{3}} L_0 \end{aligned} \tag{5.12}$$

After plugging in these parameters, we obtain: $\frac{dT}{ds_X}|_0$. Plug it into Eq. 5.8, we have the definition of E^* in the configuration without the intermediate filament.

$$E^* \doteq 15.6 \frac{F}{{L_0}^2} \frac{1+4\varepsilon_0}{1+12\varepsilon_0} \tag{5.13}$$

where ε_0 is the initial cable strain, defined as $\varepsilon_0 = \frac{l-l_r}{l}$.

5.3.2 With intermediate filaments

The structures with intermediate filaments are shown in Fig. 5.7B. The red lines connecting the nodes in the middle are intermediate filaments. This structure is introduced by considering the fact in biology that the intermediate filaments are projecting from the nucleus to the peripheral of the cell [92]. Thus the designed structure has a tensional cable connecting each pair of struts and the cable all crossing the center O. With this additional structural components, the kinematics for the

actin filament remains; while the kinematics for the intermediate filament can be characterized as:

$$\begin{aligned} r_{OA} &= \frac{1}{2}\sqrt{s_x^2 + L_{AA}^2} \\ r_{OB} &= \frac{1}{2}\sqrt{s_y^2 + L_{BB}^2} \\ r_{OC} &= \frac{1}{2}\sqrt{s_z^2 + L_{CC}^2} \end{aligned} \tag{5.14}$$

With the addition of intermediate filament structures, some force balance establishment has to take into consideration the tension in the intermediate filament: forces in N_{OA}, N_{OB} and N_{OC}. The force balance now has been reconfigured and can be expressed as:

$$\begin{aligned} T &= 2(F_{AB}\frac{s_x - L_{BB}}{l_{AB}} + F_{AC}\frac{s_x}{l_{AC}} + N_{OA}\frac{s_x}{r_{OA}}) \\ F_{BC}\frac{L_{BB} - s_y}{l_{BC}} - F_{AB}\frac{s_y}{l_{AB}} - N_{OB}\frac{s_y}{r_{OB}} &= 0 \\ F_{AC}\frac{L_{AA} - s_z}{l_{AC}} - F_{BC}\frac{s_z}{l_{BC}} - N_{OC}\frac{s_z}{r_{OC}} &= 0 \end{aligned} \tag{5.15}$$

The force in each of the tensional elements including the actin filaments and the intermediate filaments can then be expressed in Hooke's law. For actin filaments, it remains the same as the previous configuration in Eq. 5.11. For intermediate filaments, a second order elastic element was added with elastic constant k_2 on the basis of a first order elastic element:

$$F = \begin{cases} k_1(r - r_r) + k_2(r - r_r)^2 & \text{if } r > r_r \\ 0 & \text{if } r < r_r \end{cases} \tag{5.16}$$

where r_r is the reference length (zero tensional force) for the intermediate filaments.

To find he relationship between the applied load T and the displacement s_X, we can plug the kinematics into the force balance in Eq. 5.15 and replace the force with the expressions in Eq. 5.16,

we would have the static balance condition with the intrinsic parameter of the components and the kinematic. With the same procedure as in the previous configuration, we can take the spatial derivative of T with respect to s_X to obtain $\frac{dT}{ds_X}$. And this derivative will be evaluated at the initial state with the following parameters:

$$\begin{aligned} l_{AB} = l_{Ac} = l_{BC} = l_0 \\ L_{AA} = L_{BB} = L_{CC} = L_0 \\ s_X = s_Y = s_Z = L_0/2 \\ l_0 = \sqrt{3/8} L_0 \end{aligned} \tag{5.17}$$

After evaluation under initial condition, the derivative $\frac{dT}{s_X}|_0$ can be plugged into Eq. 5.8 , we have E^*_{with}:

$$E^* = \frac{L}{2}\frac{8}{5L^2}\frac{dT}{ds_x} = E_{F_0} + E_{F_1} + E_{F_2} \tag{5.18}$$

where $E_{F_0} = 0.33\frac{F_0}{L_0^2}\frac{6\varepsilon_0+1}{\varepsilon_0}$ defines the contribution from the stress in the actin filament; $E_{F_1} = 0.01\frac{F_1}{L_0^2}\frac{43\varepsilon_0+2}{\varepsilon_0}$ defines the contribution from the linear portion (F_1, k_1) of the intermediate filament and $E_{F_2} = \frac{F_2}{L_0}\frac{1.6\varepsilon_0+0.3}{\varepsilon_0(\varepsilon_0+1)}$ defines contribution from the quadratic portion (F_2, k_2) of the intermediate filament. Compared with E_{F_0} and E_{F_1}, EF_2 is much smaller and therefore can be neglected. We can assume that the intermediate filament can also be modeled as a first order Hooke relation. However, E_{F_1} and E_{F_0} are comparable, and thus E_{F_1} will make a difference for the modulus with intermediate filament structure.

With the intrinsic parameters of individual filaments obtained from [173], we can calculate the Young's modulus values numerically. The parameters used in the calculation are shown in Tab. 5.1. The plotting in Fig. 5.8 shows the comparison of Young's modulus values with respect to the strain for three different situations, without intermediate filaments, with intermediate filaments

Table 5.1 Parameter list for the numerical evaluation

Variable	Physical meaning	value	unit
F_0	Average force generated by a single acto-myosin motor	1.6	nN
F_1	Average force generated by a single intermediate filament from linear portion	3.2	nN
F_1	Average force generated by a single intermediate filament from quadratic portion	0.8	nN
L_0	Estimated length of an actin filament from volume fraction	0.7	μm
K	The stiffness coefficient of an actin filament	0.05	pN/nm
k_1	The linear portion of stiffness coefficient of an intermediate filament	0.10	pN/nm
k_2	The quadratic portion of stiffness coefficient of an intermediate filament	0.25	pN/nm

only the linear portion and with intermediate filaments both linear and quadratic terms. The curve for the linear portion of intermediate filaments overlaps with the one containing both linear and quadratic portions. This also confirms that E_{F_2} is negligible. The Young's modulus with intermediate filaments in the configuration increased with 18 percent at the upper boundary when $\varepsilon_0 \to 1$. The trend is also indicative of the contribution from the intermediate filaments, that is when the strain increases, the stiffness difference is larger. This agrees well with the functional contribution of intermediate filaments in the cytoskeleton system. They are responsible for the shape maintaining when there is large strain or deformation [92].

5.4 Chapter summary

In this chapter, we validated that intercellular adhesion is part of the mechanism employed by epithelial cells to achieve force balance in a cytoskeleton based tensegrity structure. We used

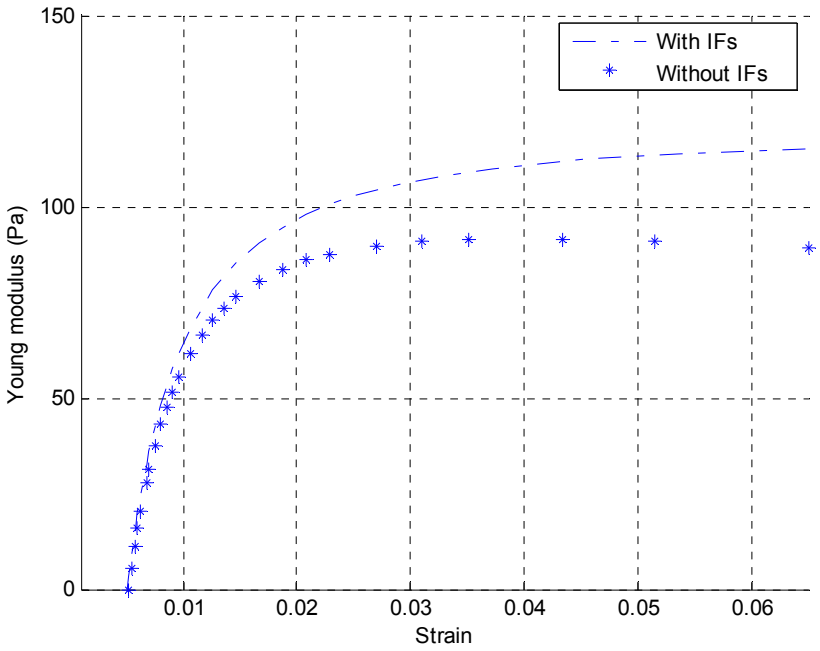

Figure 5.8 Young Modulus comparison with and without intermediate filaments from simulation based on the structure model

AFM based nanorobotics to dissect the cell-cell adhesion between keratinocyte cells, primarily the intermediate filament structures. The mechanical behavior data was subsequently obtained and a significant decrease of cellular stiffness was observed. A linkage between the integrity of cell-cell adhesion and the stiffness of the cell structure can be built. The cell adhesion loss was also induced biochemically by antibody treatment and calcium depletion which all result a disrupted desmosome structure. Both methods yield cell samples that behave similarly as when cell-cell adhesion was cut loose mechanically, and stiffness decrease was observed expectedly. The findings were then taken to test by a tensegrity structural model with and without intermediate filaments, the simulation result verifies the reduction in Young's modulus values when there is no extra tensional element provided by the intermediate filament. Thus far, the hypothesis was validated that epithelial cells employ cell-cell adhesion as a complementary mechanism to cell-ECM adhesion to sustain their mechanical integrity during cell remodeling. This research work may provide some insights in

the development of new cell growth environment by taking into consideration of cell-cell adhesion beyond cell-ECM interactions.

Chapter 6

Dynamic characterization of cell signaling pathways mechanics

6.1 Introduction

EGF is a growth factor that binds to epidermal growth factor receptor, EGFR, a cell surface receptor [174] to promote cell growth and proliferation. The ligand binding can trigger a series of downstream signaling events that regulate cell behaviors, resulting in cell proliferation, differentiation or migration. These different cell biological behaviors would result in different mechanical behaviors. The A431 human epidermoid carcinoma cell line has been widely used as a biochemical model for the investigation of signaling-pathway-related cell responses by EGF stimulation [57]. EGF treated A431 cells show significant rounding and swelling that have been reported by researchers [175]. It has long been postulated that signaling pathways could regulate the configuration of the cytoskeleton as a mechanism of facilitating the perspective cell behavior. For instance, cancer cell would display loose attachment, i.e. cell adhesion, to make way for metastasis [76]; migration cells would have stronger cell adhesion in the filopodia, the leading edges of migration direction than in the trailing edges [176]. The configuration of cytoskeleton thus will determine the overall structure of the cell body; and one can use the cytoskeleton configuration to reveal the biological behavior of living cells after certain biochemical cues. Since the cytoskeleton is deemed as the main force bearer of the whole cell [85, 163], it can then be probed by mechanical force; the

mechanical response from the cell, or cytoskeleton would provide abundant information about its mechanical status. We normally refer these information as biomechanical makers. Nanomechanical sensors are normally utilized to perform the force loading and measurement; the measurement result would yield unique insight about the cell behavior and cell signaling pathways.

The imaging modality is based on force interactions at the molecular level between a cantilever with a sharp tip attached at the free end and the sample beneath it. The force interaction is mainly determined by the distance between the two, thus by controlling a constant interaction force, one can build a topography map of the sample by raster scanning its entire surface. The nature of the measurement process and its ability of working in liquid environment make AFM an ideal tool for visualization of cellular and molecular structures *in situ*. Meanwhile, the probing interaction would also provide the mechanical property of the cell samples [177]. We have observed ultra-structural changes in real time at nanometer scale in cellular adhesions on keratinocyte cells [10]. Others have also reported results from AFM imaging about cellular structural observation, either on animal cell lines or bacteria cells [1]. Cellular elasticity can be measured by recording the force displacement curves through AFM nanoindentation. Its effectiveness as biomarkers for physiological conditions has been validated previously [178]. Cellular viscoelasticity can be obtained by fitting AFM force displacement curves with Johnson-Kendall-Roberts (JKR) dynamic model [179].

QCM-D is another nanomechanical senor that could measure interactions at the molecular level [47]. It has been used for molecular recognitions, such as membrane formations [48], protein adsorptions [49], and cell spreading [50]. It operates at thickness-shear mode by oscillating a quartz crystal disk with high frequency (normally 5 MHz) and low amplitude (less than 1 nm in lateral direction). It collects the frequency and amplitude changes of the quartz crystal and reveals the mechanical/structural status of the sample attached on top of the sensor disk: the shift in resonance frequency indicates the mass absorption or loss; while the energy dissipation alteration

could be used to derive the viscoelasticity property of the adsorbed film on the disk [51, 52].

The combination of AFM and QCM-D for biological investigations has been achieved by previous works [180, 181]. Functionally, QCM-D measures viscoelastic property change of biological matters at different physiological conditions. The mechanical information can be verified by probing the sample surface topography using AFM under. This combination has been demonstrated in the study by [180] where the effect of different substrates on cell shape and cell mechanics were investigated. The topography and mechanical property of the cells are obtained by AFM imaging and force measurement, and at the same time QCM-D characterizes the adhesion between the cells and the substrates through the frequency and dissipation monitoring. Instrumentation of AFM combined with QCM-D substrate has been developed by [181]. The system was equipped with an oscillating quartz crystal as the substrate for AFM experiment. Therefore the AFM imaging and QCM-D recording can be performed simultaneously on the same sample. However, the attention for comparative characterization of cellular viscoelasticity by AFM and QCM-D has been lacking. It has been shown that both AFM and QCM-D have the capability for viscoelasticity measurement. While AFM scans and deforms cells from the top, QCM-D measures the sensor oscillation from the bottom where cell adhesion with the substrate dominates the acoustic wave decay. AFM performs cellular investigations in the fashion of single cell analysis, and QCM-D studies the property of a small population, a single cell layer spreading on the quartz crystal. In all these aspects, AFM and QCM-D can verify and complement each other.

6.1.1 AFM energy dissipation and hysteresivity measurements

The nanoindentation process by AFM consists the loading and unloading of the vertical force exerted by the cantilever as shown in Fig. 6.1. The vertical piezo firstly drives the cantilever towards the cell sample and deforms it ($P_1 \rightarrow P_2 \rightarrow P_3$); then it retracts back to the original height

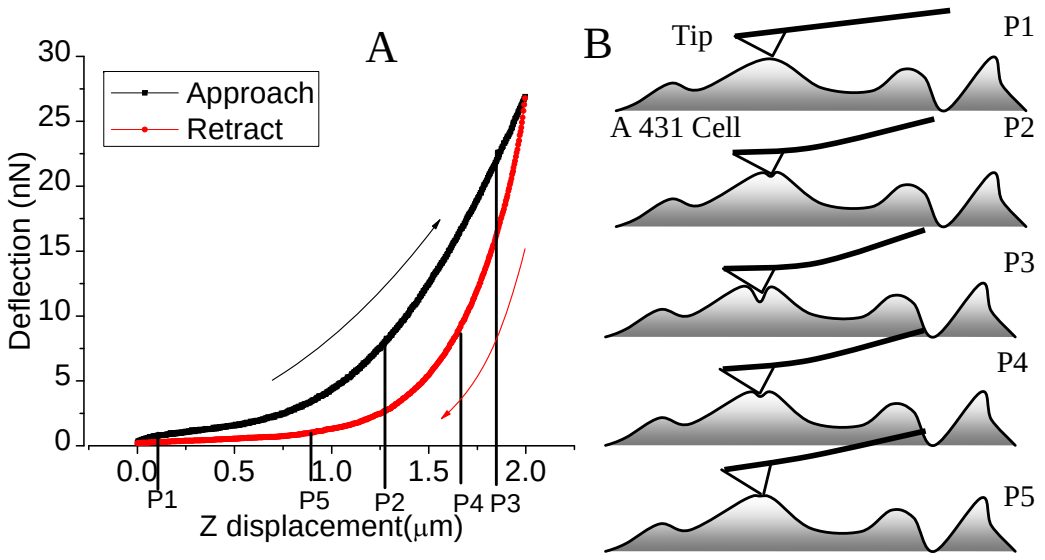

Figure 6.1 AFM energy dissipation

($P_3 \rightarrow P_4 \rightarrow P_5$). During the process, cantilever deflection will be picked up by position sensitive device (PSD) to generate the applied forces at each location, and this recorded relationship is the force-displacement curve. For each cycle, forces in the approach curve at each displacement position is always larger than those in the retraction curve. This hysteresis in applied force over the displacement defines the energy loss for the loading/unloading process. The energy required to deform the cell surface at a nominal distance on loading is not entirely recovered from the cell in withdrawing the same distance during unloading. If we define the energy under the approaching curve as A, and the energy under the retraction curve as R, the area of the hysteresis loop $(A-R)$ therefore depicts the amount of energy dissipated during each cycle. Furthermore, we can define $\zeta = \frac{A-R}{A}$ as the hysteresivity, a characteristics and measure of the viscosity property [182]. This viscoelastic index ζ indicates the viscoelastic property of a material, with $\zeta = 0 (A = R)$ indicating pure elastic material and $\zeta = 1 (R = 0)$ pure plastic material. Normal material will have a ζ value $0 < \zeta < 1$ showing both viscous and elastic properties [183].

6.1.2 QCM-D energy dissipation measurement

QCM uses a quartz crystal as an oscillator, and an alternating electrical field will generate a shear deformation of the surface, as shown in Fig. 6.2A and 6.2B. The upper and lower surfaces will move in parallel but opposite directions laterally, generating an acoustic wave that will propagate in the direction perpendicular to the sensor disk surface. The acoustic wave has a frequency of $f = nv/(2t_q)$, where f is the resonant frequency, n is the overtone number and t_q is the thickness of the crystal. For the QCM working in gaseous condition, since the oscillation decays negligibly, the Sauerbrey relationship defines the linear relationship between the mass change and the frequency shift as [47]:

$$\Delta m = -\frac{C}{n}\Delta f \tag{6.1}$$

where $C = t_q \rho_q / f_0$, and ρ_q is the density of the crystal.

However, when the sensor is immersed in liquid as shown in Fig. 6.2C, the acoustic wave will propagate through the liquid and the oscillation amplitude will decay exponentially over time. The measurement circuit would periodically switch on and off the power input, the free decay of oscillation can be obtained by recording the output voltage [47]. The voltage decay can be fitted by:

$$A = A_0 e^{t/\tau} \sin(2\pi f t + \alpha) \tag{6.2}$$

The obtained parameters τ and f can then be used to evaluate the energy dissipation factor:

$$D = \frac{1}{\pi f \tau} \tag{6.3}$$

which can also be considered as energy loss ratio - loss energy over stored energy. It is related to the viscoelasticity of the material on top of the sensor disk [184]. Several mechanical models

have been proposed to relate the viscosity and elasticity of the film with the measured D value. Voinova and coworkers have developed a continuum mechanics model considering the oscillation wave propagating through a viscoelastic material. The material was immersed in a Newtonian fluid with either known or unknown properties [51]. The model will produce the relationship of ΔD and Δf with the material properties on the top.

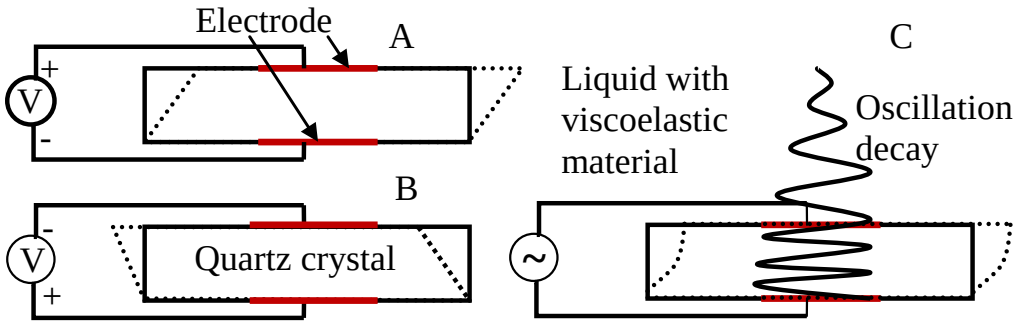

Figure 6.2 Schematic of QCM-D principle

In this work, we apply AFM probing and the QCM-D observations on the same set of cellular signaling process induced by EGF stimulation. Both experiments monitor a monolayer of A431 cells that grow on a substrate (glass substrate for AFM and quartz crystal surface for QCM-D) which will be stimulated by EGF. Whist QCM-D monitors the basal area of the cell layer close to the quartz crystal surface, where cell adhesion dominates; AFM will probe the apical surface of a single cell away from the substrate reveling cytoplasm behavior.

By analyzing and comparing the quantitative data from both techniques, the viscoelastic behavior of the cell with a more complete profile can be obtained. Once the mechanical profile is obtained from both readings, a model of the signaling pathway dynamics following the EGF simulation could be built by considering the cell mechanical structure as the plant, which makes the readings as output of the system, and the signaling pathway as the controller. We can address the signaling events from the systematic control perspective and identify the pathway related dynamics

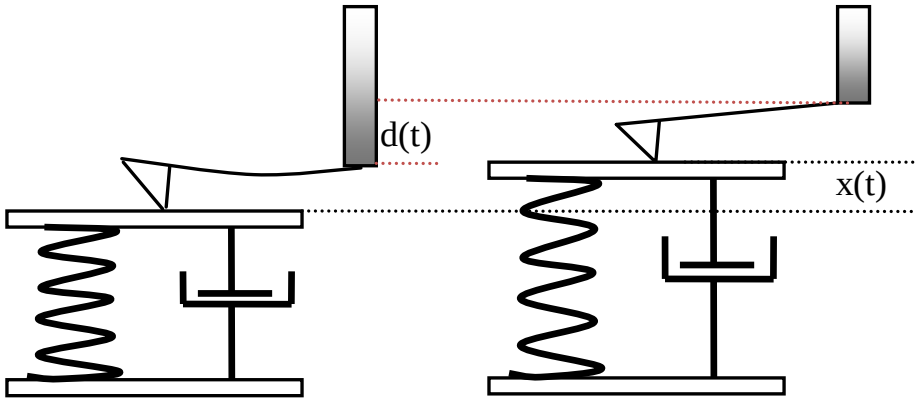

Figure 6.3 The modeling of viscoelastic material under AFM based force displacement measurement during the retract process

model structures and parameters.

6.2 Model development

6.2.1 AFM viscoelastic characterization

The following assumption was made for the force displacement based viscoelastic modeling: the cellular material is modeled as a Voigt element, a parallel configuration of spring (k) and dashpot (η) and there is only repulsive force between the AFM tip and the cell. Then we define the vertical displacement of the Z piezo as d and the deformation of the cell surface as x (Fig. 6.3). The spring constant of the cantilever is defined as k_c and its deflection is d_c.

For the retraction process, based on the Voigt element configuration, the dynamic force balance can be defined as:

$$F = k(x_m - x) + \eta\dot{x} \tag{6.4}$$

where x_m, a constant, is the maximum vertical deformation of the cellular body from the approach process and x, a function of t, is the vertical contact point elevation due to the release of the can-

tilever pressure in the withdraw process. The force can also be calculated by cantilever deflection as:

$$F = k_c(d_{cm} - \Delta d_c) \tag{6.5}$$

where d_{cm} is the maximum cantilever deflection resulted from approach process and Δd_c is the release of deflection and is defined as the difference between the distance of retraction from the piezo (d) and the cell deformation recovery (x)

$$\Delta d_c = d - x \tag{6.6}$$

Thus plug Eq. 6.5 and 6.6 into Eq. 6.4, and $d = vt$, where v is the velocity of the Z piezo motion. We have:

$$\eta\dot{x} - (k_c + k)x = f_0 - k_c vt \tag{6.7}$$

where $f_0 = k_c d_{cm} - kx_m$ is a constant resulted from the approach process. The solution to the ordinary differential Eq. 6.7 can be used to evaluate deformation recovery x under different influence of η.

6.2.2 QCM-D based cell membrane peeling model

The sensor disk motion poses the relative motion of the cell with regard to the fluid in the sensor chamber. The effect is similar with the cell under liquid shear flow. In the leading edge, the adhesion bonds between integrin receptors and the substrate ligands will be ruptured due to the flow resulted cell strain; while at the other edge, there will be bond formation activities attributed to the increased integrin and ligand affinity as shown in Fig. 6.4. The model in Fig. 6.4B describes this peeling of focal adhesion between the cell and the substrate due to shear stress under liquid

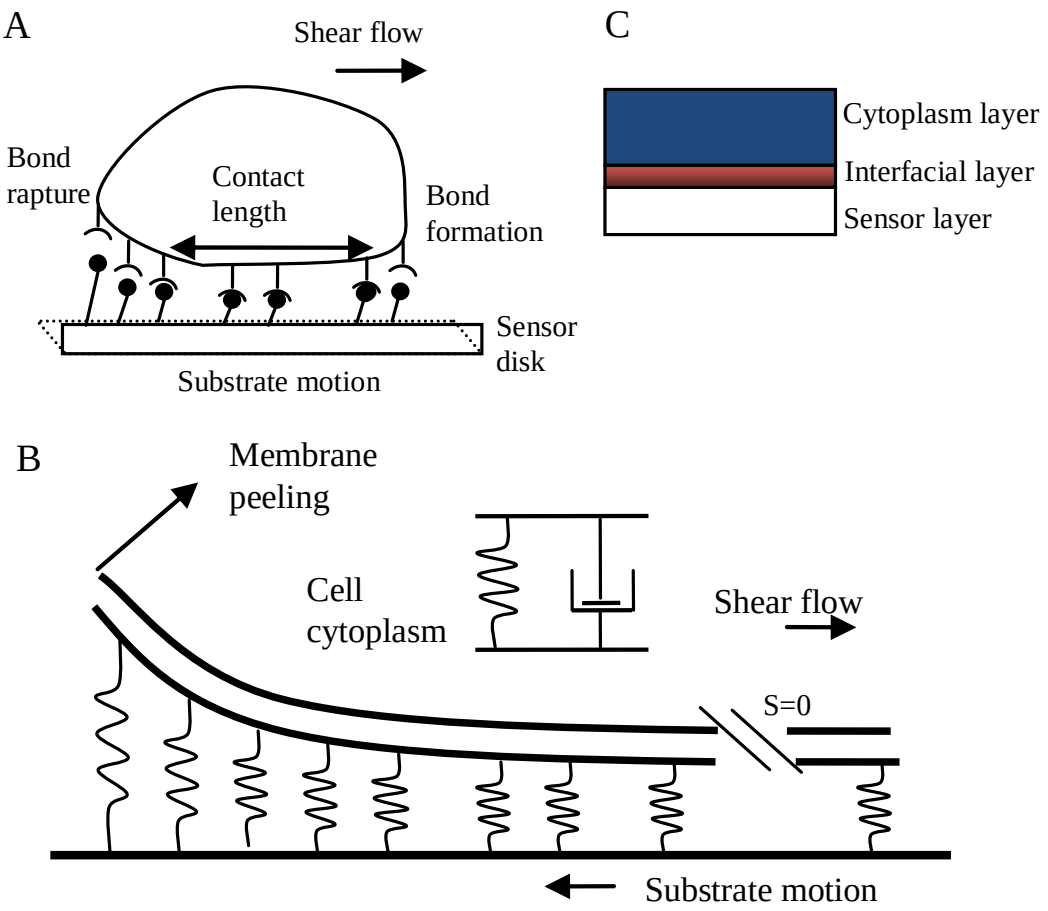

Figure 6.4 Cell membrane peeling model at the basal area (A, B); and the cell model as a whole (C) in which the cytoplasm was modeled as a Voigt element.

flow. In the 2D model, focal adhesion sites are characterized by the contact length L_c between the cell and the substrate. The substrate moves with speed v_s and the peeling speed is proportional to it as $v_p = \kappa v_s$, where κ is the coefficient. The focal adhesion is modeled as a spring with coefficient of k_a, whereas the single focal adhesion bond strength is $f_a = k_a(l - \lambda)$, where l and λ are the lengths of the bond in the stretched and unstretched states. The total focal adhesion strength then becomes $F_a = N_a k_a(l - \lambda)$, where N_a is the adhesion bond density. The adhesion kinetic equation specifies the balance for the formation and dissociation of adhesion bonds which determines the

temporal- and spatial-dependent bond density $N_a(t,s)$ [185] [61]:

$$\frac{\partial N_a}{\partial t} = v_p \frac{\partial N_a}{\partial s} + k_f(N_l^0 - N_a)(N_r^0 - N_a) - k_r N_a \tag{6.8}$$

$$k_f = k_f^0 \exp \frac{k_{ts}(l-\lambda)^2}{2k_b T} \tag{6.9}$$

$$k_r = k_r^0 \exp \frac{k_f - k_{ts}(l-\lambda)^2}{2k_b T} \tag{6.10}$$

where N_l^0 is the ligand density on the substrate; N_r^0 is the cell surface receptor density; k_f is the bond formation rate with initial value of k_f^0; k_r is the bond formation rate with initial value k_r^0; k_{ts} is the transient elastic constant of the adhesion bond and it is reasonable to assume that $k_{ts} < k_a$ for this model; k_b is the Boltzmann constant, and T is the temperature. For energy dissipation rate calculations, we have $\frac{\partial N_a}{\partial t} = 0$, and Eqs. 6.8 to 6.10 will be evaluated numerically by fourth order Runge-Kutta method with the initial value N_a^0 solved by:

$$0 = k_f(N_l^0 - N_a)(N_r^0 - N_a) - k_r N_a \tag{6.11}$$

The total energy dissipation rate for the focal adhesion dissociation can be defined as:

$$\dot{E}_a = w_c \int_0^{L_c} F_a v_p \frac{\partial l}{\partial s} \, \mathrm{d}x \tag{6.12}$$

where w_c is the effective width of the contact area.

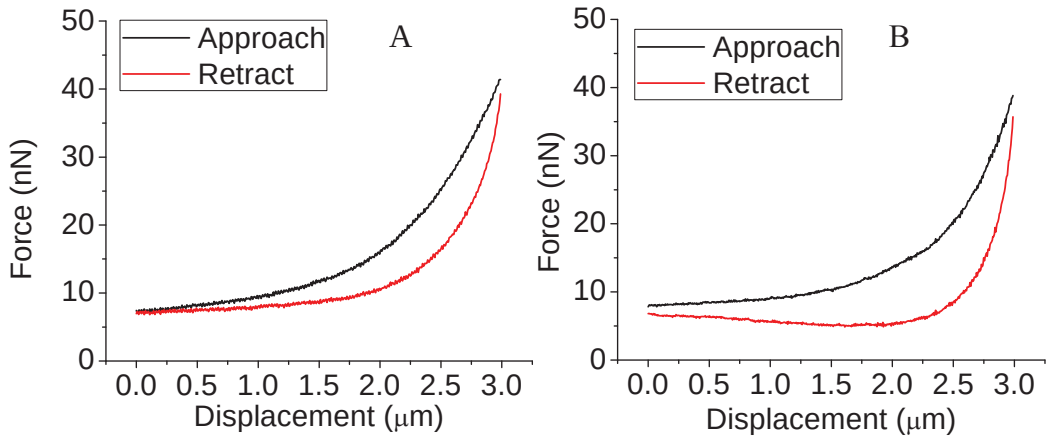

Figure 6.5 AFM energy dissipation measurement on a single cell with and without EGF treatment

6.3 Results and Discussion

The AFM measurement result before and after the stimulation with EGF are shown in Fig. 6.5 A and B. The displacement was controlled below 2 μm and the resulted loading force is within 30 nN, with the induced maximum cell deformation less than 500 nM ($<$ 25% of cell height). These parameters will be used throughout the force measurement process. The hysteresis area between the loading and unloading force curve ($A - R$), is increased from 3.2 to 6.9 femto-Joules (fJ) due to the stimulation, a 126 percent jump.

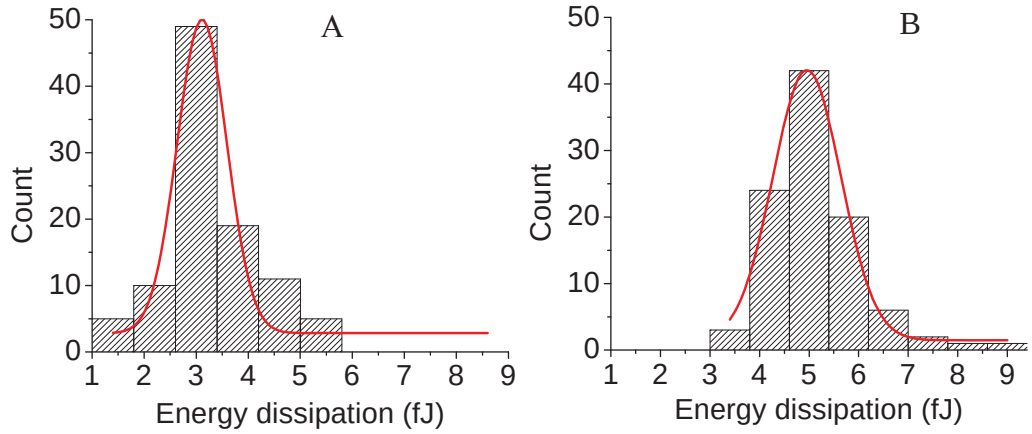

Figure 6.6 AFM energy dissipation measurement on 100 different cells before and after EGF treatment.

A statistical analysis was performed on a population of cells before and after EGF stimulation. The result is shown in Fig. 6.6A and B. The cell sample was first measured under AFM on 100 randomly selected cells. EGF was then applied to the petri dish where the cell sample sits with final concentration of 40 nM. The sample was then incubated for 30 min till another AFM measurement on 100 randomly selected cells. The result was plotted with normal distribution for energy dissipation before and after EGF addition. It can be observed that energy dissipation increased from 3.26 $\pm$ 0.95 fJ to 5.16 $\pm$ 0.89 fJ (Mean $\pm$ SD). This demonstrates the cells display a different mechanical property after EGF stimulation.

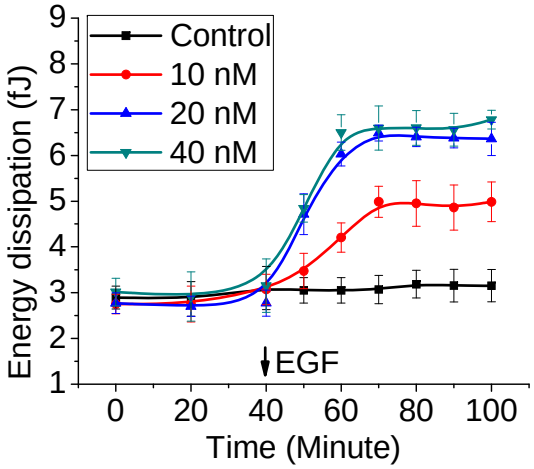

Figure 6.7 Dynamic mechanical responses (Energy dissipation) of A431 cells to stimulations with four different concentrations of EGF: 0, 10 nM, 20 nM, and 40 nM

This is a general trend on the cell population, and then we want to define how cells dynamically adjust their cytoskeleton structure throughout the stimulation process. We then monitor the stimulation process dynamically in real time. After the EGF stimulation, force displacement curves were taken at a 1Hz frequency. Fig. 6.7 summarizes the dynamic response of the cells after EGF treatment. Three different EGF concentrations were tested with 10 nM, 20 nM and 40 nM. The same volume of buffer solution was added in a separated experiment as control. The baseline measurement was longer at 40 min before EGF or control buffer was added. For all the three

dosages, a few minutes after the administration of EGF, there is an increase in energy dissipation, suggesting the effect of EGF is immediate; this increase continues until around 20 min when the response starts to level off. At the end of the observation, the energy dissipation is two fold the amount of baseline value. The experiment result also shows that energy dissipation increased with dosage dependent by comparing the three dosages. Larger energy dissipation was observed on 20 nM and 40 nM EGF experiments than 10 nM EGF. The 40 nM dose has a slightly large increase than 20 nM, although the difference is small (Fig. 6.7). Similar dynamics was observed for the hysteresivity measurement (Fig. 6.8).

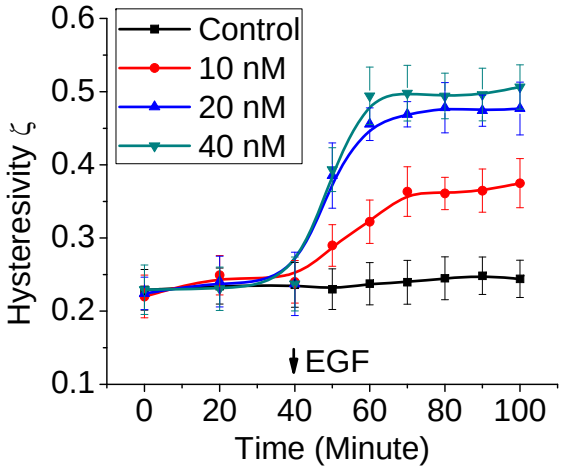

Figure 6.8 Dynamic mechanical responses (Hysteresivity) of A431 cells to stimulations with four different concentrations of EGF: 0, 10 nM, 20 nM, and 40 nM

The QCM-D experiment results for a continuous monitoring of 100 min after stimulation of EGF of dosage variation confirmed that the energy dissipation decreased over time. After stimulation with EGF of different concentrations, the dissipation decrease is clearly dosage-dependent. Immediately after stimulation, the dissipation shows a sharp increase, then after about half hour it drops down. The initial sharp increase of dissipation is caused by the liquid flush during the change of EGF containing medium. Overall the energy dissipation is decreased due to the stimulation. Fig. 6.9 shows representative dose-dependent and time-dependent changes in ΔD, of the

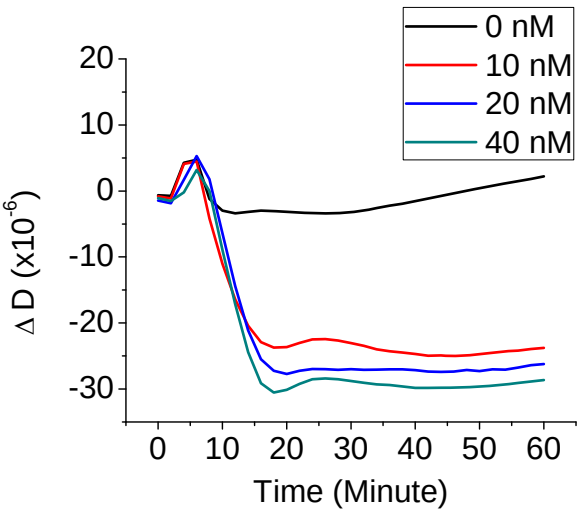

Figure 6.9 QCM-D measurement of energy dissipation over time after EGF treatment with concentration of 0 nM, 10 nM, 20 nM and 40 nM

monolayer of A431 cells in response to EGF. Unlike the AFM results shown in Fig. 6.7 and 6.8, where ζ increased with time and with dose, the QCM-D detected a decrease in ΔD with time and with dose. As a mechanical property, the change in energy dissipation factor ΔD measured directly by the QCM-D is analogous to hysteresivity, ζ, computed from the AFM measurements, where both quantities correspond to the mechanical energy loss relative to the energy input per measurement cycle. However, the two techniques probe different regions of the deposited cells; the AFM tip probes 500 nm into the cell from its top surface while the QCM-D senses approximately 100 nm into the basal area up from the bottom surface of the sensor crystal.

Interestingly, responses in D and ζ reached their plateaus within a similar time frame after the addition of the EGF (40-50 minutes for the decrease in ΔD and 50 minutes for the increase in ζ). Both changes showed signs of saturation in a similar dose range (responses at 20 nM and 40 nM at very similar levels). These similarities indicate that both mechanical responses (D and ζ) that were developed locally might be synchronously mediated by the same globe cell signaling pathway(s).

For pure elastic materials, there will be no energy dissipation. Accordingly, when an AFM

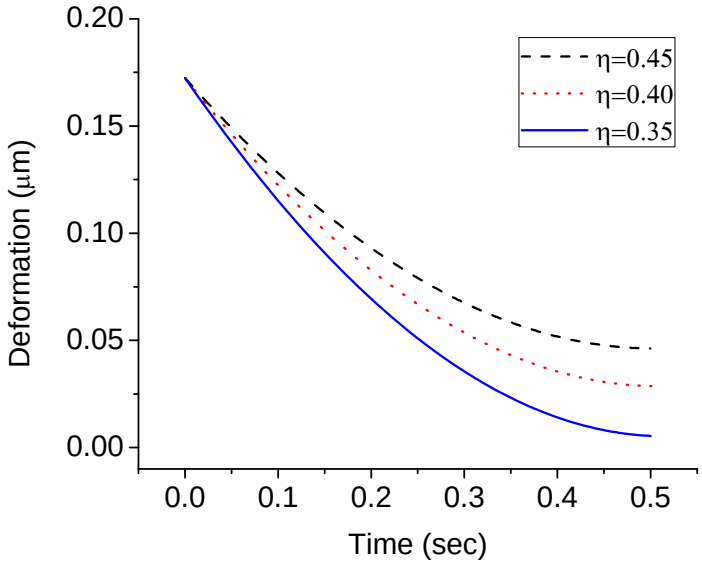

Figure 6.10 AFM energy dissipation simulation result shows that it takes longer time for the deformation to recover for a cell with higher viscosity η as indicated with $\eta = 0.45$ showing larger deformation overall.

force measurement is performed on it, the approach and retract portions of the force displacement curve would overlap. However, for biological samples, viscosity is inherent and researches have shown that cellular components inside are mostly viscoelastic such as the cytoplasm fluid, even cytoskeleton [186]. Therefore, normal force curves on biological samples in liquid display large hysteresis between the approach and the retract curves.

The hysteresis between loading and unloading force curves indicates that the repulsive force at each displacement position in unloading is lower than in loading. The origin of the decreased repulsion on the unloading curve is that at any given nominal displacement the actual local separation is larger on retraction than on approach, because it takes a finite time for the deformed cell surfaces to relax and to recover to its original shape. According to the modeling of force displacement process as described in the previous section, the deformation relaxation process can be plotted in Fig. 6.10. At the given deformation $x_m = 170$ nm, the increase of viscous factor η (from 0.35 to 0.45) will result in the increased relaxation time. In other words, it takes longer time for

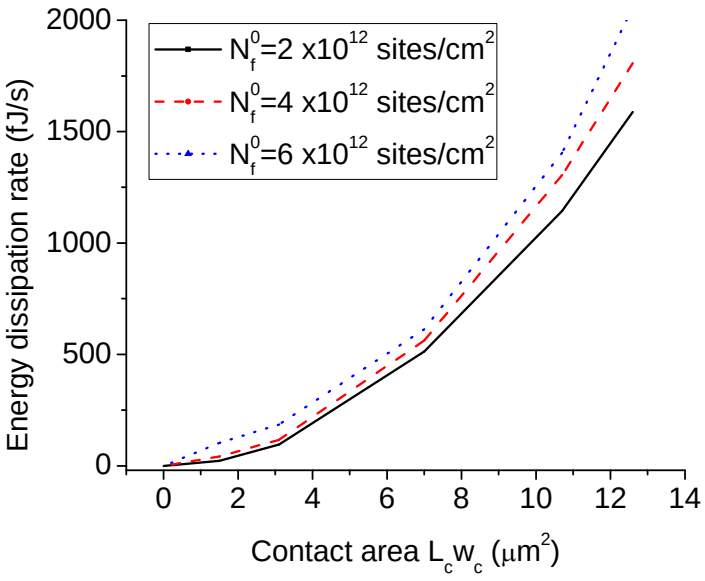

Figure 6.11 Cell peeling model simulation

a cell with higher viscosity to recover its deformation, meaning at any given displacement, there will be smaller repulsive force, resulting in a larger hysteresivity (ζ) and larger energy dissipation ($A-R$). This means the cellular body would display increased viscous characteristics to have increased energy dissipation after EGF stimulation.

For QCM-D measurement, energy dissipation measurement from QCM-D is the sum of the energy dissipated in disruption of cellular adhesion E_a and the energy loss in the viscoelastic cytoplasm E_c:$E = E_a + E_c$. The EGF reduces the focal adhesion area and strength in A431 cells [175, 187], which results in the decrease in E_a as confirmed by the adhesion peeling model described in previous section. The simulation result in Fig. 6.11 shows that the decrease in contact area A (X axis) as well as the reduced substrate adhesion ligand density (from 6×10^{12} to 2×10^{12} site/cm^2) will reduce the energy dissipation rate $\dot{E}_a$ (Y axis). On the other hand, the loss of focal adhesion will cause the cell rounding and swelling [175]. Our AFM nanoindentation measurements revealed that the cell body becomes more viscous after EGF stimulation. The increase in viscosity η in cell cytoplasm would induce relative high damping thus increase the cytoplasm en-

ergy loss during QCM-D measurement [47]. However, the QCM-D measured energy dissipation E decreases after EGF treatment, indicating that E_a dominates the energy dissipation process and E_c has minimal effect. The modeling of the wave propagation through the cellular material therefore should employ the multilayer configuration (Fig. 6.4C). Cellular adhesion through focal adhesion complex linking cytoskeleton with ECM creates an interfacial layer between the cell membrane and the ECM with gap thickness ranging from 30 nm in closest contact area to 100-250 nm in the rest areas [165, 188, 189].

Evidence shows that the acoustic wave decays almost completely before reaching the cell cytoplasm [189], rendering the energy dissipation in cellular adhesion become the primary energy loss mechanism during the QCM-D measurement, which agrees with our experimental findings. Therefore the characterization process benefits from the difference in measurement mechanisms of the two instruments. AFM performs nanoindentation on cell membranes with less than 500 nm deformation in a single-cell analysis fashion reveling cell cytoplasm properties, while QCM-D monitors the cell-ECM interfacial layer where focal adhesion dominates the energy dissipation. Therefore, AFM and QCM-D work in a complemented manner in the characterization of the viscoelastic property changes.

6.4 Chapter summary

Cell signaling is one of the fundamental processes that control the cell fate. It regulates the cell shape, and through which cell mechanics. To identify the dynamic signaling pathway *in situ*, instruments and techniques that are capable of monitoring the real-time mechanical property changes (such as viscoelasticity) as well as structural rearrangements are crucial. AFM has been proved to be an effective instrument to visualize cell membrane and cytoskeleton structures. It can also

provide the mechanical information with high temporal and spatial resolution. Meanwhile, the viscoelasticity change can also be measured as the change of energy dissipation of a cell monolayer by means of QCM-D. Our study pioneered a novel approach where AFM and QCM-D can work in complemented fashion for the characterization of cellular viscoelastic properties during signaling induced cell cytoskeleton remodeling and thus facilitate the investigation of structural and mechanical biomarkers in cellular signaling processes. These mechanical readings will provide us more insight into the dynamics of the cell signaling.

Chapter 7

Plant model derivation

7.1 Introduction

The QCM-D is a mechanical sensor that measures near surface changes by recording the mechanical oscillation of a quartz crystal. The shear mode oscillation is generated by applying an alternating voltage to a thin AT-cut quartz crystal sandwiched between a pair of electrodes. The piezoelectric property of the quartz crystal enables the fine displacement difference between electrodes, thus a high frequency shear-stress at the measuring surface. Because of the fine displacement in nanometer scale and the ultra-high oscillation frequency commonly at 5MHz in resonance, high sensitivity to the changes on the crystal surface can be achieved. It has garnered attentions from different fields ranging from monitoring chemical depositions [190] to detecting protein absorptions [191] and nucleic acid hybridizations [192]. Recently it has been used in probing the interactions between the cell and the sensor disk as a culture substrate, making it a regular cell adhesion assay of label-free manners [193–195].

When animal cells cultured on the sensor disk, the QCM-D device can detect the subtle changes to the cell adhesion, i.e. cytoskeleton and focal adhesions under different physiological/pathological conditions [196,197]. Specifically, it has been demonstrated by measurements of frequency changes, the attachment and spreading of initially suspended cells can be monitored in real time [189, 198, 199]. We have previously characterized cell adhesion change following EGF treatment by energy dissipation factor recordings [67, 68, 200]. The measurement and interpretation of energy dissi-

pation factor as an effective marker for cell adhesion has received ever increasing attention, as mechanical force in this case plays an important role in various cellular processes. The mechanical interaction at the protein/sensor disk interface contains valuable information strongly and uniquely linked to focal adhesion. To characterize the related cell property requires extracting these information from the measurement data, thus a physical model that describes the experimental condition, in this case a quartz crystal sensor in shear mode oscillation, emphasizes the role of mechanical interaction and contains cellular properties as model parameters needs to be established [189].

Most of the models to date have been based on the equivalent circuit and impedance analysis method [189, 201]. By constructing an equivalent circuit to model the electrical characteristics of a quartz crystal resonator in contact with a viscoelastic material, the recorded impedance data can then be analyzed to obtain the viscoelastic property change of the material, i.e. the cultured cell. A commonly accepted model developed by Voinova and coworkers [51] took a continuum mechanics approach and modeled the mechanical wave generated by the sensor oscillation propagating through a viscoelastic material covered by a Newtonian fluid. By setting up appropriate boundary conditions, the change of frequency and energy dissipation factor can be expressed in terms of the physical properties of the viscoelastic thin film and the fluid. These modeling approaches along with others reviewed by Johannsmann [202], though popular and easy to use, treat the cells as a uniform material and neglect the composite nature of the cell structure. In fact, more evidence is pointing towards the focal adhesion complex as one of the main units that physically interact with the sensor disk during the oscillation; there exists coupled multi-dimensional energy dissipation sources at the fluid-solid interface. The models mentioned failed to take into consideration of the physical interactions that governs these energy dissipative processes.

Thus a mechanical model that uses the mechanical oscillation as the measurement energy source and physically mimics the cell/substrate interaction in detailed fashion down to the molec-

ular level is better positioned to meet the demand. Considering the strong correlation between the focal adhesion and the energy dissipation factor [68, 203], we believe the frictional bond slip between the integrin and ECM, the viscous damping between basal membrane and the trapping liquid between the basal membrane and the substrate, as well as the frictional slip between the focal adhesion complex and the stress fiber, plus the stress fiber and the cytoplasm are all sources of energy dissipation, and they contribute in different manner and magnitude during each measurement cycle. Thus we propose a mechanical model based on the dynamics of the oscillation sensor disk as well as the kinetics of the focal adhesion and stress fiber under the experimental conditions. The model will consider these energy dissipative mechanisms and quantify their contributions, and ultimately serve as an analytical tool for QCM-D related cell adhesion assays.

7.2 Model development

The oscillation of the sensor disk experiences the friction from the attached cell and the fluid which dissipates the kinetic energy and slows down the movement. Modern tribology considers friction at the macroscopic level originating from the formation and rupture of molecular bonds [204, 205]. Filippov and coworkers presented a simple model containing two plates with relative motion connected by molecular bonds to address the frictional energy dissipation through bond rupture and viscous component [206]. The energy dissipation through the viscous damping at the liquid-solid interface can be easily comprehended [207, 208]; while the model dealt mainly with the energy dissipative process through the molecular bond stick-slip motion [209]. Mechanical forces exerted from the oscillation break the energy equilibrium of bond formation/dissociation. The bond length and unbinding probability becomes dependent or a function of the applied force; thus it lowers the barrier height of the unbinding process and elevated the dissociation probability and ultimately

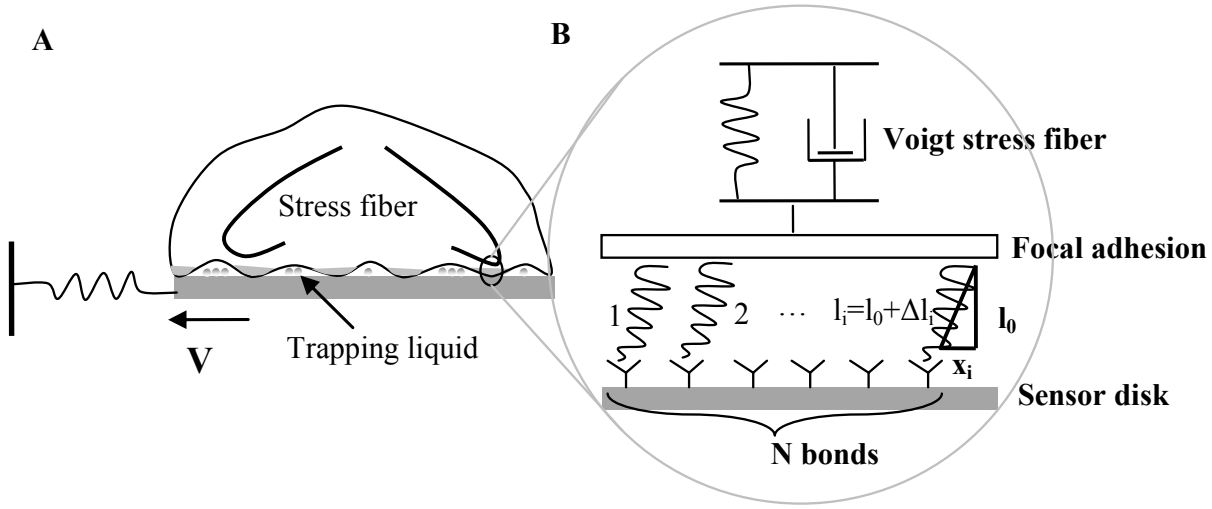

Figure 7.1 The QCM-D/cell focal adhesion energy dissipation model

dissipates the kinetic energy [210]. This was described by Bell's model of bond kinetics under mechanics influences [60, 211]. Base on friction model and combined with the Bell's model of molecular bond kinetics, we designed a mechanical model to mimic the QCM-D measurement of cell adhesion. The model considers the sensor disk interacts with the cell through the focal adhesion complex with molecular bonds.

7.2.1 The dynamics model for the sensor disk

The proposed mechanical model treat the quartz crystal as a harmonic oscillator [190] and the oscillation is maintained by a spring (K) shown in Fig. 7.1A. The sensor disk anchored on the spring will have an initial displacement as the energy input. The physical interaction between the sensor disk and the cell is characterized by the molecular bond forces (F_b) at the interfacial layer denoting the integrin-ECM adhesion, plus the viscous damping (η_l) from the liquid trapped in between the basal membrane and the sensor disk. Thus the dynamics of the disk oscillation can be defined:

$$M\ddot{X} + \eta_l \dot{X} + F_b + K(X + L_{s0} - Lsr) = 0 \tag{7.1}$$

where M is the mass of the disk and η_l is the viscous damping coefficient; X is the index of the disk horizontal motion; K is the spring constant; L_{so} and L_{sr} are the initial and rest length of the spring. Therefore, $\eta\dot{X}$ represents damping from the intrinsic decay and by the trapping fluid and the interactive bond force is defined by F_b. $K(X + L_{s0} - Lsr)$ is the force in the spring and $M\ddot{X}$ is the force resulting from the acceleration of the sensor disk. The adhesion bond force F_b will be derived in the next section.

Apparently, without the friction between the cell and the sensor disk caused by the relative movement between the two or the intracellular fluid viscous damping, the sensor disk would be in the oscillation motion at all time. With the friction in mind, we have the energy loss of the sensor disk that was captured in energy dissipation factor(D), which is defined as the ratio between the input energy and the output energy:

$$D = \frac{1}{2\pi}\frac{D_{in} - D_{out}}{D_{in}} \tag{7.2}$$

The input energy is the initial kinetic energy of the sensor disk defined as: $D_{in} = \frac{1}{2}MV_0^2$; while the output energy is the current kinetic energy of the sensor disk defined as: $D_{out} = \frac{1}{2}M\dot{X}^2$. Eq. 7.2 defines the total energy dissipation factor during a given time period; it will be used to evaluate different energy dissipation channels and to compare with the experimental data from the QCM-D measurement.

7.2.2 The mechanical model of cell adhesion

The focal adhesion is characterized as the total effect of the molecular bonds. Each molecular bond is defined as a single spring connecting the cell and the moving disk [206] as shown in Fig. 7.1B, and it has two states: a closed state indicating an intact bond that enables the connection while

an open state meaning the bond is ruptured and the connection is lost. The adhesion force of the bonds in the lateral direction thus is defined as the sum of forces in each individual bond based on the assumption that all the bonds are uniformly distributed and contribute to the total force equally:

$$F_b = \sum_{i=1}^{N} q_i f_i^x \tag{7.3}$$

where F_b is the total force, i is the bond index and N is the number of bonds in the focal adhesion complex, f_i^x is the force in the ith bond projected in the X direction, q_i is the state of the bond with Eq. 7.3 will be evaluated based on the status of each bond and be used to update F_b in the master equation Eq. 7.1. The transition between a closed bond and an open bond is a stochastic process defined by:

$$q_i(t+\Delta t) = q_i(t) - q_i(t)H(\xi_i - \Delta t k_{off}) + (1-q_i(t))H(\xi_i - \Delta t k_{on}) \tag{7.4}$$

where $H()$ is the Heaviside step function, ξ_i is a random number in $(0,1)$. Eq. 7.4 defines bond transition and will be used to update each bond status with the formation and dissociation rate k_{on} and k_{off} defined later in the section.

If it is a closed bond, then the force in the individual bond is defined according to Hook's law: $f_i = k_b(l_i - l_0)$, where k_b is the spring constant of the bond, with the projection in the X direction $f_i^x = f_i x_i / l_i$; l_i is the bond length and x_i is its projection in the X direction. The geometrical relation defines: $x_i = \sqrt{l_i^2 - l_0^2}$ and l_0 is the initial bond length and the distance between the sensor disk and the adhesion plaque. Thus,

$$f_i^x = f_i \sqrt{1 - (l_0/(l_0+\Delta l_i))^2} \tag{7.5}$$

The bond movement ($\dot{x}_i$) can be defined with respect to the substrate movement ($\dot{X}$) as:

$$\dot{x}_i = q_i\dot{X} + \lambda(1-q_i)x_i \tag{7.6}$$

Eq. 7.6 builds the position relationship between the bonds and the substrate and x_i will be used to update the length of each bond and eventually the formation and dissociation rate k_{on} and k_{off}.

The bond formation and dissociation is defined in Bell's model [60, 211], which describes the impact of mechanical forces on the kinetics of bond formation/dissociation, especially on the rate of dissociation as:

$$k_{off}(l_i) = k^0_{off} e^{\beta f_i \Delta l_i} \tag{7.7}$$

$$k_{on} = \begin{cases} k^0_{on} & \text{if} \tau_c > \tau_b \\ k^0_{on}\frac{\tau_c}{\tau_b} & \text{if} \tau_c < \tau_b \end{cases} \tag{7.8}$$

where Δl_i is the bond stretch; $\beta = \frac{1}{k_B T}$; τ_c is the contact time defined by the time during which the free end of an integrin is exposed to a moving contact area, and it is inversely proportional to the moving speed: $\tau_c = L_c(\dot{X} - \Delta\dot{l}_s)$, where Ł$_c$ is the contact length and $\dot{X}$ and $\Delta\dot{l}_s$ are speed of the adhesion plaque motion and the stress fiber extension, respectively. τ_b is the intrinsic association time of integrin and ligand molecules on the order between 0.01 and 1 sec, and we used a value of 0.01 sec [212]. Eqs. 7.7 and 7.8 will update the status of each bond in association with Eq. 7.4.

The actin filament is represented by a viscoelastic Voigt element, i.e., spring-dashpot combination in parallel. The force balance in the actin filament with respect to the binding forces is defined:

$$\sum_{i=1}^{N} q_i f_i = k_s \Delta l_s + \mu_s \Delta \dot{l}_s \tag{7.9}$$

where k_s and μ_s are the elastic and damping coefficient of the stress fiber; Δl_s is the extension of the stress fiber. The total force from the closed bonds is balanced by the stress fiber with elastic component $k_s \Delta l_s$ and viscous component $\mu_s \Delta \dot{l}_s$. Eq. 7.9 uses the force information in all the bonds and calculates the extension of the stress fiber Δl_s. The energy dissipation of the mechanical model mainly comes from these two channels: the friction at the interface of cell-disk contact (E_a) and the viscous damping of the stress fiber ($E_d = \int \sum_{i=1}^{N} q_i f_i \Delta l_s dt$). The cell-disk friction ($E_a = E_b + E_v$) at the microscopic level also comes with two components: the rupture of adhesion bonds between the cell and the sensor disk ($E_b = \int \sum_{i=1}^{N} f_i \Delta l_i dt$) [185] and the viscous damping through the trapped liquid at the interface ($E_v = \int \eta_l \dot{X}^2 dt$).

7.2.3 Gaussian compensation of oscillation amplitude

The quartz crystal of the sensor disk oscillates in different amplitude from different regions; as studies have shown that a bell-shaped curve could be drawn for the relationship of the amplitude with respect to the position on the sensor disk [208]. The amplitude is largest in the center and fades away at the peripheral. Gaussian distribution compensation was applied to the simulation to mimic this phenomenon. A Gaussian distribution profile for the oscillation of the sensor disk was generated according to the equation:$A = \frac{A_0}{2\pi} e^{-\frac{(x-x_0)^2+(y-y_0)^2}{\sigma^2}}$, where A denotes the oscillation amplitude in nanometer, i.e. the initial spring displacement (Fig. 7.2A); A_0 is a coefficient to normalize the amplitude values to render the largest amplitude to be 1 nm; x and y are indexes for the dimension on the disk and σ is the variance defining the width of the Gaussian. The profile generated with $x_0 = 5$ and $y_0 = 5$ in a sensor disk with a diameter of 10 mm, and a $\sigma =$

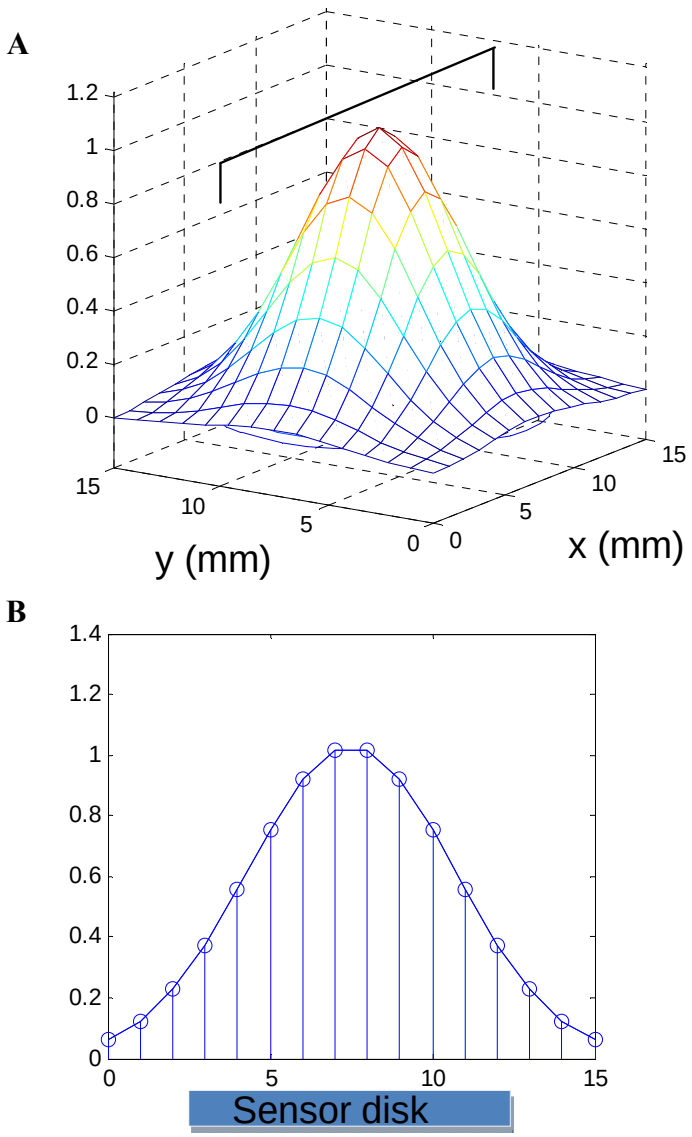

Figure 7.2 A: The initial spring displacement $L_{s0} - L_{sr}$ will be varied according to a Gaussian profile of the oscillation amplitude $A = L_{s0} - L_{sr}$ with the maximum amplitude $A0/2\pi$ of 1 nm and a variance of 3.16; B: Illustration of the sensor disk with manually divided areas with equal distribution of bonds, each was assigned with one amplitude.

3.16 is shown in Fig. 7.2B with 10 by 10 resolution. Each amplitude will be evaluated once by numerical simulation, and the 100 simulation data would be compiled together to obtain the energy dissipation data.

7.2.4 Numerical simulation

The calculations were achieved numerically with a Matlab program. The general strategy for the simulation is like the following. The states of all the bonds were then initialized along with the initial bond stretching Δl_i using Eq. 7.6 along with the geometrical relationship, bond formation (k_{on}) and dissociation rate (k_{off}) as in Eqs. 7.7 and 7.8. The system equilibrium was first achieved by a continuous 10 μs running. For each simulation step ($h = 10^{-8}s$), after the bond kinetics was initialized, the total bond force F_b can be calculated as in Eq. 7.3. The relationship between the bond movement ($\dot{x}_i$) and the substrate movement ($\dot{X}$) was defined subsequently as in Eq. 7.6. The master differential equation of the sensor disk dynamics was then solved numerically using the 4th order Runge-Kutta method [213]. The stress fiber stretching could then be updated as in Eq. 7.9. The total observation time is 50 μs and all the simulation parameters are listed in Tab. 7.1. The sensor disk has a thickness of 0.33 *mm* and a diameter of 14 *mm*. With the density of quartz comes around 2.65 g/cm^3, we can calculate the mass of the sensor disk around 0.134 g. Since the frequency of the harmonic oscillator is determined by the mass and spring constant as $f = \sqrt{\frac{K}{M}}$, to achieve nature frequency of 15 MHz, the spring constant is designed to be 3.05 $\times 10^{13} N/m$. Other parameters were based on values provided in previous literature.

7.3 Result and discussion

7.3.1 The dynamics of the sensor disk and the kinetics of the bond

The disk model behaves in harmonic oscillation rather than the thickness-shear mode that QCMD operates. Only the stored oscillation energy is twice than in thickness-shear mode, while other characteristics remain [190, 220]. The oscillation amplitude diminishes over time due to the direct

Table 7.1 The parameters in the model with their physical meanings used for the simulation

Symbol	Physical meaning	value	Ref.
M	Mass of the sensor disk	0.134 g	
K	Spring constant of the main spring	$3.05 \times 10^{13} N/m$	
k_B	Boltzmann constant	$1.38 \times 10{-}23 m^2 kg s^{-2} K^{-1}$	
T	Room temperature	310 K	
η	Damping coefficient	$10^{-3} Ns/m$	[214]
k_{on}^0	Forward rate constant	$100 s^{-1}$	[212,215]
k_{off}^0	Reverse rate constant	$1 s^{-1}$	[215,216]
k_b	Bond spring constant	$10 nN/\mu m$	[211,212]
k_s	Spring constant of stress fiber	$45\ nN/\mu m$	[66]
μ_s	Viscosity of stress fiber	$45 nNs/\mu m$	[66,217]
l_0	Initial bond length	10 nm	[211,218]
l_c	Contact length of the bond	20 nm	[219]

mechanical coupling between the cell and extracellular matrix, i.e. the sensor disk. This mechanical coupling is decomposed into the pulling/pushing of the focal adhesion to the cytoskeleton [221] and the viscous damping at the interface [207,208]. Shown in Fig. 7.3 is the dynamics of the sensor disk at a given initial displacement of 1 nm for a given simulation time of 5 μs. The displacement oscillates between -1 nm and 1 nm with the amplitude gradually decreases over cycles while the maximum speed diminishes correspondingly; and the kinetic energy is dissipated at a factor of around $10^{-5}(1 - E_t/E_0)$ shown in Fig. 7.3D.

The spontaneous bond association and rupture processes are strongly influenced by the relative motion between the sensor disk and the cell. As shown in Fig. 7.3 third panel, in each oscillation cycle when the speed goes beyond a certain value ($V_C \simeq 6.0 \times 10^{-4}$) determined from simulation shown in the Fig. 7.3B and C, the bond formation will be interrupted and the ratio of intact bond decreases dramatically to as low as 0.2; as more and more bond breaks, the force in the remaining bond increases, promoting the ensuing bond rupture probability. The synchronized bond dissociation in the stochastic bond behavior displayed the characteristics of the stick-slip motion

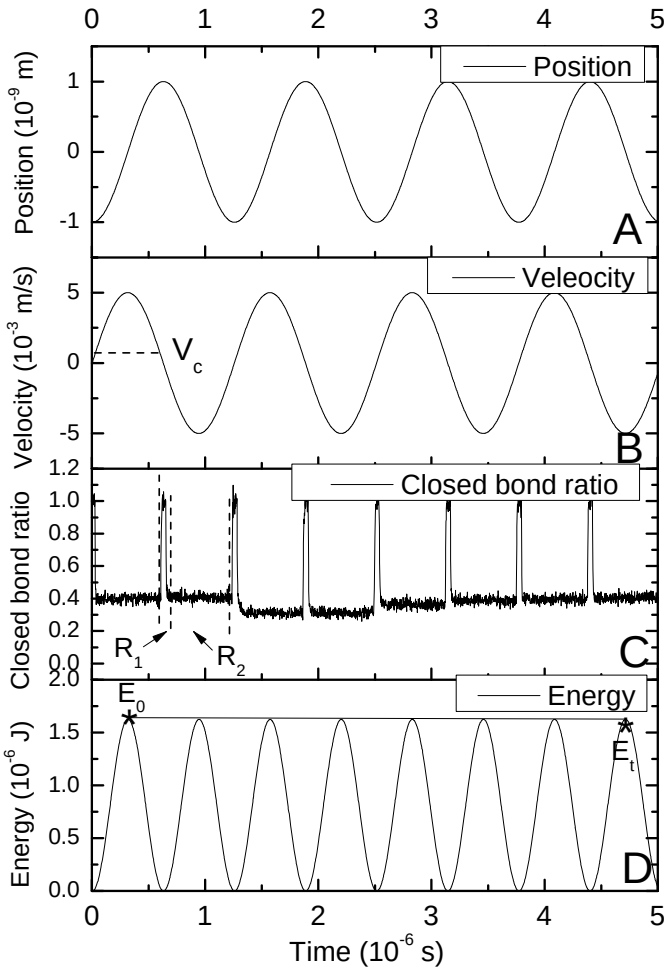

Figure 7.3 The simulation result at a given initial displacement of 1 nm for a period of 5 μs.

regime (R_2 in Fig. 7.3C) at a relative high speed of movement. At this regime, the stick-slip of the bond/disk interaction would lower the energy barrier required for unbinding and thus raises the frequency of bond dissociation, resulting kinetic energy loss. This energy loss is defined as the energy summation of every bond breaking events: $\sum_{i=1}^{N} f_i \Delta l_i$ [185]. At speed lower than V_C, the bond formation and rupture process was not influenced and the closed bond ratio hovers around the value of $k_{on}/(k_{on}+k_{off})$, which is a little less than 1; and the absence of correlation between individual bond formation and rupture events is a distinct feature of spontaneous thermal bond dissociation in the low-velocity sliding regime (R_1 in Fig. 7.3C) [206]. The binding/unbinding probability is not

affected at this regime and thus no energy is consumed in this period of every oscillation cycle.

7.3.2 Contributions from different energy dissipation source

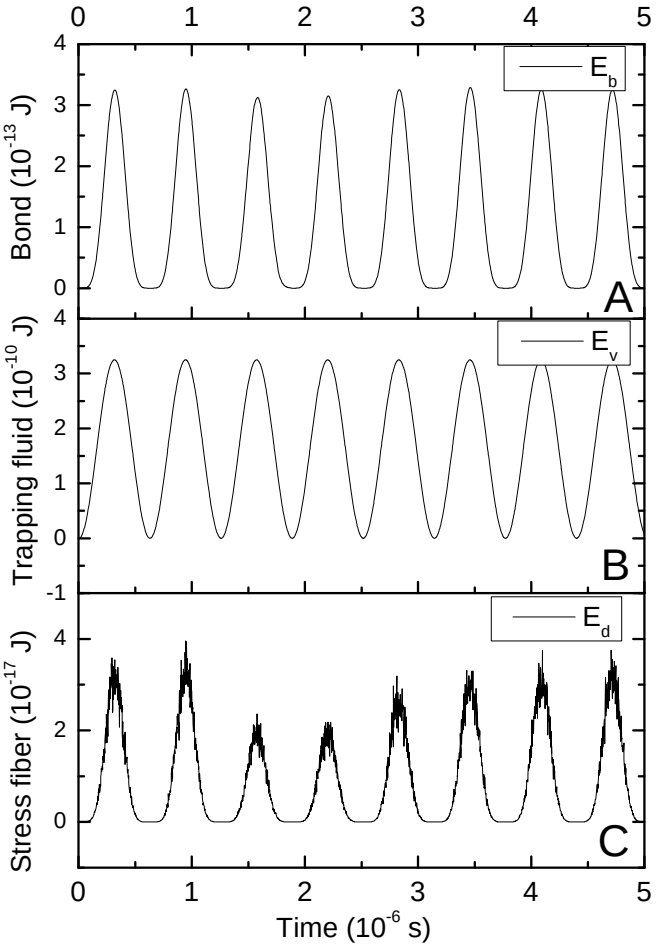

Figure 7.4 Dynamic energy dissipation for the three channels

There are three main channels of energy dissipation in the mechanical model. The dynamic molecular bond rupture events and the viscous damping caused by the trapping fluid dissipate energy as friction at the cell-sensor disk interface. The friction at the intracellular level is characterized by the viscous damping of the stress fiber, as the force in the focal adhesion complex is balanced by the stress fiber. These three energy dissipation channels consumed the dynamic energy

of the oscillating disk, and the simulation also showed that the sum of the three channels equal the total kinetic energy loss.

Of the three energy dissipation channels, the stress fiber dissipates the least energy; six orders lower than the viscous damping of the trapping liquid at the interface. The bond rupture energy dissipation is three orders less than the trapping liquid dissipation simulated when bond number is 10^5. The three dynamic energies shown in Fig. 7.4 is calculated based on the energy consumed in a period of each simulation time step ($h = 10^{-8}s$). As the number of bond increase, both the viscous damping by the trapping fluid and the stress fiber remain in the same level (10^{-6} and 10^{-11}, respectively). However, the energy dissipation through the synchronized bond rupture events increased almost linearly with respect to the bond number (Shown in Fig. 7.5). At the bond number around 4×10^8, the bond rupture energy levels with the viscous damping of the trapping liquid; and it dominates the total energy dissipation at bond number 10^9 and beyond. It is worth noting that these energy dissipation values and contribution relationships were calculated for a simulation time of 5 μs. At longer observation time, these values vary but the relationship remains.

7.3.3 Relationship of bond number and energy dissipation

Since the viscous damping of the trapping liquid will remain the same as the bond number increase causing the increase in the bond rupture dissipation, thus we can expect a linear increase in total energy dissipation, considering the fact that stress fiber energy dissipation is negligible. This was confirmed by the simulation when the bond number goes from 3×10^7 to 3×10^9 shown in Fig. 7.6A. A further increase in bond number to 10^8 shows that the linear relationship transforms to an exponential decay at bond number 4×10^9 and beyond as shown in Fig. 7.6B, with the linear portion correlating with bond number range in Fig. 7.6A.

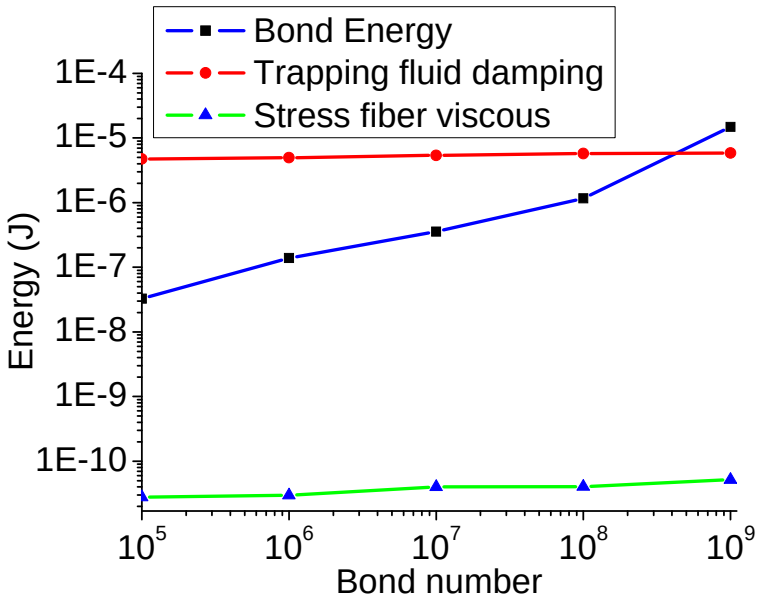

Figure 7.5 The energy dissipation channel contribution with respect to the bond number.

The documented data about bond density in focal adhesion supports the concept of molecular bonds at a higher number than 10^9. Based on the size of the sensor disk and considering the cells with area around 1000-2000 μm^2 [221,222], the disk would contain a monolayer of 10^5 cells. The bond density for focal adhesion is around 200-500 bonds per μm^2 [223], thus we could estimate that the total effective bond number would be in the order of 10^{10}. The measurement data from QCM-D for energy dissipation has D around 400×10^{-6}, from Fig. 7.6A it can be determined that the effective bond number that are contributing to the energy dissipation process is around 1.6×10^9. Therefore reasonably we could state that the energy dissipation arises predominantly from the bond rupture energy and the fluid friction at the interface, and thus the energy dissipation factor would appear linearly correlated with the bond number or further size of the focal adhesion if we assume the bond density over the entire focal adhesion is uniform.

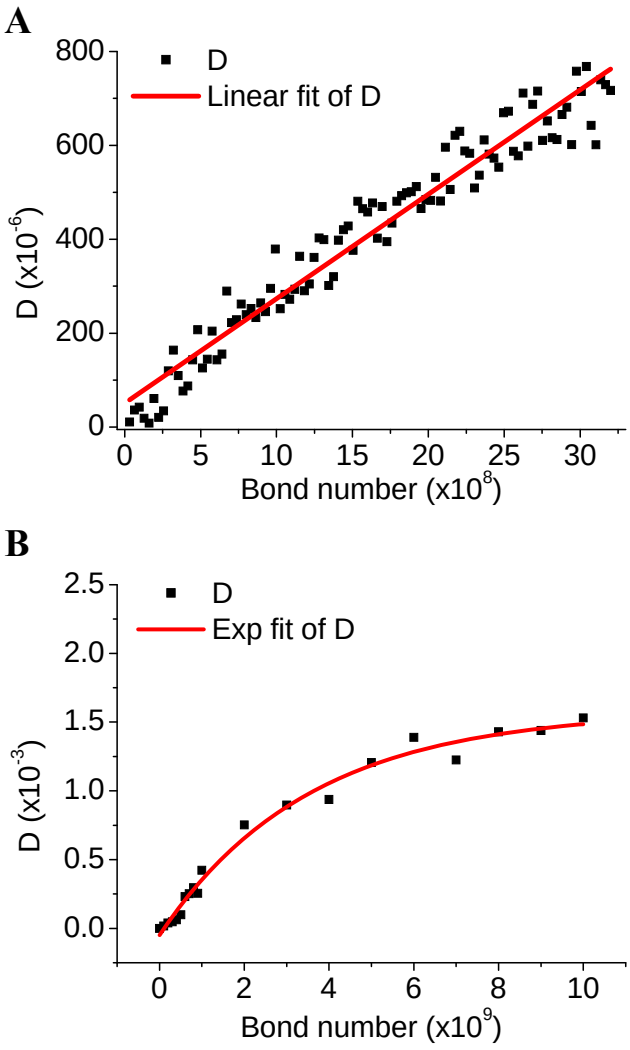

Figure 7.6 The energy dissipation increases linearly with the bond number.

7.3.4 Experimental observations

The EGF treatment reduced the size of the focal adhesion, and the change is in a time-dependent manner and it is correlated with the real-time energy dissipation factor measurement from the QCM-D [68]. The simulation uses the time-lapse normalized focal adhesion sizes as the reference input, and linearly converts them to bond number (100 percent correlates with bond number of 1.6×10^9), and the energy dissipation factors corresponding to each bond number would then be calculated based on the fitting equation for Fig. 7.6B: $D = 0.0016(1 - e^{-B/3.5\times10^9})$. A strong corre-

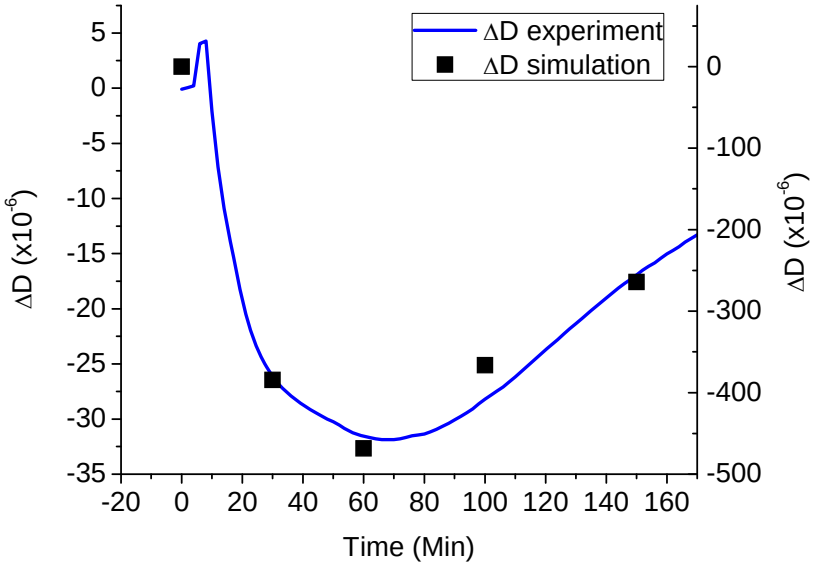

Figure 7.7 The simulation data comparison with the experimental observation

lation between the energy dissipation factor from simulation (black) and from QCM-D experiment (blue) is clearly visible as shown in Fig. 7.7.

7.4 Chapter summary

In this chapter, we designed a mechanical model based on the physical interaction between the QCM-D disk and the cell focal adhesion. The proposed model considers the sensor crystal as a harmonic oscillator and the friction at the cell/disk interface due to the dynamic molecular bond rupture as well as the viscous damping at stress fiber/cytoplasm causes the kinetic energy loss during each oscillation cycle. We found that the QCM-D energy dissipation comes mainly from the cell focal adhesion and sensor interaction, and the viscous damping caused by the trapping fluid at the interface and by the stress fiber contribute insignificantly. The energy dissipation almost linearly correlates with the bond number and thus the focal adhesion size. The finding confirms the experimental results obtained early with the similar correlation. The proposed model, different

from present models which are overwhelmingly relied on equivalent circuit method, emphasizes the importance of the physical interaction between the focal adhesion and the sensor disk and its role in the energy dissipation process of sensor oscillation. Proved valid, this model and its simulation result could well serve as an analytical tool for QCM-D based measurements of cell adhesion.

Chapter 8

Modeling of signaling pathway dynamics

8.1 Introduction

EGFR is a transmembrane receptor that regulates cell growth, proliferation, motility, and differentiation through its downstream signaling pathways [224, 225]. These pathways are activated by the binding of EGF to the extracellular domain of EGFR, followed by phosphorylation of the cytoplasmic tyrosine kinase. Because of its critical role in regulation of cell growth, proliferation, motility, and differentiation, an abnormal level of EGFR can often lead to aberrant cell signaling, which may induce uncontrolled cell growth and malignant phenotypes. This is evidenced by the fact that EGFR is highly expressed in a variety of human tumors [226]. In particular, overexpression of EGFR appears to promotes aberrant cell motility that has often been associated with tumor invasion and metastasis [227].

EGF-induced cell motility is a highly coordinated cellular function involving precise regulation of cell adhesion and de-adhesion to extracellular matrix (ECM) proteins by multiple downstream pathways of EGFR signaling [228]. Three pathways, the phosphoinositide 3-kinase (PI3K) pathway, the mitogen-activated protein kinase/extracellular signal-regulated kinase (MAPK/ ERK) pathway, and the phospholipase C (PLC) pathway, have previously been linked to the mediation of the assembly and disassembly of focal adhesions that lead to changes in cell adhesion in various cell lines [229, 230]. Although many of the key signaling molecules in each pathway have been elucidated and characterized, the understanding of how these pathways regulate cell motility

through coordination of cell adhesion and de-adhesion, is still limited by the complexity of this cell signaling system, particularly its inherent nonlinearity (e.g., crosstalk, feedback loop, feedforward loop) and dynamic complexity.

By far the traditional reductionist approach has failed to elucidate the decisive signaling reactions and molecules that are responsible for the cellular functions, which are often integrated outputs of multiple signaling pathways [231]. A quantitative understanding of regulation of cellular functions is also seriously lacking. Thus, it becomes necessary to introduce computational modeling approach at the system level to examine cellular functions in order to determine the responsible properties and interactions of the cellular components and assess how these components work together to generate an integrated downstream signal output in response to various extracellular cues.

Over the years, mathematical models have been developed to quantitatively describe various aspects of EGFR signaling [232, 233] including receptor dynamics and trafficking [234, 235] and downstream signaling events [236–238]. The transient versus the sustained responses of the MAPK cascade [239–241], autocrine positive-feedback loops [242, 243], the cross-talk between the downstream pathways of EGFR [243] have also been the areas of interests. Most of these models are described by a set of ODEs derived from a set of stoichiometric reactions and the dynamics of the involved species based on the prior knowledge of their kinetic constants and concentrations [244].

Computational models of dynamic cell adhesion based on the receptor-ligand bonds between the cytoskeleton and ECM have also been the focus of growing research activities. These models have provided quantitative analyses that have led to mechanistic insights into a wide range of cellular processes such as cell spreading, migration, proliferation and differentiation. The thermodynamic framework of cell adhesion models was established by Bell back in 1978 [60]. Based

on his seminal work, peeling models were developed to reveal the kinetics of cell adhesion and de-adhesion through quantitative mechanics of cell membrane [61,218,245,245]. A statistical mechanics model was also established to probe the adhesion of multicomponent membranes mediated by specific adhesion molecules [246, 247]. The stochastic effects of adhesion bonds switching between open and closed states under constant force were investigated [248], so were the behaviors of focal adhesions under various exogenous mechanical stimuli [249–252]. Some of the recent studies have been focused on dynamics of integrins which serve as clutches that link F-actin and ECM [214, 253, 254].

Although the importance of EGFR signaling in mediating cell adhesion has attracted a significant research interest in recent years, particularly in cancer research [58, 255–257], none of signal-to-response models describing the coupling between multi biochemical pathways mediated by EGFR signaling and adhesion mechanics of the cell has been reported. To our knowledge, the only model that has made an attempt for a coupling between cell signaling and cell mechanics is the one developed by Besser and Schwarz, where they connect the Rho pathway to adhesion mechanics by treating the mechanical force as enzyme in the framework of Michaelis-Menten kinetics [66]. Besides only a single pathway was considered for the model, the validity of treating the mechanical force as enzyme is also open to question. This could be attributed to the lack of understanding of the molecular mechanism concerning the mechanotransduction. It is clear that the development of an EGFR signaling-to-cell adhesion model that provides insight into how signals generated by environmental stimuli lead to phenotypic cell behavioral responses is one of the major challenges in system biology [258]. This requires the establishment of a molecular element that links between EGFR signaling and the mechanical response of the cell during alteration of cell adhesion.

We hypothesize that such a cellular element is focal adhesions, which are a type of adhesion

protein complexes located across the bottom surface of cells that are primarily responsible for cell adhesion to ECM and substratum [259]. The assembly and disassembly of focal adhesions are known to be regulated by the pathways mediated by EGFR signaling [229, 230]. Therefore biochemical model that describes the regulation of the restructuring of focal adhesions by EGFR signaling and biomechanical model that depicts the cell-substrate adhesion through focal adhesions could be linked together through focal adhesions. Based on this coupling, we propose to model the regulation of dynamic changes in cell adhesion by EGFR signaling.

The dynamic change in cell adhesion can be measured with the use of a nanomechanical sensor in QCM-D. The QCM-D is a highly sensitive nanomechanical device that provides simultaneous measurements of changes in frequency (Δf) and energy dissipation factor (ΔD) of an oscillating AT-cut quartz crystal [260]. ΔD is defined as the ratio of the loss of mechanical energy per oscillation period of the sensor crystal to the total mechanical energy input to the system. The QCM-D measurements provide an assessment of the changes in mass (from Δf) and mechanical properties (from ΔD) of a layer of biomolecules attached to the surface of the quartz crystal[45]. Because the acoustic signal diminishes exponentially with distance above the surface of the quartz crystal oscillator on which the cells are deposited, the QCM-D probes primarily the basal area of the cell monolayer [203, 261], which specifically relates to cell adhesion. This technique has been shown to be non-invasive to mammalian cells when the amplitude of shear oscillation is kept under 1 nm [199]. We have recently demonstrated a linear correlation between the level of focal adhesions, quantified based on number and size of vinculin (the key component of focal adhesions), and the ΔD -response of cells [68]. Because the level of focal adhesions is quantitatively related to the strength of cell adhesion [262–265], the time-dependent ΔD response could serve as a real-time, quantitative indicator of the strength of cell-substrate adhesion [193, 194].

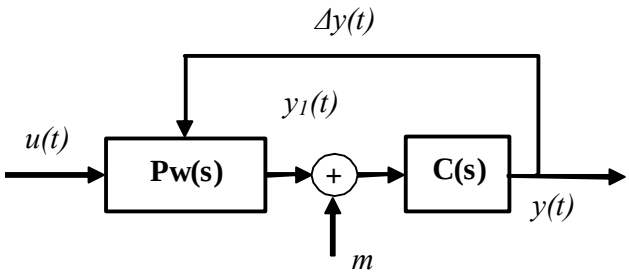

Figure 8.1 Diagram of control model of pathway dynamics

8.2 Model development

We propose to use quantitative modeling to dissect the signaling pathways involved in the process of the EGF-induced dynamic change of cell adhesion. The model will be constructed based on a system identification process, which is regularly employed in control system design to elucidate the unknown structures and parameters of some of the components in the system based on the prior knowledge and the input output information of the system [266]. A nanomechanical sensor in QCM-D, which is capable of generating real-time, continuous and measurable signals, will be used for evaluating the system output.

The proposed system structure is illustrated in Fig. 8.1. The signaling network that is known to regulate the EGF-induced cell adhesion is designated as the controller $Pw(s)$ of the system. The controller can convert the input signal $u(t)$ (e.g., EGF stimulation) to the execution signal $y_1(t)$, which is responsible for controlling the cell adhesion complex, the plant $C(s)$ of the system. Feeding the plant $C(s)$ with a measurement signal m from the QCM-D will result in the dynamic output $y(t)$, a quantity that correlates with the time-dependent ΔD signal of the QCM-D measurement. Meanwhile, the cells can also actively adjust to exogenous stimulation through a self-imposed adaption by sending the feedback signal $\Delta y(t)$ to the controller.

8.2.1 Plant model

As for the plant $C(s)$, the adhesion complex of adherent cells can receive the input signal u_2 from the EGF-activated signaling pathways. In response, the adhesion complex will undergo restructuring through dynamic assembly or disassembly of focal adhesions, resulting in the dynamic change in cell adhesion. This will be assessed based on the output of the system. The correlation between the level of cell adhesion and the ΔD response has been established in our previous study [68] . The cell layer attached to a QCM-D sensor can be modeled as a sensor disk anchored to a spring with an initial momentum [190] (Fig. 7.1). The dynamic equation for the movement of this sensor disk is defined as:

$$M\ddot{Y} + \eta\dot{Y} + f(u_2) + KY = 0 \tag{8.1}$$

where M is the mass of the disk, η is the damping coefficient, Y is the index of the disk horizontal motion, K is the spring constant, and f is the mapping coefficient from the focal adhesion to the sum of bond forces between the sensor disk and the cell adhesion complex. Therefore, represents damping by the trapping fluid underneath of the cell body and the interactive bond force is defined by the mapping $f(u_2)$. KY is the force in the spring and is the force resulting from the acceleration of the sensor disk. This equation is derived based on the assumption that the friction between the cell and the sensor disk and the viscous damping between the cell body and the liquid trapped underneath the cell body are the primary causes of the energy loss of the sensor disk. This assumption can be verified by comparing the sum of the friction and the viscous damping to the quantity of energy dissipation measured with the QCM-D. The system dynamics can be transformed to a state space model as:

$$\begin{bmatrix} \dot{Y}_1 \\ \dot{Y}_2 \end{bmatrix} = \begin{bmatrix} 0 & 1 \\ -\frac{K}{M} & -\frac{\eta}{M} \end{bmatrix} \begin{bmatrix} Y_1 \\ Y_2 \end{bmatrix} + \begin{bmatrix} 0 \\ -\frac{f}{M} \end{bmatrix} u \tag{8.2}$$

with the two state variables Y_1 and Y_2 denoting the position and velocity of the oscillating sensor disk. These two states specify the input of the QCM-D measurement signal $m = [Y_1, Y_2]^T$. The output from the mechanical model is defined as the rate of dissipation of kinetic energy:

$$Y = \frac{d}{dt}(\frac{1}{2}MY_2{}^2) \tag{8.3}$$

which is quantitatively related to the ΔD response measured with the QCM-D.

The detailed analysis of the plant model yields an exponential relationship between the input for the plant, the number of integrin-ECM bonds, and the output of the plant, the energy dissipation factor, ΔD as shown in Fig. 8.2. The fitted curve shows a relationship that is defined by equation:

$$D = 0.0016(1 - e^{-\frac{B}{3.5\times10^9}}) \tag{8.4}$$

which would then be converted to a transfer function of:

$$c(s) = \frac{1}{625s(3.5 \times 10^9 s + 1)} \tag{8.5}$$

The detail of the characterization process can be found in Chapter 7. Briefly, the mechanical oscillation by the sensor disk would be damped by the interaction of the molecular bonds between the cell and the disk. The process of bond friction relies on breaking of bonds to dissipate the kinetic energy of the disk, and this process is a stochastic process defined by Bell's model [60], which in the overall control architecture determines the bond number conversion to the friction

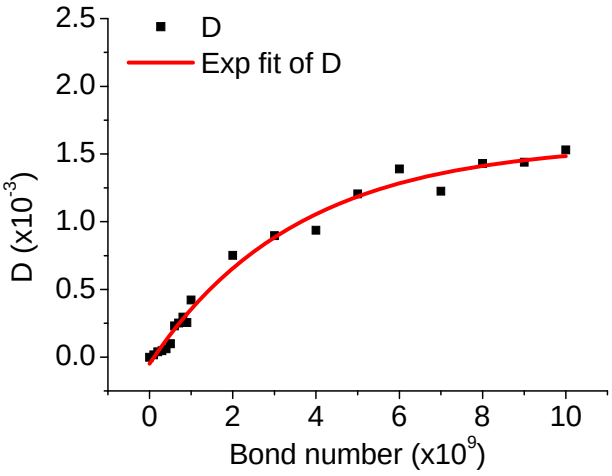

Figure 8.2 The exponential relationship of the input and output for the plant model.

force or $f(u_2)$. Plug the friction force to the second order ODE would result in the relationship between the number of bonds u_2 and the output Y which is the energy dissipation factor, the quantity that measured by QCM-D in the real-time experiment.

8.2.2 The controller model

We define the controller as the EGF-mediated signaling network that regulates cell adhesion (i.e., restructuring of focal adhesions). This controller includes the PLC pathway (Pw_a), the PI3K pathway (Pw_b), and the MAPK/ERK pathway (Pw_c). Some of the signaling molecules that are involved in EGFR activation and its downstream cascades will not be included in the initial model, but will be considered during the model refinement [236, 237]. The state variable of Pw is designated as the concentration of a specific downstream effector molecule that is directly involved in regulation of restructuring of focal adhesions (e.g., calpain in the MAPK/ERK pathway). The change in concentration of a species involved in a signaling reaction is usually described with an ODE. For example, when EGF binds to the EGF receptor on the membrane of the cell: [EGF] + [FreeEGF-receptor] $\rightleftharpoons$ [Bound-EGF-Receptor] (BEGFR), and the reaction is regarded as a mass reaction,

thus the time-dependent change in concentration of BEGFR can be described mathematically by an ODE:

$$\frac{d[BEGFR]}{dt} = k_{rbEGF}[EGFR][EGF] - k_{ruEGF}[BEGFR] \tag{8.6}$$

where [EGFR] is the concentration of EGF receptors on the cell membrane, [EGF] is the concentration of EGF and is the overall input of the system u, k_{rbEGF} and k_{ruEGF} are the forward and reverse reaction rate constants (binding/unbinding of EGF to the free EGF receptor). The concentration of [EGFR] can then be determined based on these parameters, which are available from previous biochemical, biophysical, and modeling studies [236, 243, 267–269]]. For a Michaelis-Menten reaction, like the Rac molecule activates Rho, the process can be defined by:

$$\frac{d[ActiveRho]}{dt} = +k_{Rho}[ActiveRac]\frac{[InActiveRho]}{[InactiveRho] + k_m Rho} \tag{8.7}$$

where [ActiveRho] and [InActiveRho] are the concentrations of active and inactive Rho, and [ActiveRac] is the concentration of active Rac; k_{Rho} is the rate constant for the reaction and k_{kmRho} is the Michaelis constant for the Michaelis-Menten reaction.

To determine the concentration of a downstream effector may require solving a series of ODEs derived from sequential signaling reactions upstream in the pathway. The detailed system consists of 14 molecules that primarily determine the output of the effector molecule for cell adhesion regulation. From the 14 molecules, we employed 26 state variables based on their active and inactive status (the list of variables is shown in Tab. 8.1). The structure is shown in Fig. 8.3 on which the group of ODEs was based upon.

If the concentration or the rate constant of a particular species is not readily available, an estimate based on the information on a related species may be used for the calibration of the initial model. Such estimated parameters can be determined eventually through model fitting of

Table 8.1 State variables and ODEs

Variables	Physical Meaning	ODEs
X_1	[EGF]	$\frac{dX_1}{dt} = -k_{rbEGF}X_1X_2 + k_{ruEGF}X_3$
X_2	[Free EGF Rec]	$\frac{dX_2}{dt} = -k_{rbEGF}X_1X_2 + k_{ruEGF}X_3$
X_3	[Bound EGF Rec]	$\frac{dX_3}{dt} = +k_{rbEGF}X_1X_2 - k_{ruEGF}X_3$
X_4	[Active Ras]	$\frac{dX_4}{dt} = +k_{Ras}X_3\frac{X_5}{X_5+k_{mRas}} - k_{ERKRas}X_18\frac{X_4}{X_4+k_{mERKRas}}$
X_5	[InActive Ras]	$\frac{dX_5}{dt} = -k_{Ras}X_3\frac{X_5}{X_5+k_{mRas}} + k_{ERKRas}X_18\frac{X_4}{X_4+k_{mERKRas}}$
X_6	[Active Raf]	$\frac{dX_6}{dt} = +k_{Raf}X_4\frac{X_7}{X_7+k_{mRaf}} - k_{AktRaf}X_10\frac{X_6}{X_6+mAktRaf}$
X_7	[InActive Raf]	$\frac{dX_7}{dt} = -k_{Raf}X_4\frac{X_7}{X_7+k_{mRaf}} + k_{AktRaf}X_10\frac{X_6}{X_6+mAktRaf}$
X_8	[Active PI3K]	$\frac{dX_8}{dt} = +k_{PI3K}X_3\frac{X_9}{X_9+k_{mPI3K}} + k_{RasPI3K}X_4\frac{X_9}{X_9+k_{mRasPI3K}}$
X_9	[InActive PI3K]	$\frac{dX_9}{dt} = -k_{PI3K}X_3\frac{X_9}{X_9+k_{mPI3K}} - k_{RasPI3K}X_4\frac{X_9}{X_9+k_{mRasPI3K}}$
X_{10}	[Active Akt]	$\frac{dX_{10}}{dt} = +k_{Akt}X_8\frac{X_{11}}{X_{11}+k_{mAkt}}$
X_{11}	[InActive Akt]	$\frac{dX_{11}}{dt} = -k_{Akt}X_8\frac{X_{11}}{X_{11}+k_{mAkt}}$
X_{12}	[Active Rac]	$\frac{dX_{12}}{dt} = +k_{Rac}X_8\frac{X_{13}}{X_{13}+k_{mRac}}$
X_{13}	[InActive Rac]	$\frac{dX_{13}}{dt} = -k_{Rac}X_8\frac{X_{13}}{X_{13}+k_{mRac}}$
X_{14}	[Active Rho]	$\frac{dX_{14}}{dt} = +k_{Rho}X_12\frac{X_{15}}{X_{15}+k_{mRho}}$
X_{15}	[InActive Rho]	$\frac{dX_{15}}{dt} = -k_{Rho}X_12\frac{X_{15}}{X_{15}+k_{mRho}}$
X_{16}	[Active MEK1/2]	$\frac{dX_{16}}{dt} = +k_{MEK}X_6\frac{X_{17}}{X_{17}+k_{mMEK}} - k_{dPP2AMEK}X_20\frac{X_{16}}{X_{16}+k_{mPP2AMEK}}$
X_{17}	[InActive MEK1/2]	$\frac{dX_{17}}{dt} = -k_{MEK}X_6\frac{X_{17}}{X_{17}+k_{mMEK}} + k_{dPP2AMEK}X_20\frac{X_{16}}{X_{16}+k_{mPP2AMEK}}$
X_{18}	[Active Erk1/2]	$\frac{dX_{18}}{dt} = +k_{ERK}X_16\frac{X_{19}}{X_{19}+k_{mERK}} - k_{dPP2AERK}X_20\frac{X_{18}}{X_{18}+k_{mPP2AERK}}$
X_{19}	[InActive Erk1/2]	$\frac{dX_{19}}{dt} = -k_{ERK}X_16\frac{X_{19}}{X_{19}+k_{mERK}} + k_{dPP2AERK}X_20\frac{X_{18}}{X_{18}+k_{mPP2AERK}}$
X_{20}	[Active PP2A]	$\frac{dX_{20}}{dt} = 0$
X_{21}	[Active PLCγ]	$\frac{dX_{21}}{dt} = +k_{PLC\gamma}X_3\frac{X_{22}}{X_{22}+k_{mPLC\gamma}}$
X_{22}	[InActive PLCγ]	$\frac{dX_{22}}{dt} = -k_{PLC\gamma}X_3\frac{X_{22}}{X_{22}+k_{mPLC\gamma}}$
X_{23}	[Active PIP2]	$\frac{dX_{23}}{dt} = +k_{PIP2}X_{21}\frac{X_{24}}{X_{24}+k_{mPIP2}}$
X_{24}	[InActive PIP2]	$\frac{dX_{24}}{dt} = -k_{PIP2}X_{21}\frac{X_{24}}{X_{24}+k_{mPIP2}}$
X_{25}	[Active Cofilin]	$\frac{dX_{25}}{dt} = +k_{Cofilin}X_{23}\frac{X_{26}}{X_{26}+k_{mCofilin}}$
X_{26}	[InActive Cofilin]	$\frac{dX_{26}}{dt} = -k_{Cofilin}X_{23}\frac{X_{26}}{X_{26}+k_{mCofilin}}$

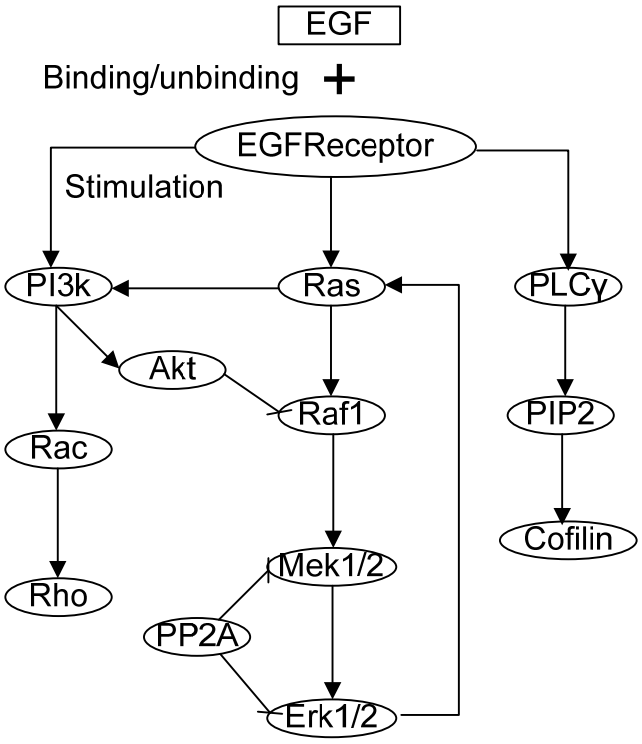

Figure 8.3 The system of molecules that ODEs were built upon.

the experimental data. The rate constants for the 26 ODEs are listed in Tab. 8.2. A combination of equations can easily be built for a more specific and complicated signaling network based on the registered items in the database. The overall signal output from the entire signaling network will be represented as a weighted linear combination of three pathways:

$$y_1 = \alpha Pw_a + \beta Pw_b + \gamma Pw_c \tag{8.8}$$

where α, β and γ are mapping parameters.

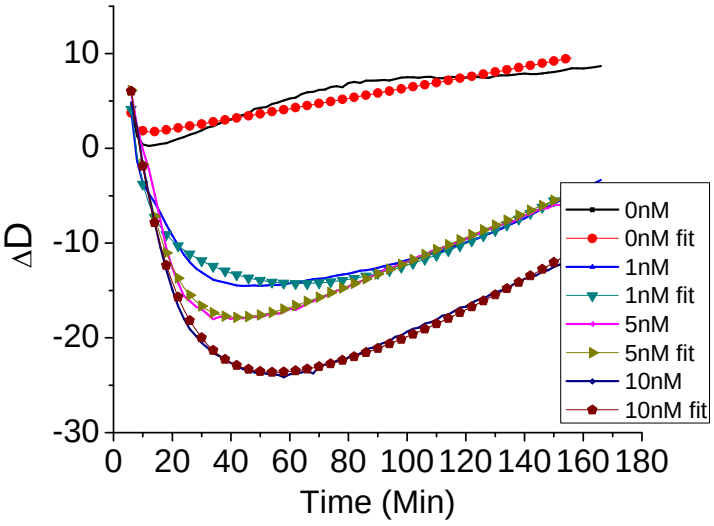

Figure 8.4 The fitting result for EGF treatment of A431 cells based on the control model.

8.3 Result

The parameter for the control model $Pw(s)$ was obtained mostly from the paper by Brown et al. [268]. For the unknown parameters, we used a fitting algorithm to fit the experimental data with the model and obtain an optimal parameter set. For the EGF treatment of the A431 cells, the real time energy dissipation factor data were then fitted. The data would then be tested when one or several of the pathways were to be blocked.

The real-time measurement of energy dissipation variations is compared against the simulation data from the model in Fig. 8.4. Based on the parameters from literature, the model fits the experimental data with precision for concentrations of 1, 5 and 10 nM. The dynamics model shows discrepancies with the experimental data only at the first phase of the cell adhesion transition (Phase I) when the cell deadhesion dominates the process with drastic restructuring. Features in Phase II and III with stable configuration and gradual recovery of cell adhesion are well captured.

Of equal importance, the expression of these key molecules in the pathway can be analyzed. It has been reported [68] that the three branches of pathway cascade induce different outcomes of cell

adhesion. Specifically, the PLC pathway strengthens the focal adhesion complex and promotes the assembly of focal adhesion while inhibits the disassembly of cell adhesion. On the contrary, both the MAPK pathway and the PI3K pathway destabilize the focal adhesion structure and compel the disassembly of the focal adhesion. As the cell experience the rise and fall of the cell adhesion both in size and strength as indicated by the energy dissipation and fluorescence labeling, the expression of these key molecules also fluctuates. The model could also be tested by blocking certain branches of the pathway and monitor the response.

As shown in Fig. 8.5, the expression levels of Rho, MEK and PLCγ over the course of preservation are plotted. Both the levels of Rho and MEK went up in Phase I, though the temporal dynamics of these two molecules did not overlap. The upregulation of MEK experienced a more drastic boost during the first 20 minutes of EGF stimulation and reached plateau 15 minutes into the observation; while the deregulation had a similar temporal dynamics. The expression level of Rho increased at a pace shared with the overall deadhesion. It plateaued at around the end of Phase I and the inception of Phase II, and subsequently dropped at a slower rate than MEK. Since both pathways are responsible for the disassembly of focal adhesion, the increase of both would shadow or at least neutralize the promoting effect of the PLC pathway. Additionally, the downregulation of PLCγ begins slowly after receiving EGF signal, which exacerbates the disassembly of the focal adhesion. After Phase II, however, the combined effect of both decreased levels of MEK and Rho, plus the upswing of the PLCγ would essentially bring back the focal adhesions that were previously disrupted. A concerted effort of these key molecules in the pathway dynamics accomplished the delicate task of cell adhesion regulation.

The overall effect of the molecule dynamics after EGF stimulation is manifested through the biophysical properties of the focal adhesions as well as the cytoskeleton mechanics, as the real-time measurement data from QCM-D tracks the change of energy dissipation that are directly

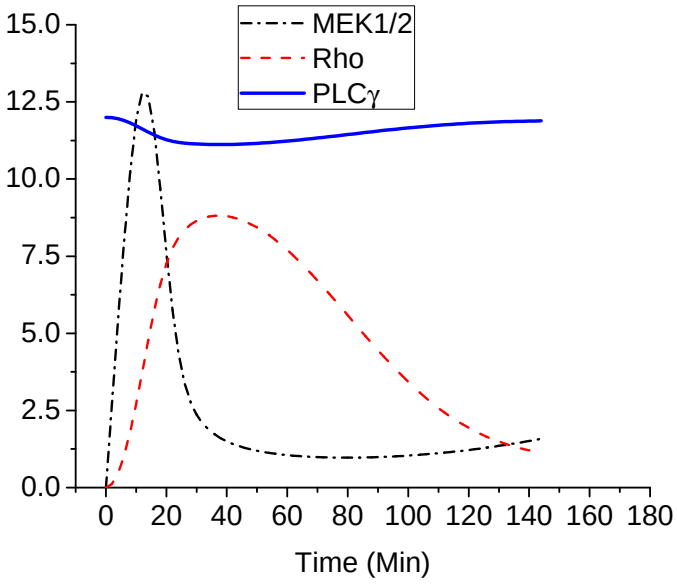

Figure 8.5 Expression levels of MEK1/2, Rho and PLCγ

related to the size and strength of focal adhesion. Leveraging this functional study, we were able to provide a multifaceted characterization of the EGF induced cell adhesion change. The analysis from the signaling pathway control model yields a unique peek into the biochemical dynamics of the regulation as well as the biomechanical dynamics of the adhesion. The simulation result compares well with the realtime measurement data. More importantly, the simulation provides the molecule dynamics in the process of regulation which can be verified by biochemical assays, such as Western blot. At the minimum, from the biochemical assay, we can build a calibration standard for each key molecule over the time course and we'll prevent the messy experiments from repeating. If the prediction from the model proves correct, we will find similar levels of protein expression during the EGF stimulation process.

8.4 Chapter summary

This chapter proposed a signaling pathway control model that aims to decipher intricate signaling pathways that regulate cell adhesion during EGF stimulation. The model leverages on the capabilities of nanomechanical senor in QCM-D which provides real time measurement of cell adhesion strength. A mechanical model was built to quantitatively relate the measurement value, energy dissipation (ΔD) with the dynamic bond formation/dissociation. This mechanical model was considered the plant controlled by the signaling pathway model. Upon obtaining the measurement output in ΔD and with prior knowledge of EGF concentration, we identified the key steps and branches of signaling pathways in the regulation process, or more specifically the dynamics of key molecules. The study initiates a unique methodology in delineating pathway dynamics that essentially eliminates the necessity of the messy, time-consuming biochemical assays, at least significantly reduces the amount of them, which will shed insight on the system biologists' approaches, as well as be of importance to the the modeling and control community. The result of the study will advance the understanding of the EGF regulated cell adhesion and benefit the development of therapeutics in cancer treatment with overexpression of EGFR.

Table 8.2 Rate constants

Reaction name	Reaction	Parameter	Value
EGF binding	EGF+ FreeEGFRec ⇔ BoundEGFRec	k_{rbEGF}	2.185E-5
Ras activation by bound EGFR	RasInactive → RasActive	k_{Ras} k_{mRas}	694.731 6086070
Ras deactivation by ERK1/2	RasActive → RasInactive	k_{ERKRas} $k_{mERKRas}$	1611.97 896896
Raf activation by Ras	RafInactive → RafActive	k_{Raf} k_{mRaf}	1509.36 1432410
Raf deactivation by Akt	RafActive →RafInactive	k_{AktRaf} $k_{mAktRaf}$	15.1212 119355
PI3k activation by bound EGFR	PI3kActive → PI3kInactive	k_{PI3K} k_{mPI3K}	10.6737 184912
PI3K activation by Ras	PI3kActive→ PI3kInActive	$k_{RasPI3K}$ $k_{mRasPI3K}$	0.0771067 272056
Akt activation by PI3k	AktActive→ AktInactive	k_{Akt} k_{mAkt}	0.0566279 653951
Rac activation by PI3k	RacActive → RacInactive	k_{Rac} k_{mRac}	Est. Est.
Rho activation by Rac	RhoActive → RhoInactive;	k_{Rho} k_{mRho}	Est. Est.
MEK1/2 activation by Raf	MEK1/2Active → MEK1/2Inactive;	$k_{MEK1/2}$ $k_{mMEK1/2}$	185.759 4768350
MEK1/2 deactivation by PP2A	MEK1/2Active → MEK1/2Inactive	$k_{PP2AMEK1/2}$ $k_{mPP2AMEK1/2}$	2.83243 518753
ERK1/2 activation by MEK1/2	ERK1/2Active → ERK1/2Inactive	$k_{ERK1/2}$ $k_{mERK1/2}$	9.85367 1007340
ERK1/2 deactivation by PP2A	ERK1/2Active → ERK1/2Inactive	$k_{PP2AERK1/2}$ $k_{mPP2AERK1/2}$	8.8912 3496490
PLCγ activation by bound EGFR	PLCγActive → PLCγInactive;	k_{PLC} k_{mPLCg}	Est. Est.
PIP2 activation by PLCγ	PIP2Active → PIP2Inactive	k_{PIP2} k_{mPIP2}	Est. Est.

Chapter 9

Conclusion and future work

9.1 Conclusion

9.1.1 Development of AFM nanorobotics for biomedical applications

The use of AFM as a robotic platform in changing materials especially biological materials at their native states has transformed the biomedical research significantly in numerous aspects. The unprecedented level at which AFM can visualize biological samples combined with the dexterity of the robotic control schemes makes the operation at the cellular level a possibility. With the AFM nanorobotic platform, cellular surgeries at nanometer precision were carried out to mimic the effect of antibody treatment; while the flexibility of a haptic device provide a convenient and efficient means for capturing the mechanical property changes at a survey mode.

The development of the platform requires the precise modeling of the interaction of the AFM end-effector, or cantilever with the biological samples, especially live cells, with complex material properties, and the control of the positioning of the end-effector monitors the interaction force and feedback to the operator. Living cells normally display a high level of viscosity, therefore, the operation frequency of the AFM manipulation should be high enough to provide the extra rounds of position and force feedback. We have developed a number of control schemes to increase the frequency so that the operation could be performed smoothly.

9.1.2 Dynamical monitoring of cellular structural and mechanical changes under patho/physiological conditions

The mechanical profile of cells gives out a wide spectrum of information regarding on their status, not only biophysical status, but biochemical status as well. The real-time observation and monitoring of these properties provides us a unique peek into the complex dynamics of the cell structural and the change of their biological behavior. We have demonstrated this concept by different sets of experiments on a number of biological stimuli-response processes.

The experiment with the insulinoma cells showed that the ionic response from the cell after stimulation from different chemical species can be revealed and delineated by a continuous monitoring of the subtle changes of the membrane heights in the order of a few tens of nanometers, and the change of cellular elasticity. The structural and mechanical alterations upon stimulation of glucose and capsaicin tracked by the AFM nanorobotics platform echoed the response from the ion channels, or the change of membrane capacitance. Thus the structure and mechanical profiles give us a signature of the ion channel activities of the cell, and we were able to establish a causal relationship of a single-phase biological process.

The experiment with the HaCaT cells provided us some insights in the cellular response when the cellular structures, specifically the adhesion structure, were damaged. We found that the cellular stiffness experienced a two-phase response when the keratinocytes were treated with an autoimmune antibody found in patients with Pemphigus Vulgaris. The stiffness dropped in the first hour of treatment, which was followed by an increase in the ensuing four hours of observation. We postulate that the loss of adhesion was directly caused by the loss of cellular adhesion between neighboring cells. The cellular adhesions as we consider are tensional anchoring sites to provide the mechanical support and maintain the integrity of the cell structures, the loss of which will result

in the decrease in the pre-stress, which determines the stiffness in a tensegrity cellular structure, and ultimately resulted in the reduced stiffness. We conclude that the increase of stiffness in the second phase can find its roots in the initiation of the apoptosis pathway, which leads to the increased density of the filamentous structures of the cell, and thus stiffness. These hypothesis were verified by a series of experiments, and one of the important piece is to mimic the loss of adhesion by nanorobotic surgery.

9.1.3 Nanomechanical characterization and nanorobotic surgery delineate cell signaling pathway

The nanorobotic surgery severs the ties of the intermediate filaments between neighboring keratinocytes. The dissection processes were controlled at nanometer precision. We were able to monitor the snap of bundles of intermediate filaments by looking at the profile of the lateral force from the cantilever deflection during the nanorobotic surgery. The filamentous structures were imaged, sectioned and compared before and after surgery. We could confirm that the snap of the bundles were due to the severing force of the end-effector.

The repeated surgery operation could ultimately isolate a single cell from its neighbors, a physiological states similar with the antibody treatment, or non-formation of cellular adhesions. The isolation of cells, or the damage of the cell adhesion led to the decreased cellular stiffness, just as we expected. It verifies our conjecture that the cell behaves as a tensegrity structure, any single change at its cytoskeleton will trigger its active rearrangement globally. More importantly, the surgery operations that isolated cells did not lead to any increase of cellular stiffness. That, as we conclude should be a direct result of antibody-triggered, well-synchronized signaling pathways, apoptosis pathway in this case. Thus we set out to see whether we could find a quantitative method

of looking at signaling pathways from the mechanical measurements we took using the integrated platform, thus the transition from *mechano*phenotying to *mechano*proteomics.

9.1.4 Cell adhesion model with nanomechanical oscillator

To take a closer look at the cell adhesion at the basal area, we introduced into out platform a nanomechanical oscillator to detect the change of the cell-ECM adhesion strength during cellular events. The oscillator monitors the mechanical response from the bottom of the cell, while the AFM nanorobot takes measurement on the top. The result of the experiment showed a well synchronized profile from both measurement data. The A431 cell responded in a synchronized fashion temporally after the stimulation of EGF: the increased stiffness and increased hysteritivity from the AFM data, and the decreased energy dissipation from the oscillator. The profile pointed to us that the cell went through a transition that requires it to reduce its grasp onto the substrate underneath, while at the same time, direct its cytoskeleton to transit towards a more liquid like states.

A mechanical model of the cell adhesion structure interacting with the oscillating sensor was developed, with implications to the cytoskeleton. The model qualitatively evaluates the response from both data and analyzed the change of cell-ECM adhesion and the effect of this change on the actin filaments. We conclude that the reduced cell-ECM strength was due to the decreased number of integrin based bonds, integrin-RGD. The decreased force equilibrium led to the reduced energy dissipation level at each cycle of the oscillation. The loss of integrin bonds eventually led to the decreased cluster strength at the focal adhesion sites and thus broke the old force equilibrium between the focal adhesion and the actin filaments and established a new equilibrium at a lower force in the filaments. Quantitatively, the model provides the input and output relationship of the oscillation sensor to convert the molecular levels to the energy dissipation readouts that can be deduced for the comprehensive model of signaling pathway.

9.1.5 A systematic control model for cell signaling pathway

We think that these transition of cellular structure must have been orchestrated by the same EGF triggered pathway. Thus we took a systematic approach in the dissection of the signaling pathway. It employs the common concept of system identification process in a control practice. We took the input and output information and deduced the regulators in the middle. In our case, the input is the biochemical specie of EGF and the output is the mechanical readout of energy dissipation, a set of realtime quantitative data captured dynamically during the cellular transition process.

We consider the complex signaling network as the controller that regulates the mechanical behavior, or mechanical interaction of cells with the sensing elements. The pathway was modeled by the traditional differential equation approach and the plant is the mechanical model of the interaction between the adhesion bonds and the oscillator. We simulated a range of inputs from the EGF and look at the best fit with the experimental data to identify the key parameters in the signaling pathway. At these parameters, we looked at the levels of a few important regulating proteins, the rise and fall of levels of these molecules were identified and verified in literature during similar biological processes.

9.2 Future work

9.2.1 Signal transduction and propagation study

A key aspect of the signaling transduction is the intra- and intercellular signal propagation. For intracellular propagation, local concentrated EGF would cause dimmerization of EGFR, a signature reaction due to activation which would lead to downstream signaling events. Besides, this would trigger reactions from neighboring receptors, and thus a wave of dimerization would propagate

throughout the entire cell (Fig. 9.1A1,2). A study can be carried out to see whether the pathway can be triggered locally as by a AFM nanorobotic delivery of the EGF molecular to a specific location on the cell membrane (Fig. 9.1A3). We can also design experiments to test the signaling propagation through the physical contacts between neighboring cells. The study will tell us whether one stimulated cell will lead to the response from its neighbors, and whether the signal can be passed on to a large group of cells to provoke a synchronized response (Fig. 9.1B1,2).

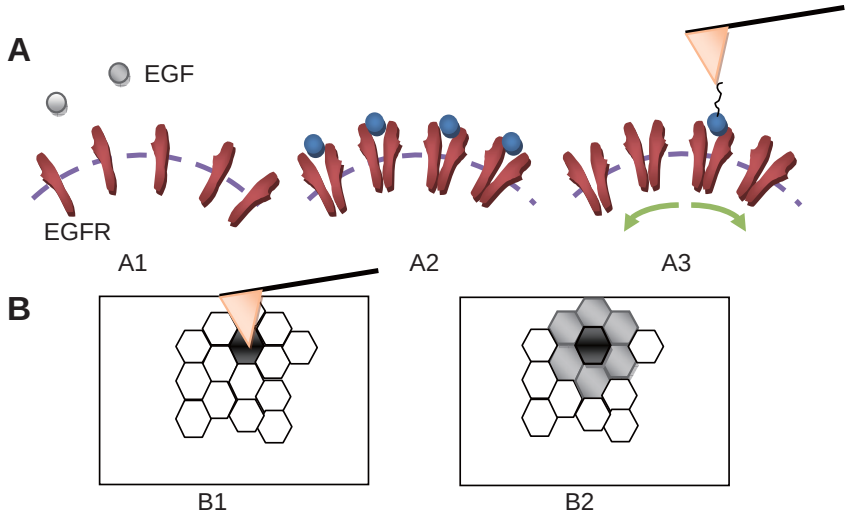

Figure 9.1 EGF stimulated intra and intercellular signaling propagation: A1, no activation; A2, global activation; A3, Local activation. B1, Local stimulation; B2, Intercellular propagation

9.2.2 Functional model of the pathway based on mechanical profile

A function model can be built to take the mechanical profile of any nature, elasticity, viscosity, energy dissipation, surface roughness and so on. The mechanical profile will work as a unified marker of physio/pathological events. An extension of the current signaling pathway model can be developed to take advantage of the unified maker and derive the molecular expressions of cellular events.

BIBLIOGRAPHY

BIBLIOGRAPHY

[1] Daniel J Müller and Yves F Dufrene. Atomic force microscopy as a multifunctional molecular toolbox in nanobiotechnology. *Nature nanotechnology*, 3(5):261–269, 2008.

[2] JKH Hörber and MJ Miles. Scanning probe evolution in biology. *Science*, 302(5647):1002–1005, 2003.

[3] Gerd Binnig, Calvin F Quate, and Ch Gerber. Atomic force microscope. *Physical review letters*, 56(9):930–933, 1986.

[4] Vladimir A Ukraintsev, Christopher Baum, Gary Zhang, and Craig L Hall. The role of afm in semiconductor technology development: the 65 nm technology node and beyond. In *Proc. SPIE*, volume 5752, pages 127–139, 2005.

[5] Todd D Krauss and Louis E Brus. Charge, polarizability, and photoionization of single semiconductor nanocrystals. *Physical Review Letters*, 83(23):4840–4843, 1999.

[6] Andre K Geim and Konstantin S Novoselov. The rise of graphene. *Nature materials*, 6(3):183–191, 2007.

[7] King Wai Chiu Lai, Carmen Kar Man Fung, Hongzhi Chen, Ruiguo Yang, Bo Song, and Ning Xi. Manipulation and assembly methods for graphene based nano devices. In *Nanotechnology (IEEE-NANO), 2010 10th IEEE Conference on*, pages 623–626. IEEE, 2010.

[8] Guangyong Li, Ning Xi, and Donna H Wang. In situ sensing and manipulation of molecules in biological samples using a nanorobotic system. *Nanomedicine: nanotechnology, biology, and medicine*, 1(1):31, 2005.

[9] Guangyong Li, Ning Xi, and Donna H Wang. Probing membrane proteins using atomic force microscopy. *Journal of cellular biochemistry*, 97(6):1191–1197, 2006.

[10] Carmen Kar Man Fung, Kristina Seiffert-Sinha, King Wai Chiu Lai, Ruiguo Yang, Dan Panyard, Jiangbo Zhang, Ning Xi, and Animesh A Sinha. Investigation of human keratinocyte cell adhesion using atomic force microscopy. *Nanomedicine: Nanotechnology, Biology and Medicine*, 6(1):191–200, 2010.

[11] Ruiguo Yang, Ning Xi, Carmen Kar, Man Fung, King Wai, Chiu Lai, K Seiffert-Sinha, and AA Sinha. Analysis of keratinocytes stiffness after desmosome disruption using atomic force microscopy based nanomanipulation. In *Nanotechnology, 2009. IEEE-NANO 2009. 9th IEEE Conference on*, pages 640–643. IEEE, 2009.

[12] Ruiguo Yang, Ning Xi, Carmen Kar Man Fung, King Wai Chiu Lai, Kristina Seiffert-Sinha, Animesh A Sinha, and Weijing Zhang. Investigations of bio markers for human lymphoblastoid cells using atomic force microscopy. In *Nano/Micro Engineered and Molecular Systems (NEMS), 2010 5th IEEE International Conference on*, pages 129–132. IEEE, 2010.

[13] Carmen Kar Man Fung, Ruiguo Yang, King Wai Chiu Lai, Ning Xi, K Seiffert-Sinha, and AA Sinha. Micro fixture enabled in-situ imaging and manipulation of cell membrane protein. In *Nano/Micro Engineered and Molecular Systems (NEMS), 2010 5th IEEE International Conference on*, pages 165–168. IEEE, 2010.

[14] Daniel J Muller. Afm: A nanotool in membrane biology. *Biochemistry*, 47(31):7986–7998, 2008.

[15] Guangyong Li, Ning Xi, Lianqing Liu, Jiangbo Zhang, and K Lai. Study of dna properties under controlled conditions using afm based nano-robotics. In *Nanotechnology, 2007. IEEE-NANO 2007. 7th IEEE Conference on*, pages 1018–1021. IEEE, 2007.

[16] Andreas Engel and Daniel J Müller. Observing single biomolecules at work with the atomic force microscope. *Nature Structural & Molecular Biology*, 7(9):715–718, 2000.

[17] King Wai Chui Lai, Ning Xi, Carmen Kar Man Fung, Jiangbo Zhang, Hongzhi Chen, Yilun Luo, and Uchechukwu C Wejinya. Automated nanomanufacturing system to assemble carbon nanotube based devices. *The International Journal of Robotics Research*, 28(4):523–536, 2009.

[18] Sébastien Decossas, Frédéric Mazen, Thierry Baron, Georges Brémond, and Abdelkader Souifi. Atomic force microscopy nanomanipulation of silicon nanocrystals for nanodevice fabrication. *Nanotechnology*, 14(12):1272, 2003.

[19] Ning Xi, CKM Fung, Ruiguo Yang, Kristina Seiffert-Sinha, King Wai Chiu Lai, and Animesh A Sinha. Bionanomanipulation using atomic force microscopy. *Nanotechnology Magazine, IEEE*, 4(1):9–12, 2010.

[20] Harald Herrmann, Harald Bär, Laurent Kreplak, Sergei V Strelkov, and Ueli Aebi. Intermediate filaments: from cell architecture to nanomechanics. *Nature Reviews Molecular Cell Biology*, 8(7):562–573, 2007.

[21] JD Beard, DJ Burbridge, AV Moskalenko, O Dudko, Polina L Yarova, SV Smirnov, and SN Gordeev. An atomic force microscope nanoscalpel for nanolithography and biological applications. *Nanotechnology*, 20(44):445302, 2009.

[22] Matthias Rief, Filipp Oesterhelt, Berthold Heymann, and Hermann E Gaub. Single molecule force spectroscopy on polysaccharides by atomic force microscopy. *Science*, 275(5304):1295–1297, 1997.

[23] Keir C Neuman and Attila Nagy. Single-molecule force spectroscopy: optical tweezers, magnetic tweezers and atomic force microscopy. *Nature methods*, 5(6):491–505, 2008.

[24] Andrew E Pelling, Farlan S Veraitch, Carol Pui-Kei Chu, Chris Mason, and Michael A Horton. Mechanical dynamics of single cells during early apoptosis. *Cell motility and the cytoskeleton*, 66(7):409–422, 2009.

[25] Dimitrios Fotiadis, Simon Scheuring, Shirley A Müller, Andreas Engel, and Daniel J Müller. Imaging and manipulation of biological structures with the afm. *Micron*, 33(4):385–397, 2002.

[26] PK Hansma, JP Cleveland, M Radmacher, DA Walters, PE Hillner, M Bezanilla, M Fritz, D Vie, HG Hansma, CB Prater, et al. Tapping mode atomic force microscopy in liquids. *Applied Physics Letters*, 64(13):1738–1740, 1994.

[27] Simon Scheuring and Yves F Dufrêne. Atomic force microscopy: probing the spatial organization, interactions and elasticity of microbial cell envelopes at molecular resolution. *Molecular microbiology*, 75(6):1327–1336, 2010.

[28] QS Li, GYH Lee, CN Ong, and CT Lim. Afm indentation study of breast cancer cells. *Biochemical and biophysical research communications*, 374(4):609–613, 2008.

[29] Martin Stolz, Riccardo Gottardi, Roberto Raiteri, Sylvie Miot, Ivan Martin, Raphaël Imer, Urs Staufer, Aurelia Raducanu, Marcel Düggelin, Werner Baschong, et al. Early detection of aging cartilage and osteoarthritis in mice and patient samples using atomic force microscopy. *Nature nanotechnology*, 4(3):186–192, 2009.

[30] Andrew Hards, Chunqing Zhou, Markus Seitz, Christoph Bräuchle, and Andreas Zumbusch. Simultaneous afm manipulation and fluorescence imaging of single dna strands. *ChemPhysChem*, 6(3):534–540, 2005.

[31] Chiara Callies, Peter Schön, Ivan Liashkovich, Christian Stock, Kristina Kusche-Vihrog, Johannes Fels, Alexandra S Sträter, and Hans Oberleithner. Simultaneous mechanical stiffness

and electrical potential measurements of living vascular endothelial cells using combined atomic force and epifluorescence microscopy. *Nanotechnology*, 20(17):175104, 2009.

[32] Christoph Riethmüller, Tilman E Schäffer, Ferry Kienberger, Werner Stracke, and Hans Oberleithner. Vacuolar structures can be identified by afm elasticity mapping. *Ultramicroscopy*, 107(10):895–901, 2007.

[33] Michael J Rust, Mark Bates, and Xiaowei Zhuang. Stochastic optical reconstruction microscopy (storm) provides sub-diffraction-limit image resolution. *Nature methods*, 3(10):793, 2006.

[34] Susana Moreno Flores and José L Toca-Herrera. The new future of scanning probe microscopy: Combining atomic force microscopy with other surface-sensitive techniques, optical microscopy and fluorescence techniques. *Nanoscale*, 1(1):40–49, 2009.

[35] Gennaro Picardi, Marc Chaigneau, Razvigor Ossikovski, Christophe Licitra, and Guillame Delapierre. Tip enhanced raman spectroscopy on azobenzene thiol self-assembled monolayers on au (111). *Journal of Raman Spectroscopy*, 40(10):1407–1412, 2009.

[36] Philip S Waggoner and Harold G Craighead. Micro-and nanomechanical sensors for environmental, chemical, and biological detection. *Lab on a Chip*, 7(10):1238–1255, 2007.

[37] Martino Poggio. Nanomechanics: Sensing from the bottom up. *Nature nanotechnology*, 8(7):482–483, 2013.

[38] Gajendra S Shekhawat and Vinayak P Dravid. Nanomechanical sensors: Bent on detecting cancer. *Nature nanotechnology*, 8(2):77–78, 2013.

[39] Hans Peter Lang, Martin Hegner, and Christoph Gerber. Cantilever array sensors. *Materials today*, 8(4):30–36, 2005.

[40] F Huber, HP Lang, N Backmann, D Rimoldi, and Ch Gerber. Direct detection of a braf mutation in total rna from melanoma cells using cantilever arrays. *Nature nanotechnology*, 8(2):125–129, 2013.

[41] G Longo, L Alonso-Sarduy, L Marques Rio, A Bizzini, A Trampuz, J Notz, G Dietler, and S Kasas. Rapid detection of bacterial resistance to antibiotics using afm cantilevers as nanomechanical sensors. *Nature nanotechnology*, 8(7):522–526, 2013.

[42] Montserrat Calleja, Priscila M Kosaka, Álvaro San Paulo, and Javier Tamayo. Challenges for nanomechanical sensors in biological detection. *Nanoscale*, 4(16):4925–4938, 2012.

[43] Christian Franck, Stacey A Maskarinec, David A Tirrell, and Guruswami Ravichandran. Three-dimensional traction force microscopy: a new tool for quantifying cell-matrix interactions. *PLoS One*, 6(3):e17833, 2011.

[44] Venkat Maruthamuthu, Benedikt Sabass, Ulrich S Schwarz, and Margaret L Gardel. Cell-ecm traction force modulates endogenous tension at cell–cell contacts. *Proceedings of the National Academy of Sciences*, 108(12):4708–4713, 2011.

[45] Jianping Fu, Yang-Kao Wang, Michael T Yang, Ravi A Desai, Xiang Yu, Zhijun Liu, and Christopher S Chen. Mechanical regulation of cell function with geometrically modulated elastomeric substrates. *Nature methods*, 7(9):733–736, 2010.

[46] Adam J Engler, Shamik Sen, H Lee Sweeney, and Dennis E Discher. Matrix elasticity directs stem cell lineage specification. *Cell*, 126(4):677–689, 2006.

[47] Fredrik Höök and Bengt Kasemo. The qcm-d technique for probing biomacromolecular recognition reactions. In *Piezoelectric Sensors*, pages 425–447. Springer, 2007.

[48] Malin Edvardsson, Michael Rodahl, and Fredrik Höök. Investigation of binding event perturbations caused by elevated qcm-d oscillation amplitude. *Analyst*, 131(7):822–828, 2006.

[49] Karin Glasmästar, Charlotte Larsson, Fredrik Höök, and Bengt Kasemo. Protein adsorption on supported phospholipid bilayers. *Journal of colloid and interface science*, 246(1):40–47, 2002.

[50] Carine Galli Marxer, Martine Collaud Coen, Thomas Greber, Urs F Greber, and Louis Schlapbach. Cell spreading on quartz crystal microbalance elicits positive frequency shifts indicative of viscosity changes. *Analytical and bioanalytical chemistry*, 377(3):578–586, 2003.

[51] Marina V Voinova, M Rodahl, M Jonson, and B Kasemo. Viscoelastic acoustic response of layered polymer films at fluid-solid interfaces: Continuum mechanics approach. *Physica Scripta*, 59(5):391, 1999.

[52] Shannon M Notley, Malin Eriksson, and Lars Wågberg. Visco-elastic and adhesive properties of adsorbed polyelectrolyte multilayers determined in situ with qcm-d and afm measurements. *Journal of colloid and interface science*, 292(1):29–37, 2005.

[53] L Kreplak, H Bär, JF Leterrier, H Herrmann, and U Aebi. Exploring the mechanical behavior of single intermediate filaments. *Journal of molecular biology*, 354(3):569–577, 2005.

[54] Aleksandr Noy. *Handbook of molecular force spectroscopy*. Springer, 2008.

[55] Graham Carpenter and Stanley Cohen. Epidermal growth factor. *Annual review of biochemistry*, 48(1):193–216, 1979.

[56] Sreenath V Sharma, Daphne W Bell, Jeffrey Settleman, and Daniel A Haber. Epidermal growth factor receptor mutations in lung cancer. *Nature Reviews Cancer*, 7(3):169–181, 2007.

[57] Kanae Oda, Yukiko Matsuoka, Akira Funahashi, and Hiroaki Kitano. A comprehensive pathway map of epidermal growth factor receptor signaling. *Molecular systems biology*, 1(1), 2005.

[58] Zhimin Lu, Guoqiang Jiang, Peter Blume-Jensen, and Tony Hunter. Epidermal growth factor-induced tumor cell invasion and metastasis initiated by dephosphorylation and downregulation of focal adhesion kinase. *Molecular and cellular biology*, 21(12):4016–4031, 2001.

[59] Michele A Wozniak, Katarzyna Modzelewska, Lina Kwong, and Patricia J Keely. Focal adhesion regulation of cell behavior. *Biochimica et Biophysica Acta (BBA)-Molecular Cell Research*, 1692(2):103–119, 2004.

[60] George I Bell. Models for the specific adhesion of cells to cells. *Science*, 200(4342):618–627, 1978.

[61] M Dembo, DC Torney, K Saxman, and D Hammer. The reaction-limited kinetics of membrane-to-surface adhesion and detachment. *Proceedings of the Royal Society of London. Series B. Biological Sciences*, 234(1274):55–83, 1988.

[62] Salvatore Pece and J Silvio Gutkind. Signaling from e-cadherins to the mapk pathway by the activation of epidermal growth factor receptors upon cell-cell contact formation. *Journal of Biological Chemistry*, 275(52):41227–41233, 2000.

[63] Elizabeth J Joslin, Harish Shankaran, Lee K Opresko, Nikki Bollinger, Douglas A Lauffenburger, and H Steven Wiley. Structure of the egf receptor transactivation circuit integrates multiple signals with cell context. *Molecular BioSystems*, 6(7):1293–1306, 2010.

[64] Melody K Morris, Julio Saez-Rodriguez, David C Clarke, Peter K Sorger, and Douglas A Lauffenburger. Training signaling pathway maps to biochemical data with constrained fuzzy logic: quantitative analysis of liver cell responses to inflammatory stimuli. *PLoS computational biology*, 7(3):e1001099, 2011.

[65] Neda Bagheri, Marisa Shiina, Douglas A Lauffenburger, and W Michael Korn. A dynamical systems model for combinatorial cancer therapy enhances oncolytic adenovirus efficacy by mek-inhibition. *PLoS computational biology*, 7(2):e1001085, 2011.

[66] Achim Besser and Ulrich S Schwarz. Coupling biochemistry and mechanics in cell adhesion: a model for inhomogeneous stress fiber contraction. *New Journal of Physics*, 9(11):425, 2007.

[67] Ruiguo Yang, Jennifer Y Chen, Ning Xi, King Wai Chiu Lai, Chengeng Qu, Carmen Kar Man Fung, Lynn S Penn, and Jun Xi. Characterization of mechanical behavior of an epithelial monolayer in response to epidermal growth factor stimulation. *Experimental cell research*, 318(5):521–526, 2012.

[68] Jennifer Y Chen, Ammar Shahid, Marcela P Garcia, Lynn S Penn, and Jun Xi. Dissipation monitoring for assessing egf-induced changes of cell adhesion. *Biosensors and Bioelectronics*, 38(1):375–381, 2012.

[69] Toshio Ando, Noriyuki Kodera, Daisuke Maruyama, Eisuke Takai, Kiwamu Saito, and Akitoshi Toda. A high-speed atomic force microscope for studying biological macromolecules in action. *Japanese Journal of Applied Physics*, 41(part 1):4851–4856, 2002.

[70] H Xie, DS Haliyo, and S Régnier. Parallel imaging/manipulation force microscopy. *Applied Physics Letters*, 94(15):153106–153106, 2009.

[71] Yoomin Ahn, Takahito Ono, and Masayoshi Esashi. Micromachined si cantilever arrays for parallel afm operation. *Journal of Mechanical Science and Technology*, 22(2):308–311, 2008.

[72] Atsushi Ikai. *The world of nano-biomechanics: mechanical imaging and measurement by atomic force microscopy*. Access Online via Elsevier, 2007.

[73] H Hatze. The meaning of the term biomechanics. *Journal of Biomechanics*, 7(2):189–190, 1974.

[74] Michael Fitzgerald. Nanobiomechanics". technology review. mit. retrieved february 23, February 20011.

[75] Brian M Cooke, Narla Mohandas, and Ross L Coppel. The malaria-infected red blood cell: structural and functional changes. *Advances in parasitology*, 50:1–86, 2001.

[76] Sarah E Cross, Yu-Sheng Jin, Jianyu Rao, and James K Gimzewski. Nanomechanical analysis of cells from cancer patients. *Nature nanotechnology*, 2(12):780–783, 2007.

[77] Kathryn Rosowski. Introduction to cell mechanics and mechanobiology. *The Yale journal of biology and medicine*, 86(3):436, 2013.

[78] Bernd W Koenig, Helmut H Strey, and Klaus Gawrisch. Membrane lateral compressibility determined by nmr and x-ray diffraction: effect of acyl chain polyunsaturation. *Biophysical journal*, 73(4):1954–1966, 1997.

[79] Daniel Reeves, Tristan Ursell, Pierre Sens, Jane Kondev, and Rob Phillips. Membrane mechanics as a probe of ion-channel gating mechanisms. *Physical Review E*, 78(4):041901, 2008.

[80] Debbie C Thurmond. Insulin-regulated glucagon-like peptide-1 release from l cells: actinout. *Endocrinology*, 150(12):5202–5204, 2009.

[81] Chauying J Jen, Shuo-Ju Jhiang, and Hsiun-Ing Chen. Invited review: effects of flow on vascular endothelial intracellular calcium signaling of rat aortas ex vivo. *Journal of Applied Physiology*, 89(4):1657–1662, 2000.

[82] Martin A Schwartz and Mark H Ginsberg. Networks and crosstalk: integrin signalling spreads. *Nature Cell Biology*, 4(4):E65–E68, 2002.

[83] CT Lim, EH Zhou, and ST Quek. Mechanical models for living cellsa review. *Journal of biomechanics*, 39(2):195–216, 2006.

[84] Donald E Ingber. Tensegrity: the architectural basis of cellular mechanotransduction. *Annual review of physiology*, 59(1):575–599, 1997.

[85] Donald E Ingber. Tensegrity i. cell structure and hierarchical systems biology. *Journal of Cell Science*, 116(7):1157–1173, 2003.

[86] J Li, M Dao, CT Lim, and S Suresh. Spectrin-level modeling of the cytoskeleton and optical tweezers stretching of the erythrocyte. *Biophysical Journal*, 88(5):3707–3719, 2005.

[87] Olivier Thoumine and Albrecht Ott. Time scale dependent viscoelastic and contractile regimes in fibroblasts probed by microplate manipulation. *Journal of cell science*, 110(17):2109–2116, 1997.

[88] A Yeung and E Evans. Cortical shell-liquid core model for passive flow of liquid-like spherical cells into micropipets. *Biophysical journal*, 56(1):139–149, 1989.

[89] Philippe Carl and Hermann Schillers. Elasticity measurement of living cells with an atomic force microscope: data acquisition and processing. *Pflügers Archiv-European Journal of Physiology*, 457(2):551–559, 2008.

[90] RE Mahaffy, S Park, E Gerde, J Käs, and CK Shih. Quantitative analysis of the viscoelastic properties of thin regions of fibroblasts using atomic force microscopy. *Biophysical journal*, 86(3):1777–1793, 2004.

[91] Nan Yang, Kenneth Kar Ho Wong, John R de Bruyn, and Jeffrey L Hutter. Frequency-dependent viscoelasticity measurement by atomic force microscopy. *Measurement Science and Technology*, 20(2):025703, 2009.

[92] Bruce Alberts, Dennis Bray, Julian Lewis, Martin Raff, Keith Roberts, and James D Watson. Molecular biology of the cell. 1994. *Garland, New York*.

[93] Ning Wang, Iva Marija Tolić-Nørrelykke, Jianxin Chen, Srboljub M Mijailovich, James P Butler, Jeffrey J Fredberg, and Dimitrije Stamenović. Cell prestress. i. stiffness and prestress are closely associated in adherent contractile cells. *American Journal of Physiology-Cell Physiology*, 282(3):C606–C616, 2002.

[94] JM Mitchison and MM Swann. The mechanical properties of the cell surface i. the cell elastimeter. *Journal of Experimental Biology*, 31(3):443–460, 1954.

[95] CT Lim, M Dao, S Suresh, CH Sow, and KT Chew. Large deformation of living cells using laser traps. *Acta Materialia*, 52(7):1837–1845, 2004.

[96] Geoffrey N Maksym, Ben Fabry, James P Butler, Daniel Navajas, Daniel J Tschumperlin, Johanne D Laporte, and Jeffrey J Fredberg. Mechanical properties of cultured human airway smooth muscle cells from 0.05 to 0.4 hz. *Journal of Applied Physiology*, 89(4):1619–1632, 2000.

[97] Sung Woong Han, Chikashi Nakamura, Ikuo Obataya, Noriyuki Nakamura, and Jun Miyake. A molecular delivery system by using afm and nanoneedle. *Biosensors and Bioelectronics*, 20(10):2120–2125, 2005.

[98] Steven D Hughes, Christian Quaade, John H Johnson, Sarah Ferber, and CB Newgard. Transfection of att-20ins cells with glut-2 but not glut-1 confers glucose-stimulated insulin secretion. relationship to glucose metabolism. *Journal of Biological Chemistry*, 268(20):15205–15212, 1993.

[99] George G Holz. Epac: a new camp-binding protein in support of glucagon-like peptide-1 receptor-mediated signal transduction in the pancreatic β-cell. *Diabetes*, 53(1):5–13, 2004.

[100] Martin D Meglasson and Franz M Matschinsky. Pancreatic islet glucose metabolism and regulation of insulin secretion. *Diabetes/metabolism reviews*, 2(3-4):163–214, 1986.

[101] Daniel L Cook and Nicholas Hales. Intracellular atp directly blocks k+ channels in pancreatic b-cells. 1984.

[102] LS Satin and DL Cook. Voltage-gated ca2+ current in pancreatic b-cells. *Pflügers Archiv*, 404(4):385–387, 1985.

[103] P Rorsman. The pancreatic beta-cell as a fuel sensor: an electrophysiologist's viewpoint. *Diabetologia*, 40(5):487–495, 1997.

[104] Susanne G Straub and Geoffrey WG Sharp. Glucose-stimulated signaling pathways in biphasic insulin secretion. *Diabetes/metabolism research and reviews*, 18(6):451–463, 2002.

[105] Mica Ohara-Imaizumi, Tomonori Fujiwara, Yoko Nakamichi, Tadashi Okamura, Yoshihiro Akimoto, Junko Kawai, Satsuki Matsushima, Hayato Kawakami, Takashi Watanabe, Kimio Akagawa, et al. Imaging analysis reveals mechanistic differences between first-and second-phase insulin exocytosis. *The Journal of cell biology*, 177(4):695–705, 2007.

[106] Michael J Caterina, Mark A Schumacher, Makoto Tominaga, Tobias A Rosen, Jon D Levine, and David Julius. The capsaicin receptor: a heat-activated ion channel in the pain pathway. *Nature*, 389(6653):816–824, 1997.

[107] Arpad Szallasi, Daniel N Cortright, Charles A Blum, and Samer R Eid. The vanilloid receptor trpv1: 10 years from channel cloning to antagonist proof-of-concept. *Nature Reviews Drug Discovery*, 6(5):357–372, 2007.

[108] Pablo Juan-Picó, Esther Fuentes, F Javier Bermudez-Silva, F Javier Diaz-Molina, Cristina Ripoll, Fernando Rodríguez de Fonseca, and Angel Nadal. Cannabinoid receptors regulate ca¡ sup¿ 2+¡/sup¿ signals and insulin secretion in pancreatic β-cell. *Cell calcium*, 39(2):155–162, 2006.

[109] Luciano De Petrocellis, Pietro Marini, Isabel Matias, Aniello Schiano Moriello, Katarzyna Starowicz, Luigia Cristino, Santosh Nigam, and Vincenzo Di Marzo. Mechanisms for the coupling of cannabinoid receptors to intracellular calcium mobilization in rat insulinoma β-cells. *Experimental cell research*, 313(14):2993–3004, 2007.

[110] Sven Karlsson, AJ Scheurink, Anton B Steffens, and Bo Ahrén. Involvement of capsaicin-sensitive nerves in regulation of insulin secretion and glucose tolerance in conscious

mice. *American Journal of Physiology-Regulatory, Integrative and Comparative Physiology*, 267(4):R1071–R1077, 1994.

[111] Jooyoung Jung, Sun Wook Hwang, Jiyeon Kwak, Soon-Youl Lee, Chang-Joong Kang, Won Bae Kim, Donghee Kim, and Uhtaek Oh. Capsaicin binds to the intracellular domain of the capsaicin-activated ion channel. *The Journal of neuroscience*, 19(2):529–538, 1999.

[112] Sven-Eric Jordt and David Julius. Molecular basis for species-specific sensitivity to hot chili peppers. *Cell*, 108(3):421–430, 2002.

[113] Tatyana G Kuznetsova, Maria N Starodubtseva, Nicolai I Yegorenkov, Sergey A Chizhik, and Renat I Zhdanov. Atomic force microscopy probing of cell elasticity. *Micron*, 38(8):824–833, 2007.

[114] Y Akiba, S Kato, K Katsube, M Nakamura, K Takeuchi, H Ishii, and T Hibi. Transient receptor potential vanilloid subfamily 1 expressed in pancreatic islet beta cells modulates insulin secretion in rats. *BIOCHEMICAL AND BIOPHYSICAL RESEARCH COMMUNICATIONS*, 321(1):219–225, AUG 11 2004.

[115] CE Lewis, A Clark, SJH Ashcroft, GJS Cooper, and JF Morris. Calcitonin gene-related peptide and somatostatin inhibit insulin release from individual rat b cells. *Molecular and cellular endocrinology*, 57(1):41–49, 1988.

[116] JF O'Neill, RC Johnston, L Halferty, GP Brennan, J Keiser, I Fairweather, et al. Adult triclabendazole-resistant fasciola hepatica: morphological changes in the tegument and gut following in vivo treatment with artemether in the rat model. *Journal of helminthology*, 83(2):151, 2009.

[117] WILLY J Malaisse, Abdullah Sener, MAJDA Koser, M Ravazzola, and F Malaisse-Lagae. The stimulus-secretion coupling of glucose-induced insulin release. insulin release due to glycogenolysis in glucose-deprived islets. *Biochem. J*, 164:447–454, 1977.

[118] Zhanxiang Wang, Eunjin Oh, and Debbie C Thurmond. Glucose-stimulated cdc42 signaling is essential for the second phase of insulin secretion. *Journal of Biological Chemistry*, 282(13):9536–9546, 2007.

[119] Zhanxiang Wang and Debbie C Thurmond. Mechanisms of biphasic insulin-granule exocytosis–roles of the cytoskeleton, small gtpases and snare proteins. *Journal of cell science*, 122(7):893–903, 2009.

[120] Yoichi Hamada, Hiroshi Ikegami, Hironori Ueda, Yoshihiko Kawaguchi, Eiji Yamato, Koji Nojima, Kazunori Yamada, Naru Babaya, Masao Shibata, and Toshio Ogihara. Insulin secretion to glucose as well as nonglucose stimuli is impaired in spontaneously diabetic nagoya-shibata-yasuda mice. *Metabolism*, 50(11):1282–1285, 2001.

[121] Seigo Fujimoto, Mayumi Mori, Hiromi Tsushima, and Mitoshi Kunimatsu. Capsaicin-induced, capsazepine-insensitive relaxation of the guinea-pig ileum. *European journal of pharmacology*, 530(1):144–151, 2006.

[122] Frances M Ashcroft and Patrik Rorsman. Electrophysiology of the pancreatic β-cell. *Progress in biophysics and molecular biology*, 54(2):87–143, 1989.

[123] Patrik Rorsman, Lena Eliasson, Takahiro Kanno, Quan Zhang, and Sven Gopel. Electrophysiology of pancreatic β-cells in intact mouse islets of langerhans. *Progress in biophysics and molecular biology*, 107(2):224–235, 2011.

[124] S Gopel, Q Zhang, L Eliasson, XS Ma, J Galvanovskis, T Kanno, A Salehi, and P Rorsman. Capacitance measurements of exocytosis in mouse pancreatic alpha-, beta- and delta-cells within intact islets of Langerhans. *JOURNAL OF PHYSIOLOGY-LONDON*, 556(3):711–726, MAY 1 2004.

[125] Arthur Beyder and Frederick Sachs. Electromechanical coupling in the membranes of shaker-transfected hek cells. *Proceedings of the National Academy of Sciences*, 106(16):6626–6631, 2009.

[126] Dong-Qi Tang, Li-Zhen Cao, Brant R Burkhardt, Chang-Qi Xia, Sally A Litherland, Mark A Atkinson, and Li-Jun Yang. In vivo and in vitro characterization of insulin-producing cells obtained from murine bone marrow. *Diabetes*, 53(7):1721–1732, 2004.

[127] Jean-Claude Henquin, Myriam Nenquin, Patrick Stiernet, and Bo Ahren. In vivo and in vitro glucose-induced biphasic insulin secretion in the mouse pattern and role of cytoplasmic ca2+ and amplification signals in β-cells. *Diabetes*, 55(2):441–451, 2006.

[128] BA Becker and AA Gaspari. Pemphigus vulgaris and vegetans. *Dermatologic clinics*, 11(3):429, 1993.

[129] Ken Ishii, Reiko Harada, Itsuro Matsuo, Yuji Shirakata, Koji Hashimoto, and Masayuki Amagai. In vitro keratinocyte dissociation assay for evaluation of the pathogenicity of anti-desmoglein 3 igg autoantibodies in pemphigus vulgaris. *Journal of investigative dermatology*, 124(5):939–946, 2005.

[130] Grant J Anhalt, Ramzy S Labib, John J Voorhees, Theodore F Beals, and Luis A Diaz. Induction of pemphigus in neonatal mice by passive transfer of igg from patients with the disease. *The New England journal of medicine*, 306(20):1189, 1982.

[131] Aimee S Payne, Don L Siegel, and John R Stanley. Targeting pemphigus autoantibodies through their heavy-chain variable region genes. *Journal of Investigative Dermatology*, 127(7):1681–1691, 2007.

[132] Marilyn G Farquhar and George E Palade. Junctional complexes in various epithelia. *The Journal of cell biology*, 17(2):375–412, 1963.

[133] Anthea Scothern and David Garrod. Visualization of desmosomes in the electron microscope. *Methods in cell biology*, 88:347–366, 2008.

[134] George F Obland. The fine structure of the interrelationship of cells in the human epidermis. *The Journal of biophysical and biochemical cytology*, 4(5):529–538, 1958.

[135] Hiroshi Shimizu, Takuji Masunaga, Akira Ishiko, Arata Kikuchi, Takashi Hashimoto, and Takeji Nishikawa. Pemphigus vulgaris and pemphigus foliaceus sera show an inversely graded binding pattern to extracellular regions of desmosomes in different layers of human epidermis. *Journal of investigative dermatology*, 105(2):153–159, 1995.

[136] Xuming Mao, Eun Jung Choi, and Aimee S Payne. Disruption of desmosome assembly by monovalent human pemphigus vulgaris monoclonal antibodies. *Journal of Investigative Dermatology*, 129(4):908–918, 2008.

[137] Paula Berkowitz, Peiqi Hu, Zhi Liu, Luis A Diaz, Jan J Enghild, Michael P Chua, and David S Rubenstein. Desmosome signaling inhibition of p38mapk prevents pemphigus vulgaris igg-induced cytoskeleton reorganization. *Journal of Biological Chemistry*, 280(25):23778–23784, 2005.

[138] Subra Suresh. Nanomedicine: Elastic clues in cancer detection. *Nature nanotechnology*, 2(12):748–749, 2007.

[139] Wilbur A Lam, Michael J Rosenbluth, and Daniel A Fletcher. Chemotherapy exposure increases leukemia cell stiffness. *Blood*, 109(8):3505–3508, 2007.

[140] Tomomi E Kimura, Anita J Merritt, and David R Garrod. Calcium-independent desmosomes of keratinocytes are hyper-adhesive. *Journal of Investigative Dermatology*, 127(4):775–781, 2006.

[141] Jens Waschke. The desmosome and pemphigus. *Histochemistry and cell biology*, 130(1):21–54, 2008.

[142] Yuzo Takahashi, Harish P Patel, Ramzy S Labib, Luis A Diaz, and Grant J Anhalt. Experimentally induced pemphigus vulgaris in neonatal balb/c mice: a time-course study of clinical, immunologic, ultrastructural, and cytochemical changes. *Journal of investigative dermatology*, 84(1):41–46, 1985.

[143] Aimee S Payne, Ken Ishii, Stephen Kacir, Chenyan Lin, Hong Li, Yasushi Hanakawa, Kazuyuki Tsunoda, Masayuki Amagai, John R Stanley, Don L Siegel, et al. Genetic and functional characterization of human pemphigus vulgaris monoclonal autoantibodies isolated by phage display. *Journal of Clinical Investigation*, 115(4):888–899, 2005.

[144] Alex I Chernyavsky, Juan Arredondo, Yasuo Kitajima, Miki Sato-Nagai, and Sergei A Grando. Desmoglein versus non-desmoglein signaling in pemphigus acantholysis characterization of novel signaling pathways downstream of pemphigus vulgaris antigens. *Journal of Biological Chemistry*, 282(18):13804–13812, 2007.

[145] Enno Schmidt and Jens Waschke. Apoptosis in pemphigus. *Autoimmunity reviews*, 8(7):533, 2009.

[146] Beatriz Pelacho, Cristina Natal, Agustín España, I Sanchez-Carpintero, María J Iraburu, and María Jesús Lopez-Zabalza. Pemphigus vulgaris autoantibodies induce apoptosis in hacat keratinocytes. *FEBS letters*, 566(1):6–10, 2004.

[147] HL Tang, KL Yuen, HM Tang, and MC Fung. Reversibility of apoptosis in cancer cells. *British journal of cancer*, 100(1):118–122, 2008.

[148] Karin Fischer, Simon Voelkl, Jana Berger, Reinhard Andreesen, Thomas Pomorski, and Andreas Mackensen. Antigen recognition induces phosphatidylserine exposure on the cell surface of human cd8+ t cells. *Blood*, 108(13):4094–4101, 2006.

[149] Marcus Lettau, Maren Paulsen, Hendrik Schmidt, and Ottmar Janssen. Insights into the molecular regulation of fasl (cd178) biology. *European Journal of Cell Biology*, 90(6):456–466, 2011.

[150] Mario Puviani, Alessandra Marconi, Emanuele Cozzani, and Carlo Pincelli. Fas ligand in pemphigus sera induces keratinocyte apoptosis through the activation of caspase-8. *Journal of investigative dermatology*, 120(1):164–167, 2003.

[151] MG Pacheco-Tovar, E Avalos-Díaz, E Vega-Memije, JJ Bollain-y Goytia, E López-Robles, MT Hojyo-Tomoka, L Domínguez-Soto, and R Herrera-Esparza. The final destiny of acan-

tholytic cells in pemphigus is fas mediated. *Journal of the European Academy of Dermatology and Venereology*, 23(6):697–701, 2009.

[152] MARINA FRUŠIĆ-ZLOTKIN, Rochel Pergamentz, Beno Michel, Michael David, Daniel Mimouni, François Brégégère, and Yoram Milner. The interaction of pemphigus autoimmunoglobulins with epidermal cells: activation of the fas apoptotic pathway and the use of caspase activity for pathogenicity tests of pemphigus patients. *Annals of the New York Academy of Sciences*, 1050(1):371–379, 2005.

[153] Vu Thuong Nguyen, Assane Ndoye, Leonard D Shultz, Mark R Pittelkow, Sergei A Grando, et al. Antibodies against keratinocyte antigens other than desmogleins 1 and 3 can induce pemphigus vulgaris–like lesions. *Journal of Clinical Investigation*, 106(12):1467–1479, 2000.

[154] X Wang, F Bregegere, M Frušić-Zlotkin, M Feinmesser, B Michel, and Y Milner. Possible apoptotic mechanism in epidermal cell acantholysis induced by pemphigus vulgaris autoimmunoglobulins. *Apoptosis*, 9(2):131–143, 2004.

[155] Jörg Weiske, Torsten Schöneberg, Werner Schröder, Mechthild Hatzfeld, Rudolf Tauber, and Otmar Huber. The fate of desmosomal proteins in apoptotic cells. *Journal of Biological Chemistry*, 276(44):41175–41181, 2001.

[156] Claudio Brancolini, Andrea Sgorbissa, Claudio Schneider, et al. Proteolytic processing of the adherens junctions components beta-catenin and gamma-catenin/plakoglobin during apoptosis. *Cell death and differentiation*, 5(12):1042, 1998.

[157] Atsushi Shimizu, Akira Ishiko, Takayuki Ota, Kazuyuki Tsunoda, Masayuki Amagai, and Takeji Nishikawa. Igg binds to desmoglein 3 in desmosomes and causes a desmosomal split without keratin retraction in a pemphigus mouse model. *Journal of investigative dermatology*, 122(5):1145–1153, 2004.

[158] Wolfgang-Moritz Heupel, Detlef Zillikens, Detlev Drenckhahn, and Jens Waschke. Pemphigus vulgaris igg directly inhibit desmoglein 3-mediated transinteraction. *The Journal of Immunology*, 181(3):1825–1834, 2008.

[159] Cathárine C Calkins, Shannon V Setzer, Jean Marie Jennings, Susan Summers, Kazuyuki Tsunoda, Masayuki Amagai, and Andrew P Kowalczyk. Desmoglein endocytosis and desmosome disassembly are coordinated responses to pemphigus autoantibodies. *Journal of Biological Chemistry*, 281(11):7623–7634, 2006.

[160] Xuming Mao, Yasuyo Sano, Jin Mo Park, and Aimee S Payne. p38 mapk activation is downstream of the loss of intercellular adhesion in pemphigus vulgaris. *Journal of Biological Chemistry*, 286(2):1283–1291, 2011.

[161] Sergei A Grando, Jean-Claude Bystryn, Alexander I Chernyavsky, Marina Frušić-Zlotkin, Robert Gniadecki, Roberta Lotti, Yoram Milner, Mark R Pittelkow, and Carlo Pincelli. Apoptolysis: a novel mechanism of skin blistering in pemphigus vulgaris linking the apoptotic pathways to basal cell shrinkage and suprabasal acantholysis. *Experimental dermatology*, 18(9):764–770, 2009.

[162] Jens Waschke, Paola Bruggeman, Werner Baumgartner, Detlef Zillikens, Detlev Drenckhahn, et al. Pemphigus foliaceus igg causes dissociation of desmoglein 1–containing junctions without blocking desmoglein 1 transinteraction. *Journal of Clinical Investigation*, 115(11):3157–3165, 2005.

[163] Ning Wang, Keiji Naruse, Dimitrije Stamenović, Jeffrey J Fredberg, Srboljub M Mijailovich, Iva Marija Tolić-Nørrelykke, Thomas Polte, Robert Mannix, and Donald E Ingber. Mechanical behavior in living cells consistent with the tensegrity model. *Proceedings of the National Academy of Sciences*, 98(14):7765–7770, 2001.

[164] George E Plopper, Helen P McNamee, Laura E Dike, Krzysztof Bojanowski, and Donald E Ingber. Convergence of integrin and growth factor receptor signaling pathways within the focal adhesion complex. *Molecular Biology of the Cell*, 6(10):1349, 1995.

[165] Fang Li, James H-C Wang, and Qing-Ming Wang. Thickness shear mode acoustic wave sensors for characterizing the viscoelastic properties of cell monolayer. *Sensors and Actuators B: Chemical*, 128(2):399–406, 2008.

[166] Kathleen J Green and Claire A Gaudry. Are desmosomes more than tethers for intermediate filaments? *Nature reviews Molecular cell biology*, 1(3):208–216, 2000.

[167] Reinhard Windoffer, Monika Borchert-Stuhlträger, and Rudolf E Leube. Desmosomes: interconnected calcium-dependent structures of remarkable stability with significant integral membrane protein turnover. *Journal of cell science*, 115(8):1717–1732, 2002.

[168] Christoph Riethmuller, Ines Nasdala, and Dietmar Vestweber. Nano-surgery at the leukocyte–endothelial docking site. *Pflügers Archiv-European Journal of Physiology*, 456(1):71–81, 2008.

[169] Zhao Qin, Laurent Kreplak, and Markus J Buehler. Nanomechanical properties of vimentin intermediate filament dimers. *Nanotechnology*, 20(42):425101, 2009.

[170] Laurent Kreplak, Harald Herrmann, and Ueli Aebi. Tensile properties of single desmin intermediate filaments. *Biophysical journal*, 94(7):2790–2799, 2008.

[171] Dimitrije Stamenović, Srboljub M Mijailovich, Iva Marija Tolić-Nørrelykke, Jianxin Chen, and Ning Wang. Cell prestress. ii. contribution of microtubules. *American Journal of Physiology-Cell Physiology*, 282(3):C617–C624, 2002.

[172] Shaohua Hu, Jianxin Chen, and Ning Wang. Cell spreading controls balance of prestress by microtubules and extracellular matrix. *Front Biosci*, 9:2177–2182, 2004.

[173] DIMITRIJE STAMENOVIĆ and MARK F COUGHLIN. The role of prestress and architecture of the cytoskeleton and deformability of cytoskeletal filaments in mechanics of adherent cells: a quantitative analysis. *Journal of theoretical biology*, 201(1):63–74, 1999.

[174] Pavel S Grudinkin, Valery V Zenin, Andrey V Kropotov, Viktoria N Dorosh, and Nikolay N Nikolsky. Egf-induced apoptosis in a431 cells is dependent on stat1, but not on stat3. *European journal of cell biology*, 86(10):591–603, 2007.

[175] Michael Chinkers, James A McKanna, and Stanley Cohen. Rapid rounding of human epidermoid carcinoma cells a-431 induced by epidermal growth factor. *The Journal of cell biology*, 88(2):422–429, 1981.

[176] Anne J Ridley, Martin A Schwartz, Keith Burridge, Richard A Firtel, Mark H Ginsberg, Gary Borisy, J Thomas Parsons, and Alan Rick Horwitz. Cell migration: integrating signals from front to back. *Science*, 302(5651):1704–1709, 2003.

[177] Emilios K Dimitriadis, Ferenc Horkay, Julia Maresca, Bechara Kachar, and Richard S Chadwick. Determination of elastic moduli of thin layers of soft material using the atomic force microscope. *Biophysical Journal*, 82(5):2798–2810, 2002.

[178] Sarah E Cross, Yu-Sheng Jin, Julianne Tondre, Roger Wong, JianYu Rao, and James K Gimzewski. Afm-based analysis of human metastatic cancer cells. *Nanotechnology*, 19(38):384003, 2008.

[179] Etienne Barthel. Adhesive elastic contacts: Jkr and more. *Journal of Physics D: Applied Physics*, 41(16):163001, 2008.

[180] Veronica Saravia and José L Toca-Herrera. Substrate influence on cell shape and cell mechanics: Hepg2 cells spread on positively charged surfaces. *Microscopy research and technique*, 72(12):957–964, 2009.

[181] Oliver Hayden, Roland Bindeus, and Franz L Dickert. Combining atomic force microscope and quartz crystal microbalance studies for cell detection. *Measurement Science and Technology*, 14(11):1876, 2003.

[182] Paul Hansma, Hongmei Yu, David Schultz, Azucena Rodriguez, Eugene A Yurtsev, Jessica Orr, Simon Tang, Jon Miller, Joseph Wallace, Frank Zok, et al. The tissue diagnostic instrument. *Review of Scientific Instruments*, 80(5):054303–054303, 2009.

[183] O Klymenko, J Wiltowska-Zuber, M Lekka, and WM Kwiatek. Energy dissipation in the afm elasticity measurements. *Acta Physica Polonica-Series A General Physics*, 115(2):548, 2009.

[184] Diethelm Johannsmann. Viscoelastic, mechanical, and dielectric measurements on complex samples with the quartz crystal microbalance. *Physical Chemistry Chemical Physics*, 10(31):4516–4534, 2008.

[185] Cheng Dong and Xiao X Lei. Biomechanics of cell rolling: shear flow, cell-surface adhesion, and cell deformability. *Journal of biomechanics*, 33(1):35–43, 2000.

[186] Marina Puig-de Morales-Marinkovic, Kevin T Turner, James P Butler, Jeffrey J Fredberg, and Subra Suresh. Viscoelasticity of the human red blood cell. *American Journal of Physiology-Cell Physiology*, 293(2):C597–C605, 2007.

[187] Heng Xie, Manuel A Pallero, Kiran Gupta, Philip Chang, Margaret F Ware, Walter Witke, David J Kwiatkowski, Douglas A Lauffenburger, Joanne E Murphy-Ullrich, and Alan Wells. Egf receptor regulation of cell motility: Egf induces disassembly of focal adhesions independently of the motility-associated plcgamma signaling pathway. *Journal of cell science*, 111(5):615–624, 1998.

[188] K-F Giebel, Clemens Bechinger, Stephan Herminghaus, M Riedel, Paul Leiderer, Ulrich Weiland, and Martin Bastmeyer. Imaging of cell/substrate contacts of living cells with surface plasmon resonance microscopy. *Biophysical journal*, 76(1):509–516, 1999.

[189] Joachim Wegener, Jochen Seebach, Andreas Janshoff, and Hans-Joachim Galla. Analysis of the composite response of shear wave resonators to the attachment of mammalian cells. *Biophysical journal*, 78(6):2821–2833, 2000.

[190] Michael Rodahl and Bengt Kasemo. On the measurement of thin liquid overlayers with the quartz-crystal microbalance. *Sensors and Actuators A: Physical*, 54(1):448–456, 1996.

[191] F Höök, M Rodahl, P Brzezinski, and B Kasemo. Energy dissipation kinetics for protein and antibody-antigen adsorption under shear oscillation on a quartz crystal microbalance. *Langmuir*, 14(4):729–734, 1998.

[192] L áMichelle Furtado et al. Hybridization of complementary strand and single-base mutated oligonucleotides detected with an on-line acoustic wave sensor. *Analyst*, 123(10):1937–1945, 1998.

[193] C Fredriksson, S Kihlman, M Rodahl, and B Kasemo. The piezoelectric quartz crystal mass and dissipation sensor: a means of studying cell adhesion. *Langmuir*, 14(2):248–251, 1998.

[194] Michael Rodahl, Fredrik Höök, Claes Fredriksson, Craig A Keller, Anatol Krozer, Peter Brzezinski, Marina Voinova, and Bengt Kasemo. Simultaneous frequency and dissipation factor qcm measurements of biomolecular adsorption and cell adhesion. *Faraday discussions*, 107:229–246, 1997.

[195] Megan Susan Lord, Charlotte Modin, Morten Foss, Mogens Duch, Anne Simmons, Finn S Pedersen, Bruce K Milthorpe, and Flemming Besenbacher. Monitoring cell adhesion on tantalum and oxidised polystyrene using a quartz crystal microbalance with dissipation. *Biomaterials*, 27(26):4529–4537, 2006.

[196] Megan S Lord, Charlotte Modin, Morten Foss, Mogens Duch, Anne Simmons, Finn S Pedersen, Flemming Besenbacher, and Bruce K Milthorpe. Extracellular matrix remodelling during cell adhesion monitored by the quartz crystal microbalance. *Biomaterials*, 29(17):2581–2587, 2008.

[197] Kenneth A Marx, Tiean Zhou, Anne Montrone, Donna McIntosh, and Susan J Braunhut. A comparative study of the cytoskeleton binding drugs nocodazole and taxol with a mammalian cell quartz crystal microbalance biosensor: Different dynamic responses and energy dissipation effects. *Analytical biochemistry*, 361(1):77–92, 2007.

[198] Joachim Wegener, Andreas Janshoff, and H-J Galla. Cell adhesion monitoring using a quartz crystal microbalance: comparative analysis of different mammalian cell lines. *European biophysics journal*, 28(1):26–37, 1998.

[199] Vanessa Heitmann and Joachim Wegener. Monitoring cell adhesion by piezoresonators: impact of increasing oscillation amplitudes. *Analytical chemistry*, 79(9):3392–3400, 2007.

[200] Jennifer Y Chen, Minghong Li, Lynn S Penn, and Jun Xi. Real-time and label-free detection of cellular response to signaling mediated by distinct subclasses of epidermal growth factor receptors. *Analytical Chemistry*, 83(8):3141–3146, 2011.

[201] Jonathan S Ellis and Michael Thompson. Viscoelastic modeling with interfacial slip of a protein monolayer electrode-adsorbed on an acoustic wave biosensor. *Langmuir*, 26(13):11558–11567, 2010.

[202] Diethelm Johannsmann. Studies of viscoelasticity with the qcm. In *Piezoelectric Sensors*, pages 49–109. Springer, 2007.

[203] Le Guillou-Buffello, Marcel Gindre, Paul Johnson, Pascal Laugier, Véronique Migonney, et al. An alternative quantitative acoustical and electrical method for detection of cell adhesion process in real-time. *Biotechnology and bioengineering*, 108(4):947–962, 2011.

[204] E Gnecco, R Bennewitz, and E Meyer. Abrasive wear on the atomic scale. *Physical review letters*, 88(21):215501, 2002.

[205] C Drummond, J Israelachvili, and Ph Richetti. Friction between two weakly adhering boundary lubricated surfaces in water. *Physical Review E*, 67(6):066110, 2003.

[206] AE Filippov, J Klafter, and M Urbakh. Friction through dynamical formation and rupture of molecular bonds. *Physical review letters*, 92(13):135503, 2004.

[207] Jonathan S Ellis and Michael Thompson. Slip and coupling phenomena at the liquid–solid interface. *Physical Chemistry Chemical Physics*, 6(21):4928–4938, 2004.

[208] Michael Rodahl and Bengt Kasemo. Frequency and dissipation-factor responses to localized liquid deposits on a qcm electrode. *Sensors and Actuators B: Chemical*, 37(1):111–116, 1996.

[209] Jacob Klein. Frictional dissipation in stick-slip sliding. *Physical review letters*, 98(5):056101, 2007.

[210] Julia Schmitz and Kay-Eberhard Gottschalk. Mechanical regulation of cell adhesion. *Soft Matter*, 4(7):1373–1387, 2008.

[211] GEORGE I Bell, MICAH Dembo, and PIERRE Bongrand. Cell adhesion. competition between nonspecific repulsion and specific bonding. *Biophysical Journal*, 45(6):1051–1064, 1984.

[212] Dong Kong, Baohua Ji, and Lanhong Dai. Stability of adhesion clusters and cell reorientation under lateral cyclic tension. *Biophysical journal*, 95(8):4034–4044, 2008.

[213] John Charles Butcher. *The numerical analysis of ordinary differential equations: Runge-Kutta and general linear methods*. Wiley-Interscience, 1987.

[214] Benedikt Sabass and Ulrich S Schwarz. Modeling cytoskeletal flow over adhesion sites: competition between stochastic bond dynamics and intracellular relaxation. *Journal of Physics: Condensed Matter*, 22(19):194112, 2010.

[215] Dong Kong, Baohua Ji, and Lanhong Dai. Stabilizing to disruptive transition of focal adhesion response to mechanical forces. *Journal of biomechanics*, 43(13):2524–2529, 2010.

[216] Linda J Rinko, Michael B Lawrence, and William H Guilford. The molecular mechanics of p-and l-selectin lectin domains binding to psgl-1. *Biophysical journal*, 86(1):544–554, 2004.

[217] Sanjay Kumar, Iva Z Maxwell, Alexander Heisterkamp, Thomas R Polte, Tanmay P Lele, Matthew Salanga, Eric Mazur, and Donald E Ingber. Viscoelastic retraction of single living stress fibers and its impact on cell shape, cytoskeletal organization, and extracellular matrix mechanics. *Biophysical journal*, 90(10):3762, 2006.

[218] Michael D Ward, Micah Dembo, and Daniel A Hammer. Kinetics of cell detachment: peeling of discrete receptor clusters. *Biophysical journal*, 67(6):2522–2534, 1994.

[219] Elisabetta Ada Cavalcanti-Adam, Tova Volberg, Alexandre Micoulet, Horst Kessler, Benjamin Geiger, and Joachim Pius Spatz. Cell spreading and focal adhesion dynamics are regulated by spacing of integrin ligands. *Biophysical journal*, 92(8):2964–2974, 2007.

[220] BNJ Persson. Applications of surface resistivity to atomic scale friction, to the migration of hotadatoms, and to electrochemistry. *The Journal of chemical physics*, 98:1659, 1993.

[221] Nina Tymchenko, Erik Nilebäck, Marina V Voinova, Julie Gold, Bengt Kasemo, and Sofia Svedhem. Reversible changes in cell morphology due to cytoskeletal rearrangements measured in real-time by qcm-d. *Biointerphases*, 7(1-4):1–9, 2012.

[222] Carlos Drummond and Jacob Israelachvili. Dynamic phase transitions in confined lubricant fluids under shear. *Physical Review E*, 63(4):041506, 2001.

[223] Paul W Wiseman, Claire M Brown, Donna J Webb, Benedict Hebert, Natalie L Johnson, Jeff A Squier, Mark H Ellisman, and AF Horwitz. Spatial mapping of integrin interactions and dynamics during cell migration by image correlation microscopy. *Journal of cell science*, 117(23):5521–5534, 2004.

[224] Mark A Lemmon and Joseph Schlessinger. Cell signaling by receptor-tyrosine kinases. *Cell*, 141(7):1117, 2010.

[225] Graham Carpenter. Receptors for epidermal growth factor and other polypeptide mitogens. *Annual review of biochemistry*, 56(1):881–914, 1987.

[226] AP Dei Tos and I Ellis. Assessing epidermal growth factor receptor expression in tumours: what is the value of current test methods? *European Journal of Cancer*, 41(10):1383–1392, 2005.

[227] Alan Wells, Jareer Kassis, James Solava, Timothy Turner, and Douglas A Lauffenburger. Growth factor-induced cell motility in tumor invasion. *Acta Oncologica*, 41(2):124–130, 2002.

[228] Douglas A Lauffenburger and Alan F Horwitz. Cell migration: Review a physically integrated molecular process. *Cell*, 84:359–369, 1996.

[229] Robert J Cain and Anne J Ridley. Phosphoinositide 3-kinases in cell migration. *Biology of the Cell*, 101(1):13–29, 2009.

[230] Fred D Allen, Clara F Asnes, Philip Chang, Elliot L Elson, Douglas A Lauffenburger, and Alan Wells. Epidermal growth factor induces acute matrix contraction and subsequent calpain-modulated relaxation. *Wound repair and regeneration*, 10(1):67–76, 2002.

[231] Jeongah Yoon and Thomas S Deisboeck. Investigating differential dynamics of the mapk signaling cascade using a multi-parametric global sensitivity analysis. *PloS one*, 4(2):e4560, 2009.

[232] H Steven Wiley, Stanislav Y Shvartsman, and Douglas A Lauffenburger. Computational modeling of the egf-receptor system: a paradigm for systems biology. *Trends in cell biology*, 13(1):43–50, 2003.

[233] Ami Citri and Yosef Yarden. Egf–erbb signalling: towards the systems level. *Nature reviews Molecular cell biology*, 7(7):505–516, 2006.

[234] C Wofsy, B Goldstein, K Lund, and HS Wiley. Implications of epidermal growth factor (egf) induced egf receptor aggregation. *Biophysical journal*, 63(1):98–110, 1992.

[235] Haluk Resat, Jonathan A Ewald, David A Dixon, and H Steven Wiley. An integrated model of epidermal growth factor receptor trafficking and signal transduction. *Biophysical journal*, 85(2):730–743, 2003.

[236] Boris N Kholodenko, Oleg V Demin, Gisela Moehren, and Jan B Hoek. Quantification of short term signaling by the epidermal growth factor receptor. *Journal of Biological Chemistry*, 274(42):30169–30181, 1999.

[237] Birgit Schoeberl, Claudia Eichler-Jonsson, Ernst Dieter Gilles, and Gertraud Müller. Computational modeling of the dynamics of the map kinase cascade activated by surface and internalized egf receptors. *Nature biotechnology*, 20(4):370–375, 2002.

[238] Neil Kumar, Raffi Afeyan, Hyung-Do Kim, and Douglas A Lauffenburger. Multipathway model enables prediction of kinase inhibitor cross-talk effects on migration of her2-overexpressing mammary epithelial cells. *Molecular pharmacology*, 73(6):1668–1678, 2008.

[239] Frances A Brightman and David A Fell. Differential feedback regulation of the mapk cascade underlies the quantitative differences in egf and ngf signalling in pc12 cells. *FEBS letters*, 482(3):169–174, 2000.

[240] NI Markevich, G Moehren, OV Demin, A Kiyatkin, JB Hoek, and BN Kholodenko. Signal processing at the ras circuit: what shapes ras activation patterns? *Systems biology*, 1(1):104–113, 2004.

[241] Satoru Sasagawa, Yu-ichi Ozaki, Kazuhiro Fujita, and Shinya Kuroda. Prediction and validation of the distinct dynamics of transient and sustained erk activation. *Nature Cell Biology*, 7(4):365–373, 2005.

[242] Stanislav Y Shvartsman, Cyrill B Muratov, and Douglas A Lauffenburger. Modeling and computational analysis of egf receptor-mediated cell communication in drosophila oogenesis. *Development*, 129(11):2577–2589, 2002.

[243] Mariko Hatakeyama, Shuhei Kimura, Takashi Naka, Takuji Kawasaki, Noriko Yumoto, Mio Ichikawa, Jae-Hoon Kim, Kazuki Saito, Mihoro Saeki, Mikako Shirouzu, et al. A computational model on the modulation of mitogen-activated protein kinase (mapk) and akt pathways in heregulin-induced erbb signalling. *Biochemical Journal*, 373(Pt 2):451, 2003.

[244] Regina Samaga, Julio Saez-Rodriguez, Leonidas G Alexopoulos, Peter K Sorger, and Steffen Klamt. The logic of egfr/erbb signaling: theoretical properties and analysis of high-throughput data. *PLoS computational biology*, 5(8):e1000438, 2009.

[245] EVAN A Evans. Detailed mechanics of membrane-membrane adhesion and separation. i. continuum of molecular cross-bridges. *Biophysical journal*, 48(1):175–183, 1985.

[246] Reinhard Lipowsky. Adhesion of membranes via anchored stickers. *Physical review letters*, 77(8):1652–1655, 1996.

[247] Thomas R Weikl and Reinhard Lipowsky. Adhesion-induced phase behavior of multicomponent membranes. *Physical Review E*, 64(1):011903, 2001.

[248] Thorsten Erdmann and Ulrich S Schwarz. Stochastic dynamics of adhesion clusters under shared constant force and with rebinding. *The Journal of chemical physics*, 121:8997, 2004.

[249] Alice Nicolas, Benjamin Geiger, and Samuel A Safran. Cell mechanosensitivity controls the anisotropy of focal adhesions. *Proceedings of the National Academy of Sciences of the United States of America*, 101(34):12520–12525, 2004.

[250] Tom Shemesh, Benjamin Geiger, Alexander D Bershadsky, and Michael M Kozlov. Focal adhesions as mechanosensors: a physical mechanism. *Proceedings of the National Academy of Sciences of the United States of America*, 102(35):12383–12388, 2005.

[251] Vikram S Deshpande, Robert M McMeeking, and Anthony G Evans. A model for the contractility of the cytoskeleton including the effects of stress-fibre formation and dissociation. *Proceedings of the Royal Society A: Mathematical, Physical and Engineering Science*, 463(2079):787–815, 2007.

[252] Ana-Sunčana Smith, Kheya Sengupta, Stefanie Goennenwein, Udo Seifert, and Erich Sackmann. Force-induced growth of adhesion domains is controlled by receptor mobility. *Proceedings of the National Academy of Sciences*, 105(19):6906–6911, 2008.

[253] Clarence E Chan and David J Odde. Traction dynamics of filopodia on compliant substrates. *Science Signaling*, 322(5908):1687, 2008.

[254] Alice Macdonald, A Rick Horwitz, and Douglas A Lauffenburger. Kinetic model for lamellipodal actin-integrin'clutch'dynamics. *Cell adhesion & migration*, 2(2):95–105, 2008.

[255] Sourabh Kharait, Kien Tran, Clayton Yates, and Alan Wells. Cell motility in prostate tumor invasion and metastasis. In *Cell Motility in Cancer Invasion and Metastasis*, pages 301–338. Springer, 2006.

[256] Susanne Rogers and Suzanne Eccles. Egfr signaling in invasion, angiogenesis and metastasis. In *EGFR Signaling Networks in Cancer Therapy*, pages 245–264. Springer, 2008.

[257] Charles Kumar Thodeti and Kaustabh Ghosh. Mechanisms of tumor cell migration and invasion in lung cancer metastasis. In *Lung Cancer Metastasis*, pages 93–109. Springer, 2010.

[258] Matthew J Lazzara and Douglas A Lauffenburger. Quantitative modeling perspectives on the erbb system of cell regulatory processes. *Experimental cell research*, 315(4):717–725, 2009.

[259] Allison L Berrier and Kenneth M Yamada. Cell–matrix adhesion. *Journal of cellular physiology*, 213(3):565–573, 2007.

[260] Matthew C Dixon. Quartz crystal microbalance with dissipation monitoring: enabling real-time characterization of biological materials and their interactions. *Journal of biomolecular techniques: JBT*, 19(3):151, 2008.

[261] Vanessa Heitmann, Björn Reiß, and Joachim Wegener. The quartz crystal microbalance in cell biology: basics and applications. In *Piezoelectric Sensors*, pages 303–338. Springer, 2007.

[262] Nathalie Q Balaban, Ulrich S Schwarz, Daniel Riveline, Polina Goichberg, Gila Tzur, Ilana Sabanay, Diana Mahalu, Sam Safran, Alexander Bershadsky, Lia Addadi, et al. Force and focal adhesion assembly: a close relationship studied using elastic micropatterned substrates. *Nature cell biology*, 3(5):466–472, 2001.

[263] Karen A Beningo, Micah Dembo, Irina Kaverina, J Victor Small, and Yu-li Wang. Nascent focal adhesions are responsible for the generation of strong propulsive forces in migrating fibroblasts. *The Journal of cell biology*, 153(4):881–888, 2001.

[264] Nathan D Gallant, Kristin E Michael, and Andrés J García. Cell adhesion strengthening: contributions of adhesive area, integrin binding, and focal adhesion assembly. *Molecular biology of the cell*, 16(9):4329–4340, 2005.

[265] John L Tan, Joe Tien, Dana M Pirone, Darren S Gray, Kiran Bhadriraju, and Christopher S Chen. Cells lying on a bed of microneedles: an approach to isolate mechanical force. *Proceedings of the National Academy of Sciences*, 100(4):1484–1489, 2003.

[266] Lennart Ljung. Aspects on the system identification problem. *Signal Processing*, 4(5):445–456, 1982.

[267] RP Araujo, EF Petricoin, and LA Liotta. A mathematical model of combination therapy using the egfr signaling network. *Biosystems*, 80(1):57–69, 2005.

[268] Kevin S Brown, Colin C Hill, Guillermo A Calero, Christopher R Myers, Kelvin H Lee, James P Sethna, and Richard A Cerione. The statistical mechanics of complex signaling networks: nerve growth factor signaling. *Physical Biology*, 1(3):184, 2004.

[269] William W Chen, Birgit Schoeberl, Paul J Jasper, Mario Niepel, Ulrik B Nielsen, Douglas A Lauffenburger, and Peter K Sorger. Input–output behavior of erbb signaling pathways as revealed by a mass action model trained against dynamic data. *Molecular systems biology*, 5(1), 2009.